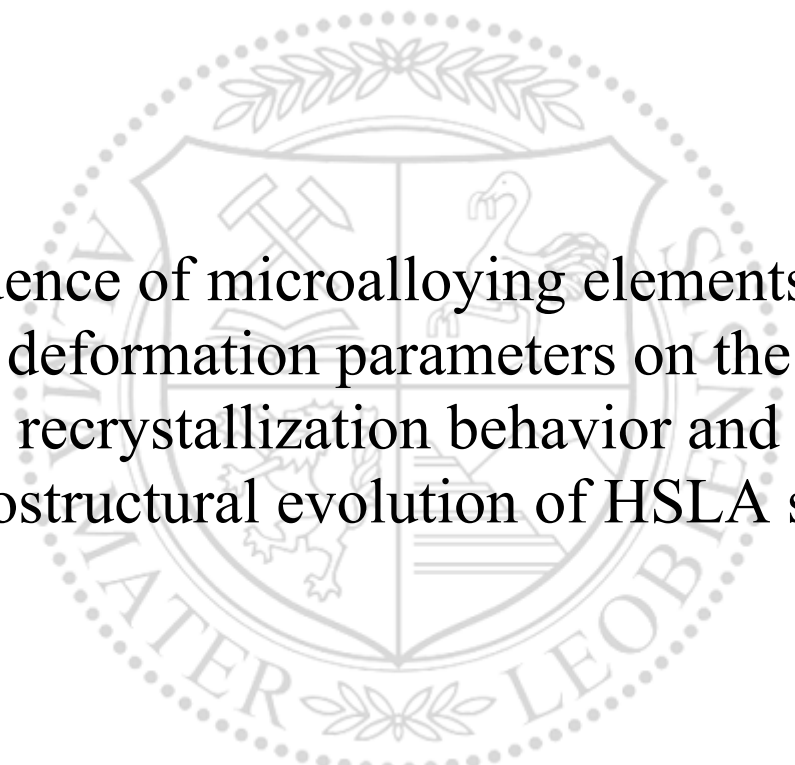




Chair of Design of Steels

Doctoral Thesis



Influence of microalloying elements and
deformation parameters on the
recrystallization behavior and
microstructural evolution of HSLA steels

Dipl.-Ing. Stefan Monschein, BSc

July 2022



EIDESSTATTLICHE ERKLÄRUNG

Ich erkläre an Eides statt, dass ich diese Arbeit selbständig verfasst, andere als die angegebenen Quellen und Hilfsmittel nicht benutzt, und mich auch sonst keiner unerlaubten Hilfsmittel bedient habe.

Ich erkläre, dass ich die Richtlinien des Senats der Montanuniversität Leoben zu "Gute wissenschaftliche Praxis" gelesen, verstanden und befolgt habe.

Weiters erkläre ich, dass die elektronische und gedruckte Version der eingereichten wissenschaftlichen Abschlussarbeit formal und inhaltlich identisch sind.

Datum 01.07.2022

Unterschrift Verfasser/in
Stefan Monschein

Danksagung

Der Beginn meiner Arbeit ist jenen Personen gewidmet, die mich in den letzten Jahren persönlich, sowie fachlich unterstützten und somit wesentlich zum Gelingen dieser Arbeit beigetragen haben.

Mein erster Dank gebührt meinem Betreuer Ronald Schnitzer. Sein warmherziger Führungsstil, seine fachliche Kompetenz und zahllose Gespräche und Diskussionen trugen in großem Maße zum Erfolg dieser Arbeit bei. Vielen Dank, dass Du immer ein offenes Ohr für meine Anliegen hattest und stets bemüht warst mich bei diesen zu unterstützen. Ebenfalls herzlich danken möchte ich Martin Stockinger, welcher die Mentorenrolle in meinem Dissertationsvorhaben übernommen hat.

Bei meinen Kolleginnen und Kollegen der voestalpine Wire Rod Austria GmbH, voestalpine Stahl Donawitz GmbH und voestalpine Forschungsservicegesellschaft Donawitz GmbH möchte ich mich ebenfalls recht herzlich bedanken. Hervorheben möchte ich hier vor allem Marlene Kapp, Katharina Ragger, Josef Fasching, sowie Dominik Zügner. Ich konnte in den unzähligen Projektmeetings immer auf euer Feedback vertrauen.

Für die Unterstützung und Durchführung meiner zahlreichen Versuche am Abschreck- und Umformdilatometer gebührt meinem Bürokollegen Thomas Fischer ein großer Dank. Meinen studentischen Kollegen, deren Master- und Bachelorarbeiten ich teilweise betreuen durfte, gebührt ebenso ein großer Dank. Hervorheben möchte ich hier Nikolaus Kostwein, Jakob Eschelbeck und Katharina Käsznar.

Ein großes Dankeschön geht ebenfalls an meine Kollegen Ganesh und Gloria aus unserem Exotenbüro. Trotz unserer völlig unterschiedlichen Charaktere, waren die gemeinsamen Stunden mit euch immer von gegenseitiger Wertschätzung und Humor geprägt.

Mein größter Dank gebührt jedoch meiner Familie, insbesondere meinen Eltern Barbara und Josef Monschein. Eure aufopfernde und liebevolle Erziehung hat es Theresa, Katharina und mir erst ermöglicht unsere gewählten Wege einzuschlagen. Danke für Alles!

Abschließend möchte ich noch die Gelegenheit nutzen um mich bei meinen Freunden und Wegbegleitern in meiner Heimat Mürzhofen zu bedanken. Lieber Thomas, Felix, Lukas, Dominik, Michael und Christoph, Danke für eure langjährige und unzerbrechliche Freundschaft, die unvergesslichen Abende und eure moralische Unterstützung.

Abstract

For years, high - strength low - alloyed (HSLA) steels have been state of the art when materials are needed that combine high strength and toughness. Thanks to a combination of thermomechanical controlled processing (TMCP) and the addition of microalloying elements, such as Ti, Nb and V, a fine - grained microstructure in the as - rolled condition is obtained, which positively influences these properties. Due to the usually low C content of less than 0.1 wt%, these steels also show excellent weldability. In terms of strength and hardenability, however, steels with a low carbon content often do not meet the desired requirements, which is why the trend is going towards higher C contents.

For this reason, this doctoral thesis deals with the influence of microalloying elements and TMCP on the recrystallization behavior and microstructure development of HSLA steels with C contents above 0.2 wt%. Through a combination of deformation dilatometer experiments and high - resolution characterization methods, the influence of the microalloying elements, both in dissolved form and in the form of precipitates, was investigated.

A new method was developed which has the potential to automatically determine the degree of recrystallization of microalloyed HSLA steels using light optical microscopy and analysis of grain elongation.

The combined addition of Nb and Ti, as well as the role of various deformation parameters was investigated with regard to the recrystallization behavior and microstructure evolution. A right balance must be found when choosing the Ti content in Nb and Ti microalloyed steels to simultaneously obtain the positive effects of Ti against grain coarsening and the positive effects of Nb on the recrystallization behavior.

Finally, new insights into the formation mechanism of dynamic strain - induced transformed ferrite could be found by atom probe tomography and electron backscatter diffraction. The results suggest that the formation is a displacive mechanism, although accompanied by the diffusion of C during the formation.

Kurzfassung

Hochfeste niedriglegierte (HSLA) Stähle sind seit Jahren Stand der Technik, wenn hohe Festigkeiten und Zähigkeiten benötigt werden. Durch eine Kombination aus thermomechanischem (TM) Walzen und dem Zusatz von Mikrolegierungselementen, wie Ti, Nb und V, wird im gewalzten Zustand ein feinkörniges Gefüge erzielt, das beide Eigenschaften positiv beeinflusst. Aufgrund des meist niedrigen C - Gehalts von weniger als 0,1 m% weisen diese Stähle zudem eine hervorragende Schweißbarkeit auf. Bezüglich Festigkeit und Härtebarkeit erfüllen Stähle mit niedrigem C - Gehalt jedoch oft nicht die gewünschten Anforderungen, weshalb der Trend zu höheren Gehältern geht.

Diese Doktorarbeit beschäftigt sich daher mit dem Einfluss von Mikrolegierungselementen und TM - Prozessen auf das Rekristallisationsverhalten und die Gefügeentwicklung von HSLA - Stählen mit C - Gehalten über 0,2 m%. Durch Experimente an einem Umformdilatometer und dem Einsatz von hochauflösenden Charakterisierungsmethoden wurde der Einfluss der Mikrolegierungselemente, sowohl in gelöster Form, als auch in Form von Ausscheidungen untersucht.

Es wurde ein neues Verfahren entwickelt, das zukünftig das Potenzial hat, den Rekristallisationsgrad von mikrolegierten HSLA - Stählen mittels Lichtmikroskopie und Analyse der Kornstreckung automatisch zu bestimmen.

Die kombinierte Zugabe von Nb und Ti, sowie die Rolle verschiedener Umformparameter, wurde im Hinblick auf das Rekristallisationsverhalten und die Gefügeentwicklung untersucht. Bei der Wahl des Ti - Gehalts in mit Nb und Ti mikrolegierten Stählen muss ein richtiges Gleichgewicht gefunden werden, um gleichzeitig die positive Wirkung von Ti gegen Kornvergrößerung, sowie von Nb auf das Rekristallisationsverhalten zu erhalten.

Durch Atomsondentomographie und Elektronenrückstreubeugung konnten neue Einblicke in den Bildungsmechanismus von dynamisch spannungsinduziert umgewandelten Ferrit gewonnen werden. Die Ergebnisse deuten darauf hin, dass die Bildung ein Umklappmechanismus ist, begleitet von C - Diffusion während der Bildung.

List of abbreviations

APT.....	<i>atom probe tomography</i>
DBTT.....	ductile - brittle transition temperature
DRV.....	<i>dynamic recovery</i>
DRX.....	<i>dynamic recrystallization</i>
DSIT.....	<i>dynamic strain - induced transformation</i>
EBSD.....	<i>electron backscatter diffraction</i>
EDX.....	<i>energy dispersive X - ray diffraction</i>
HSLA.....	<i>high - strength low - alloyed</i>
LOM.....	<i>light - optical microscopy</i>
LVDT.....	<i>linear variable differential transformer</i>
MAE.....	<i>microalloying element</i>
MDRX.....	<i>metadynamic recrystallization</i>
M _s	<i>martensite start temperature</i>
PAGB.....	<i>prior austenite grain boundary</i>
PDRX.....	<i>post - dynamic recrystallization</i>
SEM.....	<i>scanning electron microscope</i>
SFE.....	<i>stacking fault energy</i>
SRV.....	<i>static recovery</i>
SRX.....	<i>static recrystallization</i>
STEM.....	<i>scanning transmission electron microscopy</i>
T _{def}	<i>deformation temperature</i>
TEM.....	<i>transission electron microscopy</i>
TKD.....	<i>transmission Kikuchi diffraction</i>
TMCP.....	<i>thermomechanical controlled processing</i>
T _{NR}	<i>non - recrystallization temperature</i>

Table of content

Abstract	I
Kurzfassung	II
List of abbreviations	III
Table of content	IV
1 Motivation	1
2 Theoretical background	3
2.1 Thermomechanical controlled rolling	3
2.2 Rolling of wire products	5
2.3 Concept of microalloyed HSLA steels	6
2.4 Recovery and recrystallization	11
2.5 Structure - property relationship of martensite	16
3 Experimental methods and challenges	20
3.1 Dilatometry	20
3.2 Atom probe tomography	25
3.3 Transmission Kikuchi diffraction	26
4 Relation of the current thesis to the state of the art	29
5 Published content	30
5.1 Appended peer - reviewed papers	30
5.2 Conference Contributions	89
5.3 Co - supervised theses.....	89
6 Summary and discussion of the published content	90
6.1 Aim and scope of the investigations	90
6.2 Development of a method for determining the degree of recrystallization.....	92
6.3 Characterization of microalloy precipitates.....	94
6.4 Influence of deformation parameters on recrystallization and microstructure.	97
6.5 Influence of the microalloying elements on recrystallization, grain growth and microstructure.....	101
7 Novel features	105
8 References	106

1 Motivation

The permanent optimization of steels with the goal to increase strength and toughness, while at the same time to reduce production costs, poses a challenge task to researchers and steel manufacturers worldwide. In the past, a combination of microalloyed high - strength low - alloyed (HSLA) steels and thermomechanical controlled processing (TMCP) has proven itself to enable the production of steels with increased strength and excellent toughness at the same time [1]. The trick behind the aforementioned combination is a grain refinement in the as - rolled condition through TMCP which has a positive effect on both, the strength and toughness [2]. Furthermore, HSLA steels possess good weldability due to a low C content, which is usually below 0.1 wt% in such steels [3]. However, the development of quenched and tempered steels is moving towards higher C contents, since the desired strength and hardenability can hardly be achieved with such low C levels. The higher C levels, in turn, also have negative effects. As an example, next to the lower weldability, also poorer cold formability in the as - rolled condition can be mentioned. Therefore, in order to minimize the negative effects and to be able to deliver optimal product properties, research in the field of HSLA steels is going towards optimizing the combination of TMCP and the addition of microalloying elements (MAE) in steels with higher C levels.

This thesis deals with the investigation of microalloyed HSLA steels with a C content of more than 0.2 wt%, used for rolling of high performance wire products. It aims to investigate the influence of microalloying concepts and forming parameters in order to optimize the strength, toughness and cold formability in the as - rolled condition of rolled wire products. Basically, this work can be separated into two parts. One of them deals with the optimization of the low - temperature toughness of wire products, which are, among other things, used for the production of hoist chains. The aim here is to use a combination of TMCP and the addition of MAE, such as Nb and Ti, to achieve a fine - grained microstructure in the as - rolled state. Subsequently this should lead to a fine martensitic microstructure after quenching and tempering, which therefore should have a positive effect on the low - temperature toughness. Based on two reference alloys (23MnNiCrMo5-2 and 23MnNiCrMo5-4), additionally microalloyed variants with varying contents of Ti and Nb were produced and examined. In order to investigate the influence of different forming parameters, such as the annealing - or deformation temperature (T_{def}), on the recrystallization - and precipitation kinetics, deformation experiments were carried out using a deformation dilatometer. Furthermore, annealing experiments were

performed to investigate the influence of different contents of MAE on the grain growth behavior.

The second part of this work deals with microalloyed steels used in the production of high performance wires, which are further used, among other things, for the production of screws. In order to reduce the production costs, the investigation aims to realize alloy concepts with a reduced proportion of expensive alloying elements, which, through a combination with optimized forming concepts, enable direct formability in the as-rolled state and still provide sufficiently high strength in the quenched and tempered condition. The influence of different deformation parameters on the development of the microstructure was examined by means of experiments carried out with a deformation dilatometer.

Both research areas had in common that, in addition to the deformation dilatometer experiments, comprehensive high - resolution characterization methods, such as atom probe tomography (APT), scanning transmission electron microscopy (STEM) or transmission Kikuchi diffraction (TKD), were carried out to characterize the precipitates and their influence on the structure - property relationships of the examined steels.

The main goal of this work was to gain knowledge with regard to the interaction of the MAE and TMCP parameters in order to optimize future industrial large - scale wire rolling processes.

2 Theoretical background

This chapter aims to acquaint the reader with important concepts and terms that play an important role in this thesis. At the beginning TMCP is briefly discussed and then peculiarities of thermomechanically rolled wire products are pointed out in more detail. In another chapter, the concept of microalloyed HSLA steels is examined and the role of the individual MAE is described separately. Since terms such as recovery, recrystallization and the formation of strain - induced precipitates play an important role in TMCP, these points will also be explained. Finally, the current state of the art to the structure - property relationship of martensitic microstructures is reflected.

2.1 Thermomechanical controlled rolling

Until the beginning of the 1960s, the strength of normalized rolled steel products was controlled by the amount and spacing of pearlite lamellas, the grain size and the content of alloying elements responsible for solid solution strengthening, e.g. Mn and Si. The constant demand for lowering production costs, while at the same time increasing strength, toughness and weldability required a fundamental rethinking of the rolling processes and were the driving force behind the development of thermomechanical processed HSLA steels [2,4–6]. These steels are characterized by a low C content of usually less than 0.1 wt%. The loss of strength, resulting from the lower C levels, is not only compensated in these steels, but even improved by a combination of TMCP and the addition of MAE, such as Nb, Ti and V. The basic principle behind TMCP is depicted in Figure 2.1 and shows that prior to the rolling process, the billets are heated to annealing temperatures in the austenite regime. The annealing temperature is chosen in a way that the microalloying elements, which are responsible for the formation of deformation - induced precipitates, are in solution prior to the rolling process. In most cases this is dependent on the Nb and C concentration in such steels [7]. Furthermore, the high annealing temperatures also lead to an easier rolling process, due to the lower rolling forces required.

To prevent excessive grain coarsening during annealing, Ti is alloyed to these steels, as this inhibits the grain growth through the formation of stable TiN precipitates [8]. At the beginning of the rolling process, TMCP does not differ from normalized rolling. However, there are differences in the selection of the finishing rolling temperature, which is lower for TMCP than for normalized rolling and lies below the non - recrystallization temperature (T_{NR}) [2].

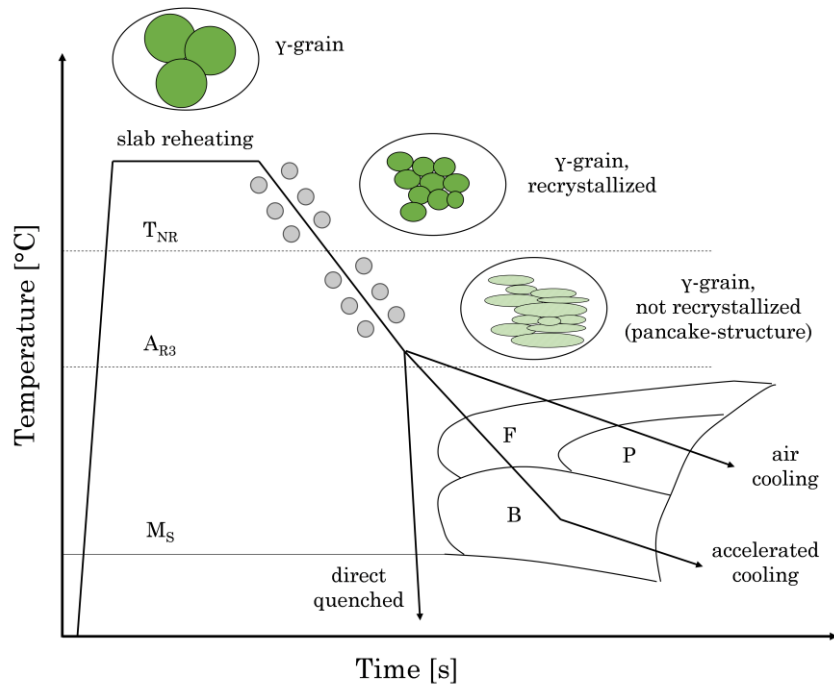


Figure 2.1: Schematic drawing of the basic principle behind TMCP. Adapted from [2].

The T_{NR} is the temperature, below which there is no complete static recrystallization between the rolling passes and its concept is described in Figure 2.2. Figure 2.2 a) shows the microstructural changes between the rolling passes for $T_{def} > T_{NR}$. A flattened “pancake” microstructure can be seen directly after the first rolling pass. However, complete recrystallization occurs between the two rolling passes. In Figure 2.2 b) $T_{def} < T_{NR}$ and therefore no complete recrystallization takes place between the rolling passes. The so - called pancake structure therefore remains, which leads to an increasing number of nucleation sites for the following ferrite transformation, since ferrite nucleates mainly along prior austenite grain boundaries (PAGB), twin boundaries and dislocation bands inside the austenite grains. In combination with accelerated cooling after rolling, this leads to a fine grained microstructure which, depending on the cooling rate, can be ferritic - perlitic, ferritic - bainitic, or bainitic - martensitic. The concentration of the MAE and the selection of the forming parameters during TMCP have a strong influence on the precipitation kinetics and the recrystallization - and transformation behavior.

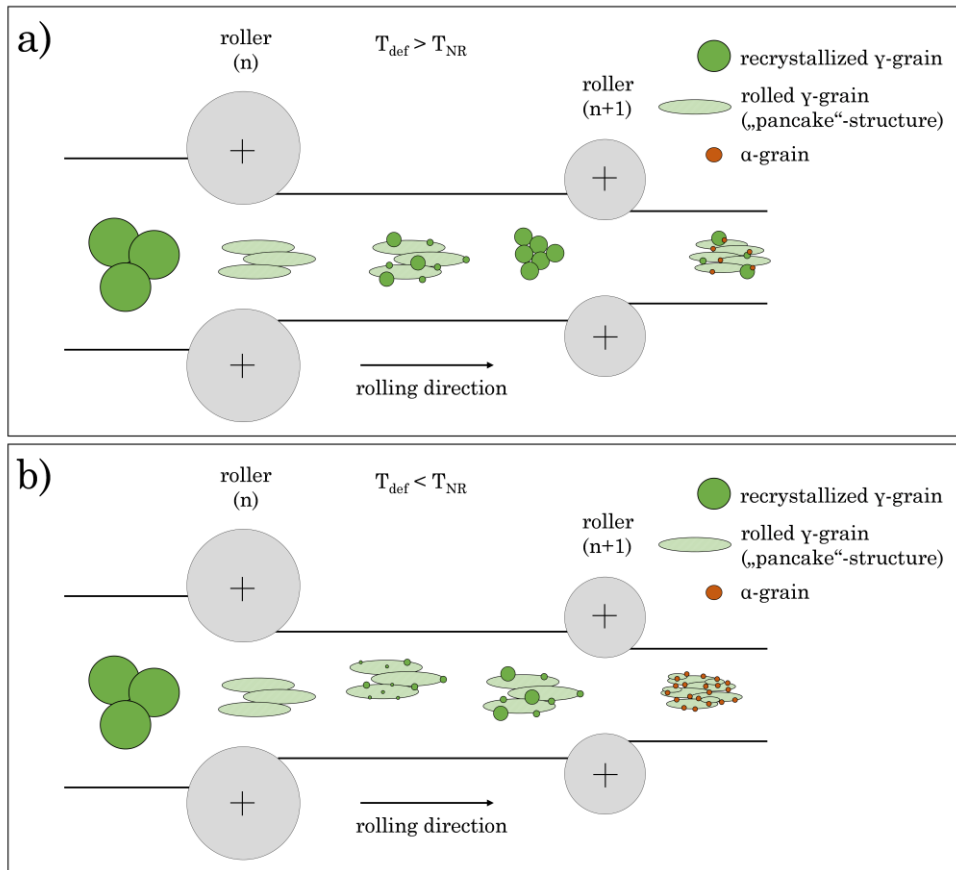


Figure 2.2: Schematic illustration of the concept of the T_{NR} . a) $T_{def} > T_{NR} \rightarrow$ complete recrystallization between the rolling passes. b) $T_{def} < T_{NR} \rightarrow$ no complete recrystallization between the rolling passes. Image adapted from [2].

2.2 Rolling of wire products

A typical production process for the manufacturing of wire rod is shown schematically in Figure 2.3. At the beginning of the process, the billets are typically heated to rolling start temperatures between 900 °C and 1200 °C in a walking - beam furnace. Immediately after the furnace, descaling is carried out on the billets to prevent scale from being introduced in the wire during rolling. At the beginning of the rolling process the rectangular shape of the billets is formed into a round shape. This reshaping happens primarily in the roughing mill and the intermediate mill which are labeled in Figure 2.3 with number 3 and 4. The final rolling steps take place in the finishing blocks, which consist of a row of individual rolling stands. In the special case of thermomechanical rolling, additional loops in the arrangement of the rolling line ensure sufficient time for cooling of the wire to lower final deformation temperatures. After rolling, the wires are coiled into rings with a diameter of around 1 m by a loop laying head. In the final step, the coiled wires are cooled down on a cooling conveyor under controlled conditions.

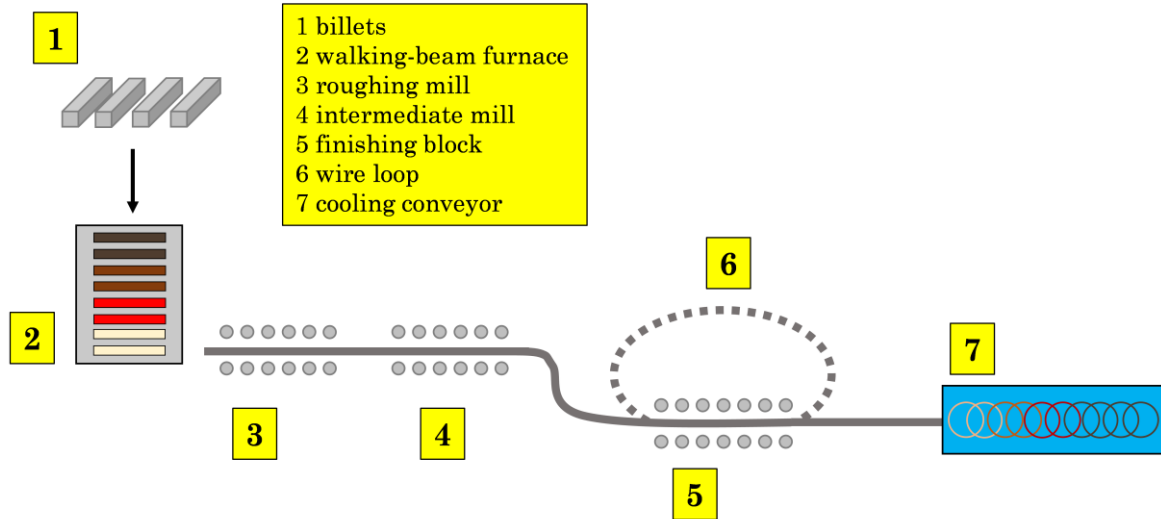


Figure 2.3: Schematic illustration of a typical wire rod rolling mill. Image adapted from [9].

2.3 Concept of microalloyed HSLA steels

Global steel production has been increasing for years, and reached a peak of 1.88 billion tons in 2020 [10], with microalloyed steels accounting for around 10 - 15 % in 2014 [5,11]. Microalloyed HSLA steels have a low C content of usually below 0.1 wt% and achieve the desired properties through a combination of TMCP and the addition of MAE, such as Nb, Ti and V [12]. These three MAE strongly influence the properties of the steels, both during rolling and afterwards, since these three MAE are responsible for the formation of the most relevant precipitates in HSLA steel, TiN, NbC and VC [13]. The equilibrium thermodynamics of the precipitates allow to describe the behavior of the precipitates during TMCP and their equilibrium solubility conditions can be expressed as:

$$\log_{10}[M][X] = \log_{10} K_{MX}^{phase} = -\frac{Q_{phase}}{RT} + B = -\frac{A}{T} + B \quad (1)$$

where M and X describe the concentration of the MAE and the interstitial element (e.g. C or N), respectively. K_{MX}^{phase} describes the phase - dependent (i.e. liquid, delta - ferrite, austenite and alpha - ferrite) equilibrium constant, Q_{phase} the phase - dependent activation energy, R is the universal gas constant and A and B are constants. The latter two constants A and B were determined in different studies in the past and are listed in detail in various reviews for Ti - [8,14], Nb - [7,14] and V [14,15] precipitates. A summary of selected values is listed in Table 1.

Table 1: Selected thermodynamic parameters of various MAE precipitates.

	A	B	Ref.
$\log[\text{Ti}][\text{N}]_{\text{liq.}}$	17040	6.40	[16]
$\log[\text{Ti}][\text{N}]_{\text{liq.}}$	12740	4.06	[17]
$\log[\text{Ti}][\text{N}]_{\text{Y}}$	15020	3.82	[18]
$\log[\text{Nb}][\text{C}]_{\text{Y}}$	7500	2.90	[19]
$\log[\text{Nb}][\text{C}+12/14\text{N}]_{\text{Y}}$	6770	2.26	[18]
$\log[\text{V}][\text{N}]_{\text{Y}}$	7700	2.86	[16]
$\log[\text{V}][\text{N}]_{\alpha}$	9700	3.90	[16]
$\log[\text{V}][\text{C}]_{\text{Y}}$	9500	6.75	[14]
$\log[\text{V}][\text{C}]_{\alpha}$	7050	4.24	[20]

By using the inhibitory effect of the precipitates against grain coarsening and recrystallization, it is possible with TMCP to obtain a fine - grained microstructure in the as - rolled condition. This in turn has a positive effect on both strength and toughness, since grain - refinement is the only mechanism without a negative effect on toughness when increasing strength.

Already in the early 1950s, Hall [21] and Petch [22] were able to establish the famous Hall - Petch equation (equation 2), which gives a relationship between the yield strength of a steel (σ_y) and its grain size (d).

$$\sigma_y = \sigma_0 + \frac{k_y}{\sqrt{d}} \quad (2)$$

In equation 2 both σ_0 and k_y are experimental constants depending on the material.

The ductile - brittle transition temperature (DBTT) can be used to describe the toughness of steels. Gladman et al. [23] were able to relate the DBTT to the chemical composition, the pearlite fraction (f_p), the concentration of interstitials (N_i) and the grain size of ferritic - pearlitic HSLA steels, which is described with equation 3.

$$DBTT = -19.0 + 44 * \text{wt}\%Si + 700 * \sqrt{\text{wt}\% N_i} + 2.2 f_p - \frac{11.5}{\sqrt{d}} \quad (3)$$

For martensitic steels it was shown by Wang et al. [24] that a decreasing package grain size has a positive effect on the DBTT. The fracture stress (σ_f) can be related to the package grain size (d_p) with equation 4.

$$\sigma_f = \sqrt{\frac{4E\gamma_p}{(1 - \nu^2)d_p}} \quad (4)$$

In equation 4 E describes the Young's modulus, γ_p is the plastic deformation energy, ν is Poisson's ratio and d_p is the package size. All three before mentioned equations again underline the importance of a fine microstructure to positively influence both strength and toughness.

Titanium

In order to avoid excessive grain coarsening, care must already be taken during annealing prior to rolling. Therefore, Ti is ideally suited and alloyed as a MAE, since it forms thermally stable TiN precipitates [8]. Although their size is normally too large to influence recrystallization, they have the desired property of inhibiting grain growth during annealing or welding [25]. Zener [26] was one of the first to derive a relation between the size and distribution of precipitates and the grain size, which is described with the following equation:

$$R_c = \frac{4r}{3f} \quad (5)$$

Here, R_c describes the critical grain radius from which grain growth is completely inhibited and r and f the particle size and volume fraction, respectively. The pinning of grain boundaries could be shown for particles with a size between 30 - 800 nm and a particle volume fraction of less than 0.01 [5].

Niobium

As an alloying element, Nb plays the most important role in the recrystallization behavior of microalloyed steels during rolling. Nb strongly inhibits the recrystallization, both through the solute drag effect and the formation of strain - induced precipitates and leads therefore to an increasing T_{NR} [2,7]. The solute drag effect refers to the increased occurrence of alloying elements, such as Nb, at grain boundaries and dislocations and this subsequently hinders their mobility [27,28]. A crucial variable regarding the solute drag effect is the difference between the atomic radius of the alloying element and Fe. For this reason, besides the MAE Nb and Ti, also other elements, such as Mo, Mn and P have a huge potential as solute drag elements [2,27]. Strain - induced NbC precipitates play a major role in inhibiting the recrystallization kinetics of microalloyed steels during deformation, which was investigated in several studies [29–34]. Deformation of the austenitic microstructure increases the number density of dislocations, deformation bands and subgrain structures, which serve as nucleation sites for precipitation and therefore leads to a higher number of strain - induced precipitates [31,35]. Although the recrystallization - inhibiting effect of both the solute drag effect and strain - induced

precipitates have been extensively studied in the past, there are still different opinions as to which of the two effects has a stronger influence. According to Speer et al. [36] and Cao et al. [37] the solute drag effects are relatively small compared to those of strain - induced Nb(C,N) precipitates, whereas other studies suggest the opposite [38]. From a more practical point of view, this question can be answered as follows: In order for strain - induced precipitates to form, they require a certain amount of induced deformation and time to nucleate and grow. The interpass time (i.e. the time between two rolling passes) differs for various rolling processes and is short in strip - or wire mills, and long in plate mills. This means that in processes with sufficient amount of deformation, strain rate and time, strain - induced precipitation effects become more and more dominant, whereas in other processes solute drag effects also play a major role in retarding recrystallization. Nevertheless, it must also be mentioned that the conditions in laboratory experiments (i.e. strain and strain rate) with regard to recrystallization behavior often differ significantly from the conditions in industrial rolling mills. However, since these parameters have a major impact on the formation of strain - induced precipitates [32], they play a bigger role in industrial large - scale processes with regard to recrystallization retarding effects than can be determined in laboratory tests. In addition to the here mentioned strain - induced precipitates in austenite, the selection of the right process parameters can also result in the formation of finest NbC precipitates in ferrite [35]. Due to their small size of around 1 - 5 nm [39] these precipitates also have the optimal size to contribute significantly to the strength of a material [40].

Vanadium

Although the steels examined in this work were alloyed without vanadium, this important MAE should also be briefly discussed in this section. Of all the transition elements used as MAE in HSLA steels, V carbides and nitrides have the highest solubility in austenite [12,15,41]. For this reason, these precipitates only play a minor role with regard to recrystallization during rolling (although reported in [15,42,43]) or grain coarsening during annealing or welding. Nevertheless, these precipitates formed later during the rolling processes make a major contribution to increasing strength and decreasing ferrite grain size. According to Lui and Jonas [44], V precipitates are typical representatives of type III precipitates during TMCP. This refers to precipitates that form at the austenite/ferrite interface during the austenite to ferrite phase transformation or which are formed directly in ferrite after the transformation. For V both, interphase precipitation [45–47] and precipitation from supersaturated ferrite [47] have been observed in the past. Lagneborg et al. [47] reported that in microalloyed steels with an

increased N content, VN precipitation can occur already at temperatures around 800 °C in the austenitic phase field. This subsequently leads to grain refinement of the ferritic structure, since these precipitates serve as ferrite nucleation sites during the transformation. It could be shown, that there is both an increase of nucleation sites along prior PAGB and intragranular nucleation [48–50]. In addition to grain refinement, the mechanism of precipitation strengthening is responsible for the increase in strength [51], which Orowan [52] already described as early as 1948. Zajac et al. [53] were able to show that the size and quantity of the precipitates depends on the V content of the alloy and that the size of the precipitates decreases with increasing V content, while their number increases at the same time. Furthermore, with regard to the increase of strength, it could be shown that the yield stress increases by 5 MPa per 0.001 wt% N.

Combined addition of MAE

The sources cited in this thesis so far have mainly dealt with the effect of a single MAE on the properties of the alloys. However, it must be mentioned that the different MAE influence each other mutually. For example, Kejian et al. [54] and Charleux et al. [40] studied the precipitation behavior of Nb and Ti microalloyed HSLA steels and its effect on strength. Charleux et al. [40] investigated a HSLA steel containing 860 ppm Nb and 470 ppm Ti and found very fine 1 nm small needlelike precipitates on dislocations in ferrite, which were held responsible for an increase in strength through precipitation hardening. Kejian et al. [54] found an opposite effect and observed reduced strength in an alloy concept with Ti (100 ppm and 220 ppm) and Nb (170 ppm) compared to one only containing Nb. The reason was that the addition of small amounts of Ti resulted in the formation of coarse (Ti,Nb) carbides. As a result, less Nb was present, increasing the strength through the formation of fine NbC precipitates. With regard for the recrystallization behavior, Hong et al. [55] observed a similar behavior. They did two - stage interrupted compression tests and saw that the size of NbC precipitates was smaller in a Nb and Ti alloyed steel compared to a steel only alloyed with Nb. They also observed a longer precipitation start time in the steel alloyed with Nb and Ti. The reason for this was that due to the formation of thermally stable (Ti,Nb)(C,N), less dissolved Nb was present in the matrix. Therefore, fewer strain - induced recrystallization - inhibiting NbC precipitates have formed.

In summary, it can be said that although it is possible to describe and modify the properties based on the microstructure, each alloy concept, including the manufacturing route, must be considered individually in order to obtain optimal properties.

2.4 Recovery and recrystallization

If metallic materials are deformed, the dislocation density (ρ) within the material increases. For example, ρ increases from 10^{10} m^{-2} to 10^{16} m^{-2} in a cold - worked metal [56,57], which leads to an increase in strength of the material [58]. At the same time, the system strives to reduce the thermodynamically unstable state, which can be achieved through recovery [56,59,60] and recrystallization [56,57,61].

In general, the activation energy of recovery is lower than that of recrystallization, which is why recovery processes take place already at lower temperatures compared to recrystallization processes. During recovery, on the one hand a redistribution and annihilation of point defects and dislocations takes place and on the other hand, there is a rearrangement of small - angle grain boundaries, the so - called polygonization [60]. Depending on whether the recovery takes place during or after deformation, it is referred to as dynamic (DRV) or static recovery (SRV).

With regard to the mobility of dislocations, the stacking fault energy (SFE) is an important variable. The SFE determines the distance between partial dislocations and therefore influences their mobility. Metals with a low SFE are characterized through a large separation between the partial dislocations and therefore the dislocation movement by gliding, climbing and cross - slipping is inhibited during plastic deformation. As a result, in metals with a low SFE, e.g. copper, silver, or austenitic stainless steels, recovery processes are inhibited and these metals tend to dynamically recrystallize faster [62,63].

The driving force behind recrystallization is the reduction in strain energy stored in the dislocations themselves [56]. The resulting reduction in free enthalpy (ΔG) is described in equation 6, whereas G is the shear modulus, b is the burgers vector and $\Delta\rho$ is the difference in dislocation density.

$$\Delta G \sim \Delta\rho G b^2 \tag{6}$$

Depending on when recrystallization occurs during deformation processes, it can be divided into dynamic (DRX) [63], metadynamic (MDRX) (or post - dynamic PDRX) [64], or static recrystallization (SRX) [62]. DRX and SRX are understood to mean those recrystallization processes that take place at the same time during deformation or afterwards, respectively, with the MDRX representing a special form, since it begins during deformation but continues after deformation.

In contrast to recovery, there is not just a rearrangement of small - angle grain boundaries (polygonization), but rather a direct formation of new grains and a globular microstructure with a low ρ through the formation of new high - angle grain boundaries.

In addition, recrystallization also needs a certain degree of critical deformation and a sufficiently high temperature, which for pure metals is around $0.4 \times T_m$ (melting temperature [K]) [57]. The recrystallization kinetics can be described using the so - called JMAK equation (equation 7), which was developed by Johnson and Mehl [65], Avrami [66–68] and Kolmogorov [69].

$$X(t) = 1 - \exp(-k_0 t^q) \quad (7)$$

Equation 7 describes the time - dependent course of the degree of recrystallized volume (X), where k_0 is a constant and q is the Avrami kinetic exponent. An example is given in Figure 2.4, which shows the time - dependent simulated recrystallization progress of a plastically strained aluminum single crystal and the corresponding simulated microstructure [70]. Furthermore, the grain size plays an important role in the kinetics of recrystallization processes. Since recrystallization starts at nucleation sites, such as grain boundaries, fine - grained microstructures show faster recrystallization kinetics, as these microstructures show a larger total area of grain boundaries [71].

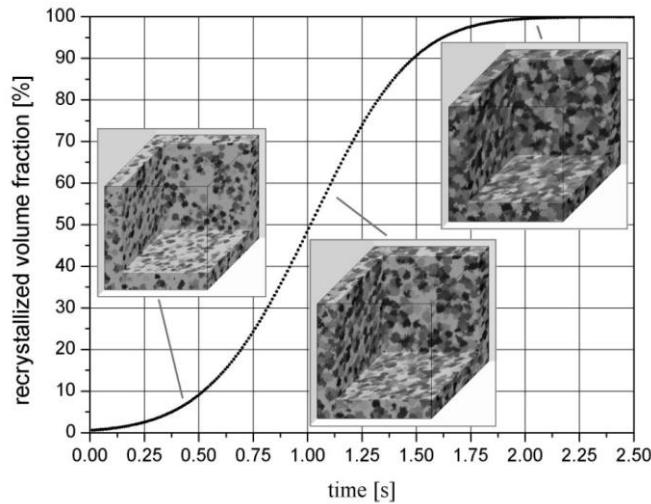


Figure 2.4: Simulated kinetics and microstructure of recrystallization in a plastically strained aluminum single crystal. Printed with permission from [70].

A critical degree of deformation ($\epsilon_{c,DRX}$) is required for DRX to take place during hot deformation (e.g. rolling). The reason for that is that during deformation, on the one hand there is a continuous generation of new dislocations, which leads to work hardening of the material. On the other hand, there is a competing mechanism, namely a softening due to the dislocation annihilation during DRV [72]. After a critical degree of deformation, the DRV is no longer rapid enough to annihilate the dislocations, which leads to an increase in dislocation density until a critical condition, at which the first recrystallization nuclei form. Experimentally, $\epsilon_{c,DRX}$ can be determined using the double - differentiation method

developed by Poliak et al. [73]. This method determines $\varepsilon_{c,DRX}$ from flow curves of compressed samples and was further simplified by Najafizadeh et al. [74]. After determining $\varepsilon_{c,DRX}$, it is also possible to calculate the fraction of dynamically recrystallized volume (X_{DRX}) generated during deformation using the following equation

$$X_{DRX} = 1 - \exp \left[-0.693 \left(\frac{\varepsilon - \varepsilon_{c,DRX}}{\varepsilon_p} \right)^m \right] \quad (8)$$

where ε is the strain, ε_p is the peak strain of the flow curve and m is a material constant.

DRX has been extensively studied in the past and a summary of this can be found in the review by Huang et al. [63]. A study by Ma et al. [75] shows how a combined addition of Nb and Ti affects the DRX of microalloyed steels. They examined different steels with a constant Nb concentration around 400 ppm and varying Ti contents between 0 and 230 ppm. To combine the Nb and Ti content in their models they used an “effective Nb content” ($[Nb]_{eff}$), which was calculated with the following equation:

$$[Nb]_{eff} = [Nb] + \beta[Ti] \quad (9)$$

where β is a multiplying factor and was chosen to be 0.33 in their study. It could be shown that with an increasing Ti content the activation energy for deformation increased, which led to an increased peak stress. According to the authors, a solute drag effect of the dissolved Ti and a precipitation pinning effect could be responsible for this. Furthermore, Ma et al. [75] could show that with an increasing Ti content the $\varepsilon_{c,DRX}/\varepsilon_p$ ratio decreased and the DRX kinetics were retarded, resulting in a lower value of m in equation 8.

Especially with regard to TMCP of HSLA steels, an understanding of static recrystallization processes is of utmost importance and the role of Nb [76–82], Ti [76,77,82,83] and V [76,79,82,84–86] were intensively studied by the group around Medina. As already mentioned in chapter 2.3, alloying these three MAE leads to delayed recrystallization kinetics and an increase of the T_{NR} , caused by the solute drag effect and pinning through strain - induced precipitates. The influence of the MAE on the T_{NR} is shown in Figure 2.5 [87] and can be described empirically using equation 10 developed by Boratto et al. [88].

$$T_{NR} = 887 + 464C + [6445Nb - 664(Nb)^{1/2}] + [732V - 230(V)^{1/2}] + 890Ti + 363Al - 357Si \quad (10)$$

Care must be taken when using this equation, as it is of empirical nature and neglects the preconditions of the steel prior to rolling.

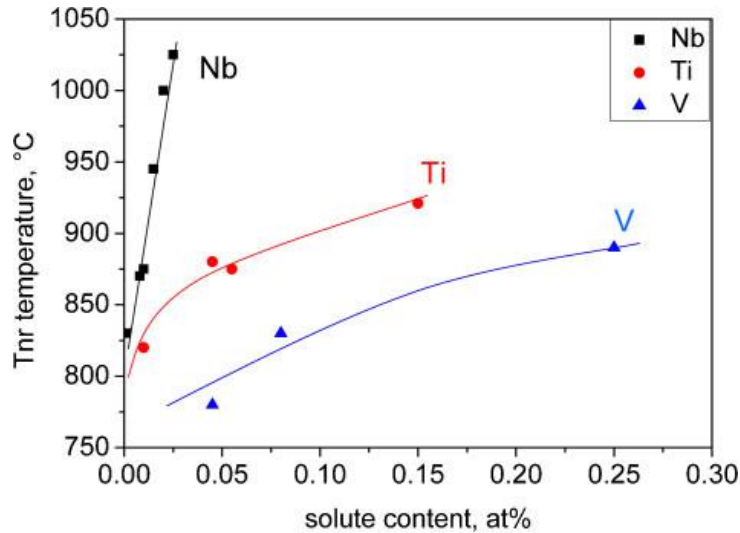


Figure 2.5: Influence of Nb, Ti and V in solute solution on the T_{NR} (0.07 wt% C, 1.4 wt% Mn and 0.25 wt% Si) [87].

Figure 2.6 shows a recrystallization diagram of a Nb alloyed HSLA steel (0.21 wt% C, 0.18 wt% Si, 1.08 wt% Mn and 0.024 wt% Nb) after torsion experiments with varying deformation temperatures [79]. First of all, it shows that the higher the deformation temperature, the faster the recrystallization processes. This is due to the higher mobility of the dislocations at elevated temperatures. Furthermore, this example also clearly shows the formation of plateaus in the recrystallization curves at deformation temperatures below 1050 °C. These plateaus indicate that recrystallization has stopped at this point due to the formation of strain - induced precipitates. This in turn can be used to preserve the flattened pancake structure in TMCP and subsequently to provide a larger number of nucleation sites for ferrite transformation.

As this example shows, it is not always easy to predict the exact processes inside the material, since the deformation parameters, but also recovery, recrystallization and precipitates mutually influence each other. This mutual interactions are illustrated schematically in Figure 2.7.

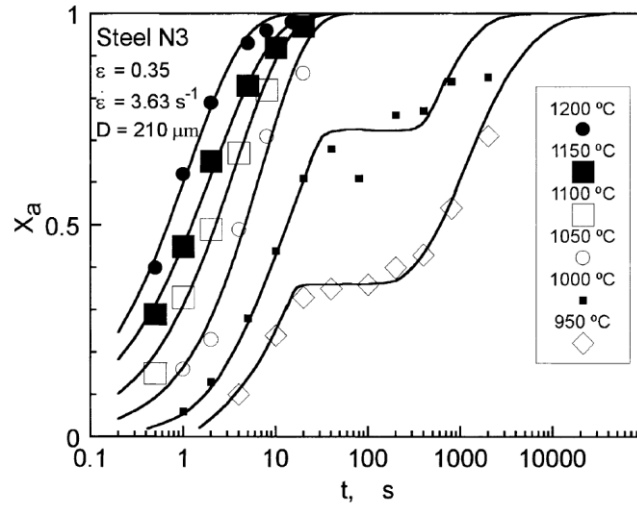


Figure 2.6: Recrystallization diagram of an HSLA steel (0.21 wt% C, 0.18 wt% Si, 1.08 wt% Mn and 0.024 wt% Nb) after varying deformation temperatures [79].

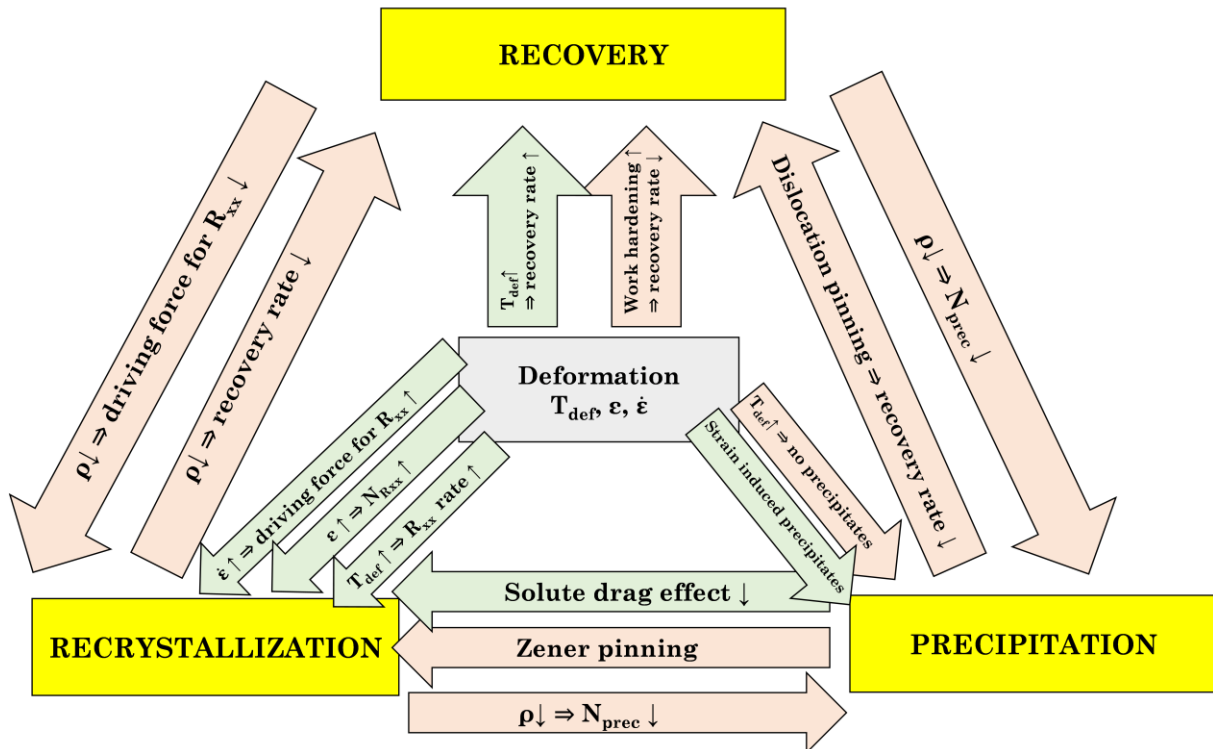


Figure 2.7: Schematic illustration of the mutual interactions between deformation, recovery, recrystallization and precipitation. Image adapted from [2].

2.5 Structure - property relationship of martensite

In ferrous alloys, such as steels, a quenching from the austenitic phase field leads to the formation of a martensitic microstructure. In the case of microalloyed HSLA steels the C content is usually below 0.25 wt% and while quenching from the austenitic phase these interstitial C atoms don't have sufficient time to diffuse, resulting in a displacive flip mechanism from a face - centered cubic austenitic microstructure (γ) to a body - centered tetragonal martensitic microstructure (α') [89]. In the case of α' martensite, different morphologies (see Figure 2.8) can occur depending on the C content and the martensite start temperature (M_s).

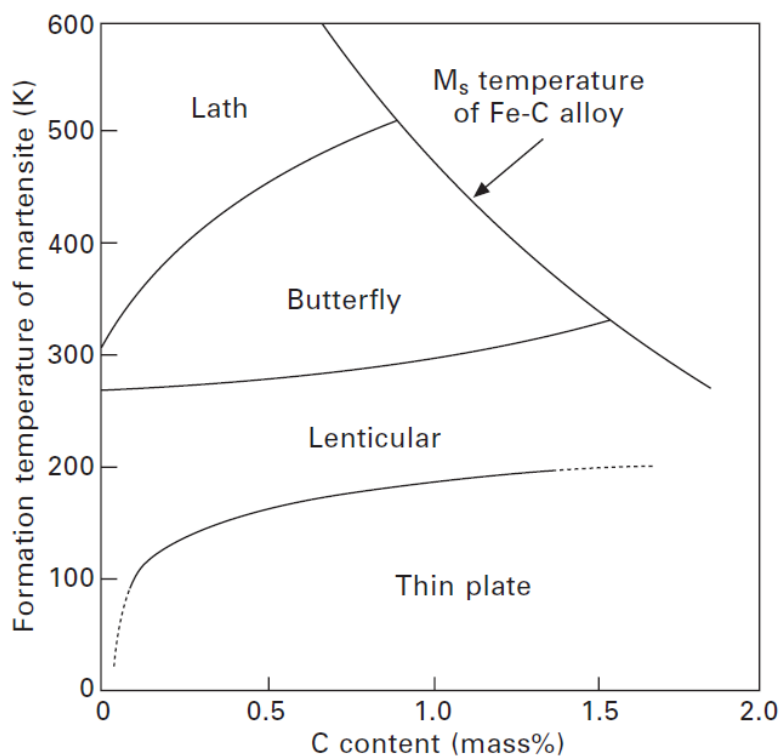


Figure 2.8: Various types of α' martensite, depending on the C content and M_s . Image reprinted with permission from [89,90].

Besides butterfly, lenticular and thin plate martensite, lath martensite is the most relevant in industrial steels, as it appears in most heat - treatable commercial steels. Therefore, its structural properties are described in more detail in this chapter. Morito et al. [91] used electron backscatter diffraction in a scanning electron microscope and Kikuchi diffraction patterns in a transmission electron microscope to investigate the microstructure of lath martensite for steels with various C contents between 0 to 0.6 wt%. Figure 2.9 displays a schematic summary of their results.

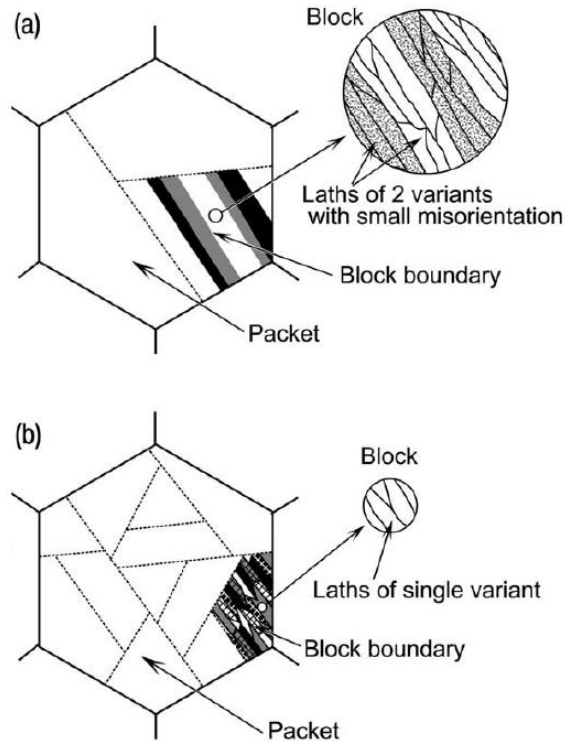


Figure 2.9: Schematic illustration of lath martensite in a steel with a C content of a) 0 - 0.4 wt% and b) 0.4 - 0.6 wt%. Image reprinted with permission from [91].

For steels with a C content between 0 to 0.4 wt% the prior austenite grain can be divided into packets which consist of parallel blocks, whereas each packet contains three blocks with different orientations. Furthermore, each block is divided into two sub - blocks each of which containing laths of a specific orientation. The laths are misoriented by a small angle around 10° . In high - carbon steels (0.4 - 0.6 wt% C) the prior austenite grain again is divided in packets. In this case, packets consist of fine blocks in the range of a few μm . A packet contains of six blocks and each block consists of laths with a specific orientation. Furthermore, it could be confirmed that there is a Kurdjumov-Sachs orientation relationship between the prior austenite grain and the martensite laths, whereas some laths seem to have a Nishiyama orientation relationship.

Already in the early 1970s, Inoue et al. [92] and Matsuda et al. [93] could show that mechanical properties, such as strength and toughness, are strongly related to the packet and block size of a martensitic microstructure.

Therefore, controlling the austenite grain size during rolling is of utmost importance for controlling the mechanical properties, as it could be shown by Furuwara et al. [94] and Wang et al. [24] that the packet and block size of a martensitic microstructure are directly related to the prior austenite grain size (see Figure 2.10). In contrast to the block and

packet size, there is hardly any correlation between the prior austenite grain size and the lath width, as reported by Morito et al. [95].

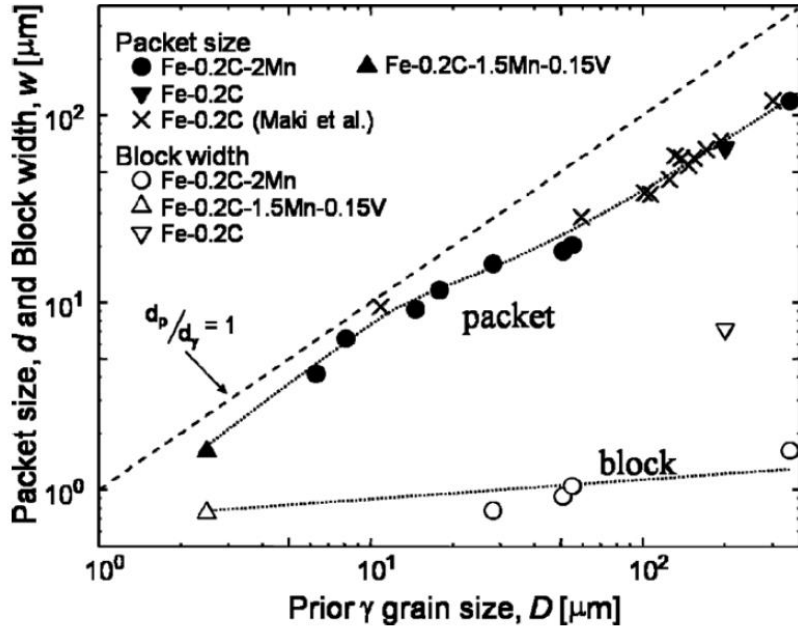


Figure 2.10: Relationship between the prior austenite grain size and the packet and block size [94].

Galindo-Nava et al. [96] investigated the relationship between the microstructure of martensitic microstructures and tempering conditions with its strength. They developed a model for determining the yield strength (σ_y) of martensitic microstructures, taking four strength - enhancing mechanism into account (1. solid solution strengthening, 2. grain boundary strengthening, 3. dislocation accumulation and 4. precipitation strengthening). Their model is described with the two following equations:

$$\sigma_{mart} = \frac{300}{\sqrt{d_{block}}} + 0.75\mu b\sqrt{\rho} \quad (11)$$

$$\sigma_y = \sigma_0 + \sum_i (\beta_i^2 x_i)^{1/2} + (\sigma_{mart}^2 + \sigma_p^2)^{1/2} \quad (12)$$

In equation 11 the effective martensite strength (σ_{mart}) sums up the grain boundary strengthening and the dislocation accumulation, whereas μ is the shear modulus, b the burgers vector, ρ the dislocation density and d_{block} the size of the martensite blocks. As equation 11 also shows, the martensite block size was used in the model of Galindo-Nava et al. [96] as decisive variable for the strength - increasing mechanism of grain boundary strengthening. This is based on previous research [97–99], which have shown that the

martensite block size is decisive for controlling the strength of martensitic microstructures and once again underlines the importance of grain refinement in martensite. In addition to the two strength mechanism already mentioned in equation 11, equation 12 also includes the proportions of solid solution strengthening and precipitation strengthening (σ_p). σ_0 is the lattice friction stress, x_i is the atom fraction of the substitutional element and β_i is the strengthening constant of the element.

With regard to toughness, Wang et al. [24] investigated the influence of different martensitic microstructures on the DBTT. They performed electron backscatter diffraction analysis along cleavage fracture surfaces and were able to show that martensite packets are extremely effective at deflecting cracks. This was shown by the fact that the cleavage facets were almost the same size as the martensite packets. Furthermore, they were able to show that the DBTT decreased with a decreasing packet size, which is shown in Figure 2.11. A similar result was obtained by Kaijalainen et al. [100], which were also able to show that the toughness improved with a decreasing prior austenite grain size and hence a finer martensitic microstructure. Through their investigations, they were also able to demonstrate the advantages of TMCP over conventional rolling routes. It was shown that a grain refinement of the austenite grain structure in a temperature regime in which recrystallization occurred also improved the toughness, but was less effective than a finishing rolling in the non - recrystallization temperature regime of TMCP.

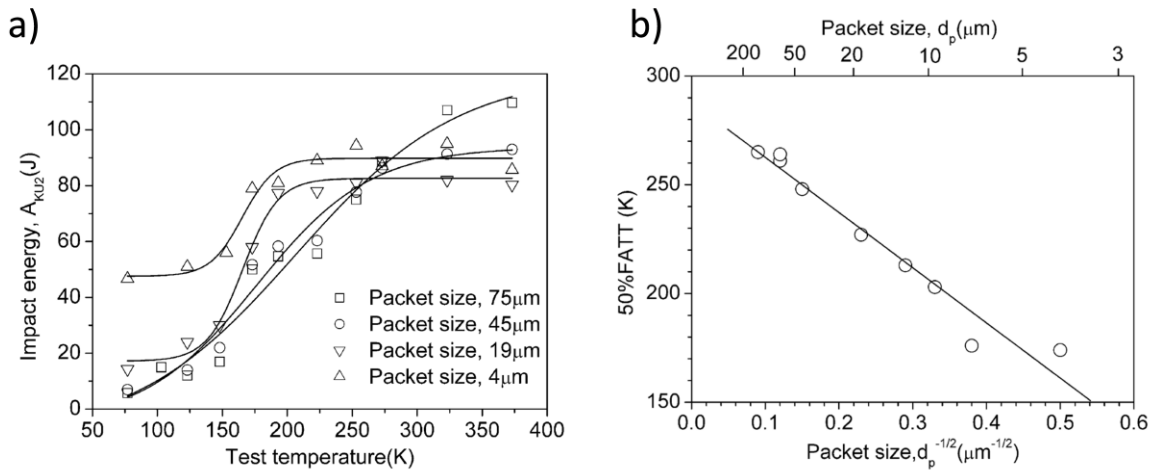


Figure 2.11: a) Impact energy dependent on the test temperature for specimens with various packet sizes. b) 50% FATT (fracture appearance transition temperature) as a function of the martensite packet size. Both images reprinted with permission from [24].

3 Experimental methods and challenges

3.1 Dilatometry

Dilatometry is a method that allows the measurement of the temperature - dependent changes in length of a sample. This makes it possible to determine material parameters, such as the thermal expansion coefficient (equation 13), or phase transformations during heating or cooling [101].

$$\alpha = \frac{1}{L_0} \frac{dL}{dT} \quad (13)$$

Equation 13 gives the relationship between the thermal expansion coefficient α , the initial sample length L_0 and the temperature - dependent change in length L . The experiment setup of conventional dilatometry is illustrated schematically in Figure 3.1. At the beginning of the experiment, the sample is clamped between two quartz push rods and connected to the control unit of a water-cooled induction coil via a thermocouple. In addition, before the start of the measurement, a vacuum is created in the sample chamber to prevent surface reactions during heating with the surrounding atmosphere. If the length of the sample changes as a result of heating, it is registered via a linear variable differential transformer (LVDT).

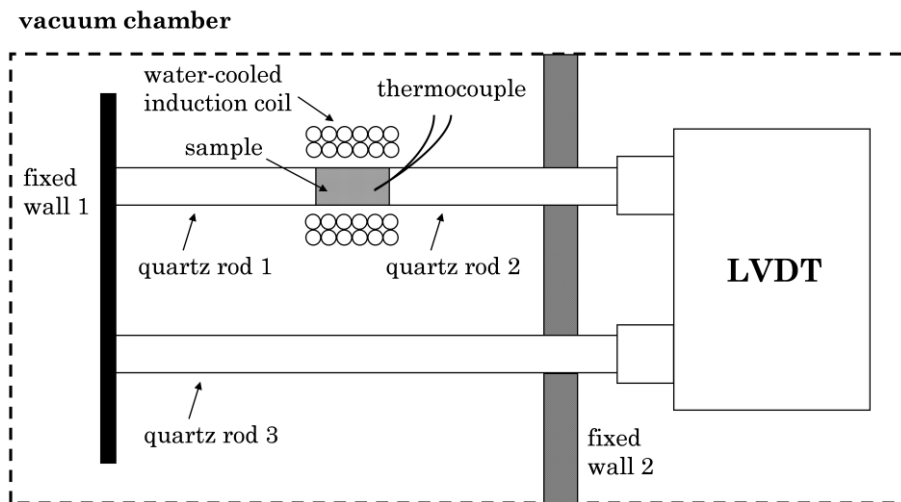


Figure 3.1: Schematic illustration of an experiment setup of a dilatometer for measuring changes in length.

A further development of dilatometry took place with the advent of tensile/compression/torsion deformation dilatometers. In addition of measuring the change of length, a deformation dilatometer offers also the possibility of introducing stress into the sample (an example of the experiment setup of a deformation dilatometer in compression mode is shown schematically in Figure 3.2). This makes it possible to

generate flow curves during deformation and to derive mechanical properties of the investigated material. Modern tensile/compression deformation dilatometers can be used in a temperature range between 20 °C and 1700 °C. They provide a maximum heating and cooling rate of around 100 K/s and achieve a length and temperature resolution of 50 nm and 0.05 °C, respectively. A commercially available deformation dilatometer from TA Instruments makes it possible to apply forces of up to 10 kN and enables deformation rates between 0.001 s⁻¹ and 10 s⁻¹ [102].

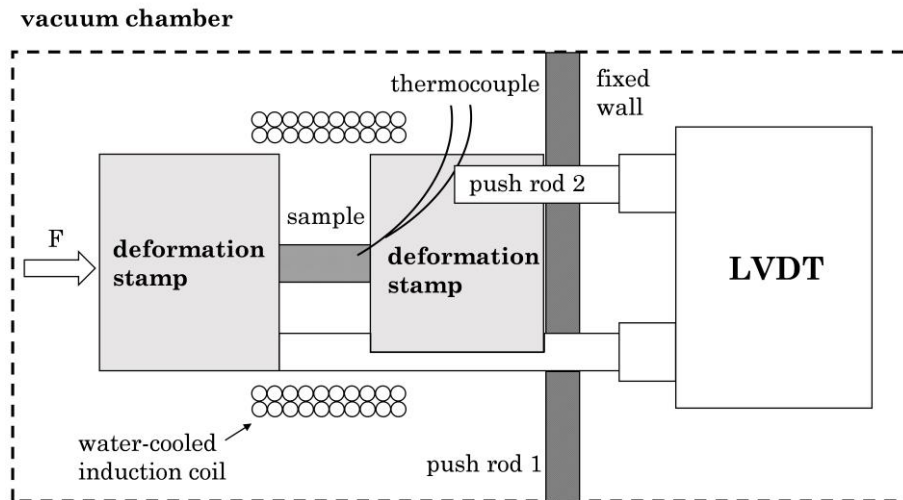


Figure 3.2: Schematic illustration of an experiment setup of a deformation dilatometer in compression mode.

As already described in chapter 2, an understanding of recovery and recrystallization processes is important for choosing the right rolling parameters in industrial large - scale TMCP. Certain experiments on deformation dilatometers, such as stress relaxation tests [103,104] and double - hit deformation tests [103,105], have prevailed in the past for investigating recrystallization kinetics in various materials. According to Vervynckt et al. [103], the latter are better suited to analyze the recrystallization behavior of microalloyed steels, as they are less sensitive to changes in the test setup compared to stress relaxation tests. Therefore, the recrystallization behavior of the steels examined in this thesis was also investigated using double - hit deformation tests, which is why this type of experiment is discussed in more detail in this section.

The measuring principle behind double - hit deformation tests is that the degree of recrystallization is calculated indirectly by comparing two flow curves recorded one after the other. A schematic illustration of the time - temperature - deformation schedule is given in Figure 3.3.

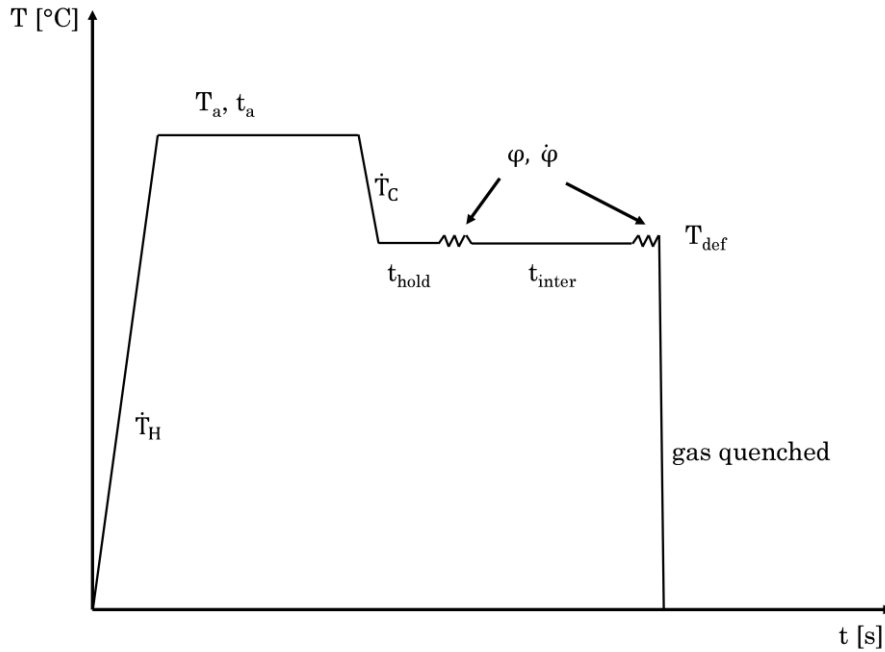


Figure 3.3: Schematic illustration of the time - temperature - deformation schedule of a double - hit deformation experiment.

At the beginning of the test the sample is heated with a certain heating rate (\dot{T}_H) to a desired annealing temperature (T_a) where the temperature is kept constant for a certain time (t_a). In the case of microalloyed steels, it is advisable to choose T_a and t_a in such a way that any microalloy precipitates dissolve during this annealing process in order to then be able to use the full potential of the strain - induced precipitates (for further information see chapter 2.3). After the annealing step the sample is cooled down with a certain cooling rate (\dot{T}_C) until it reaches the deformation temperature (T_{def}). After a short holding time (t_{hold}), which has the purpose of ensuring that the sample is heated evenly, the sample is compressed for the first time with a previously defined strain (φ) and strain rate ($\dot{\varphi}$). After the first compression the temperature is kept constant for a varying interpass time (t_{inter}) in order to be able to investigate the time - dependent recrystallization behavior. Finally, the second compression is carried out with the same compression parameters as the first compression and afterwards the sample is gas quenched as quickly as possible.

In the past, four methods for determining the degree of recrystallization after double - hit deformation tests have emerged, namely the 0.2 % or 2 % offset method [103], the back extrapolation method [78,106,107], the 5 % true strain method [30,103] and the mean flow stress method [108,109]. A schematic overview of these four methods and how the fractional softening (FS) can be calculated is shown in Figure 3.4. Strictly speaking, the fractional softening does not provide a value that can be attributed to 100 % to

recrystallization, since recrystallization and recovery processes overlap during deformation. For this reason, researchers have compared the calculated fractional softening of all four methods with the actual degree of recrystallization of the analyzed materials. It turned out that the 2 % offset method and the 5 % true strain method provide the best solution for the determination of the degree of recrystallization for microalloyed steels, since these two methods limit the effect of recovery on the fractional softening [103,110,111].

For the above mentioned reason and the fact that the 5 % true strain method provides also a simple way of calculating the fractional softening, this method was used to determine the degree of recrystallization for the steels examined in this thesis.

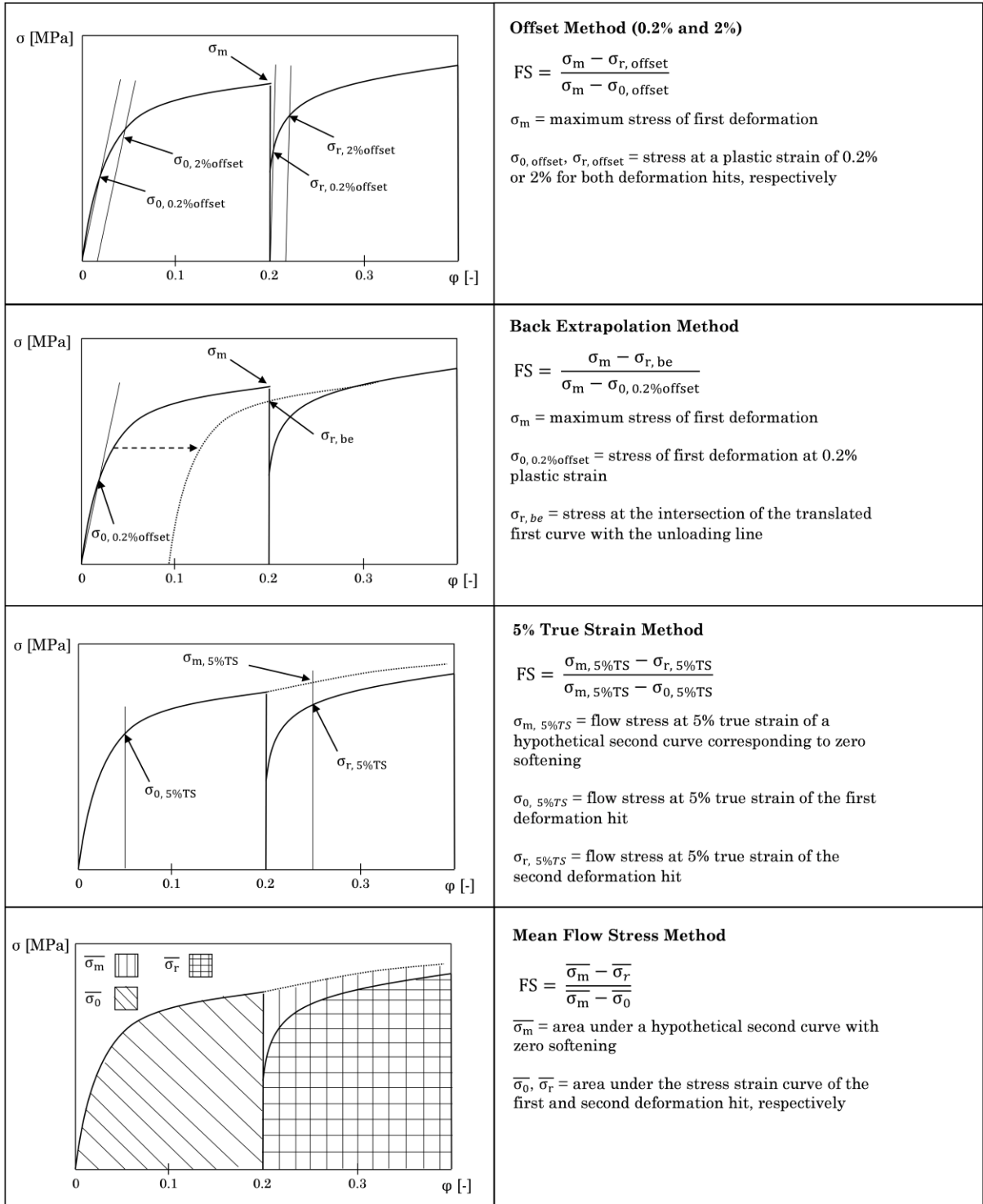


Figure 3.4: Schematic illustration of the four most used methods for the calculation of the degree of fractional softening, respectively, degree of recrystallization. Adapted from [105,112].

3.2 Atom probe tomography

APT is an extremely powerful tool for high - resolution characterization and thanks to its almost atomic spatial resolution has become a central element in the field of modern material science over the years. The measurement principle is illustrated schematically in Figure 3.5 and is based on field evaporation of atoms from a sharp tip (radius around 50 nm), which are accelerated as ions towards a detector by an applied electric field [113–115]. In order to even evaporate atoms from the APT tip it is necessary to apply a high electric field in the range of several GV/m between the tip and a local electrode.

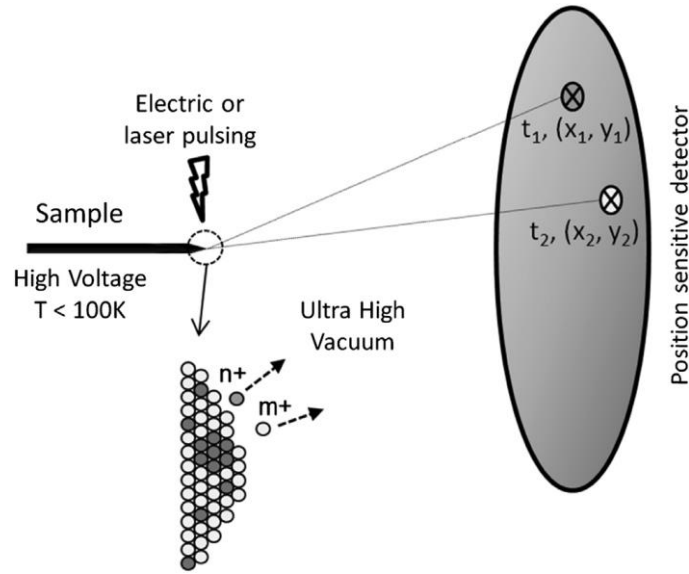


Figure 3.5: Schematic illustration of the measurement principle of an atom probe tomography measurement. Reprinted with permission from [113].

To understand why the tip needs to be this sharp for APT measurements, it is helpful to look at equation 14 for calculating the electric field (F)

$$F = \frac{V}{k_f * R} \quad (14)$$

Where V is the electric voltage between the tip and the local electrode, k_f is the so called field factor, which accounts for both the tip shape and its electrostatic environment and is around 2 - 10 [113] and R is the tip radius. Since the electric voltage that can be technically realized is limited in the kV range, it is therefore necessary to have the tip radius in the range of a few nm in order to achieve the desired electric field in the range of around 10 GV/m. During the measurement, the tip is in a high - vacuum chamber (chamber pressure is around 10^{-11} Torr) and is usually cooled to temperatures below 100 K. The evaporation process itself takes place after applying a basic electric voltage and the additional application of an electric voltage pulse or laser pulse (which enables

the tomography of poorly conducting materials as well). The evaporated ions are accelerated to a cross delay line detector and the mass - to - charge ratio can then be determined via the time - of - flight. The mass - to - charge ratio of each ion is summarized in a mass spectrum and by correlating the mass - to - charge ratios with the natural abundances of the isotopes, the peaks in the mass spectrum can be assigned to certain ion types. Thanks to the additional information of the impact position and the time of the impact on the detector, a three - dimensional reconstruction of the tip can then be created on a computer [116].

In the recent past, APT has been used more and more to study the precipitation characteristics of microalloyed steels [117–122]. As an example Nöhrer et al. [117] investigated the influence of different deformation parameters in the austenite/ferrite two phase region on the precipitation characteristics of Nb(C,N) precipitates. In addition to the classic two - stage electropolishing method [113], there is also the option of an in situ site - specific APT tip preparation using a focused ion beam microscope [123]. With the latter method, Webel et al. [120] were able to specifically analyze the precipitation characteristics of (Nb,Ti)(C,N) precipitates after various TMCP stages.

3.3 Transmission Kikuchi diffraction

Although APT is an important tool for characterizing precipitates, this technology is limited in terms of the size of the examined precipitates, as well as in characterizing their crystallographic properties. Up to a size of 50 nm, it is easily possible to examine precipitates using APT. For larger precipitates, on the other hand, TKD offers an alternative for high-resolution characterization [124]. A schematic illustration of a TKD arrangement in a scanning electron microscope (SEM) is depicted in Figure 3.6. The basic principle of TKD is similar to electron backscatter diffraction (EBSD), as in both cases the sample is in a SEM and the characterization is carried out by analyzing Kikuchi diffraction patterns using an EBSD detector and a suitable software. The key difference between the two mentioned methods is that TKD requires an electron transparent sample, which is not tilted towards the detector but backtilted away from it [125]. Thanks to this measurement setup the diffraction pattern originates from the bottom surface of the sample and therefore a smaller diffraction source volume. This in turn leads to an improved spatial resolution of down to 2 nm [126].

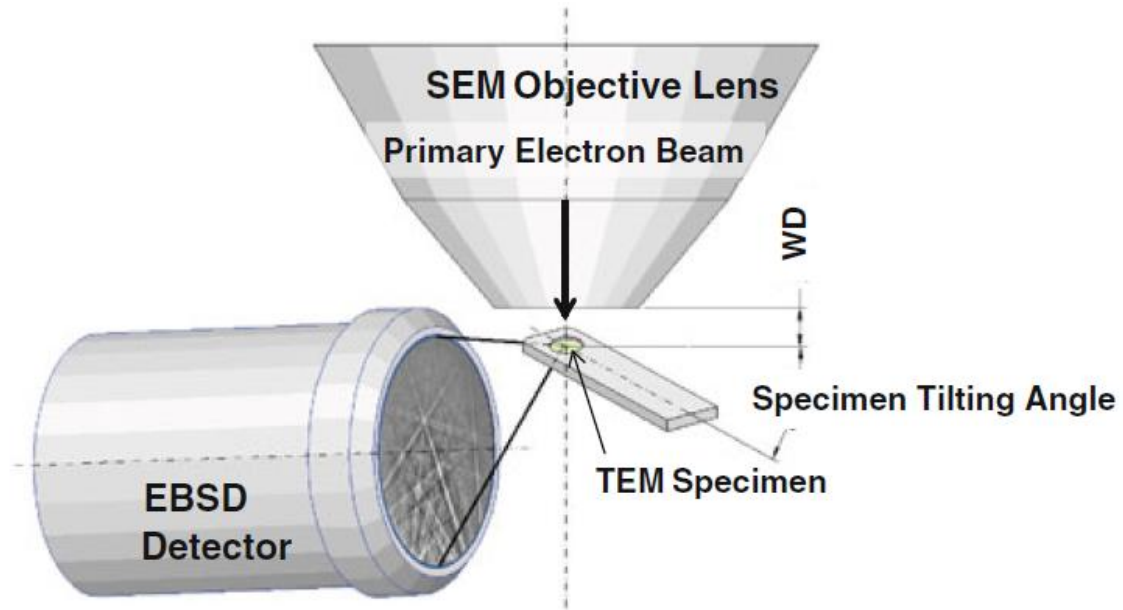


Figure 3.6: Schematic illustration of a TKD arrangement in a SEM. Reprinted with permission from [127].

In order to prevent the diffraction signal from the precipitates from being lost by the more dominant diffraction signal from the surrounding steel matrix, the precipitates of the investigated steels in this thesis were extracted from the matrix using the carbon replica method. A detailed step - by - step instruction of the method can be found in [128,129]. The method can be briefly summarized using the schematic illustration of the method in Figure 3.7. In a first step the sample is mounted in an investment compound (in the present case a PolyFast investment compound was used). In the next step the sample is ground with SiC paper and polished with a 1 μm diamond suspension. After the surface is polished, the samples are etched with a suitable etching solution for the respective steel (in the present case a common 3% nital etchant was used). This process is necessary so that the precipitates protrude from the sample surface. After the etching the sample is coated with carbon using a conventional carbon sputter coater. According to Bhattacharya et al. [128] the ideal thickness is around 100 nm. The surface of the coated samples is then carved in a grid pattern (in the present case a grid size of 2 mm was chosen) using a razor blade. Another etching follows. To do this, the sample is placed in the etching solution, which leads to a detaching of the carbon layer after a certain amount of time. In the final step, the carbon films are collected using a common 3 mm metal grid for transmission electron microscopy (TEM) characterization and the carbon layer is cleaned properly with alcohol and distilled water. After drying, the sample is ready to be used for TKD characterization.

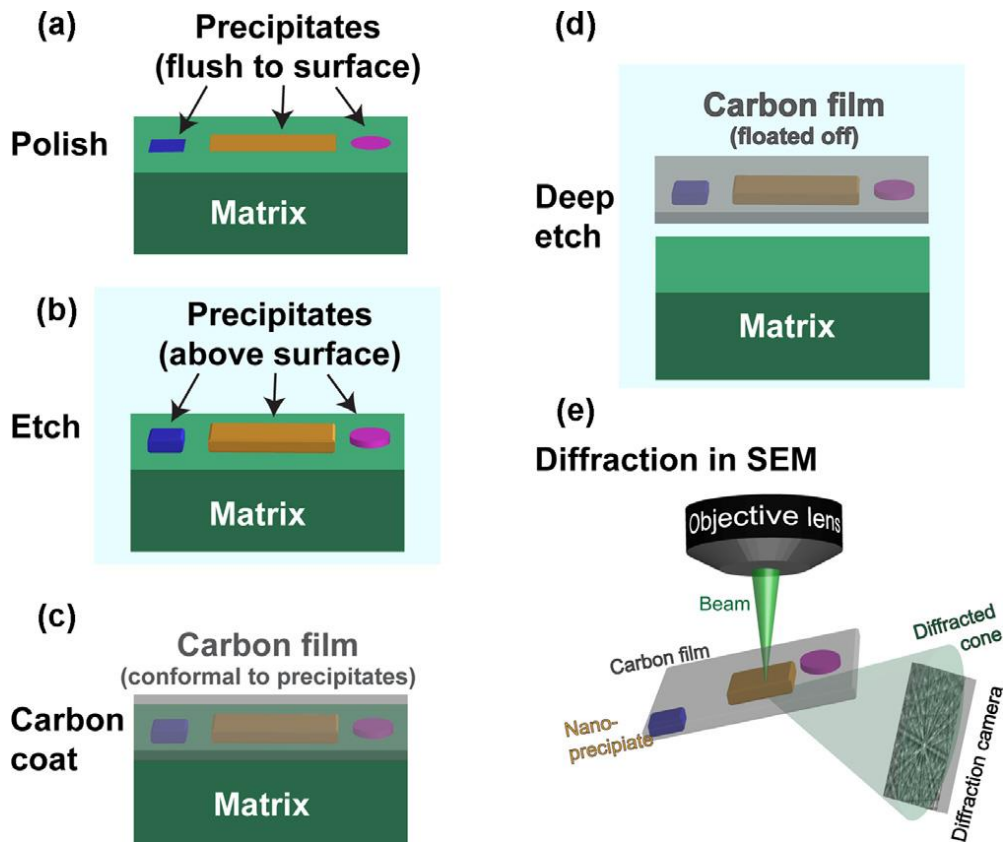


Figure 3.7: Schematic illustration of the extraction method in a) to d). a) The sample must be perfectly polished. b) After etching the precipitates protrude from the sample surface. c) The etched sample is coated with a 100 nm thin carbon layer. d) The carbon layer is detached from the sample containing the precipitates. e) A schematic illustration of the TKD arrangement in the SEM. Image reprinted with permission from [129].

4 Relation of the current thesis to the state of the art

The present work deals with the effects of various contents of MAE and TMCP parameters on the properties of microalloyed HSLA steels with C contents of more than 0.2 wt%. In the past, research in this field was mainly focused on microalloyed steels with lower C contents of usually below 0.1 wt%. A rising demand for increased strength and hardenability is pushing research in this field towards steels with higher C contents and aims to guarantee both high strength and toughness through a combination of TMCP and the addition of MAE.

Since an understanding of the recrystallization and recovery processes during TMCP is of decisive importance, a methodology was developed which has the future potential to automatically determine the degree of recrystallization of microalloyed steels using light optical microscopy (LOM). Furthermore, test alloys with C contents above 0.2 wt% and different MAE contents were produced by vacuum induction melting. A major focus was placed on the role of Ti and Nb microalloyed HSLA steels. To investigate the effect of the MAE on the grain growth - and recrystallization properties, annealing - and double - hit deformation experiments were carried out and the results compared to conventionally available microalloy - free reference alloys. In combination with high - resolution characterization methods, such as APT, STEM, TKD and energy dispersive X - ray diffraction (EDX) the relevant MAE precipitates itself and their influence on the structure - property relationships were investigated.

By choosing suitable TMCP parameters, it is possible to obtain a fine - grained ferritic microstructure in the as - rolled condition through the formation of dynamic strain - induced transformed (DSIT) ferrite. However, there is still a lack of knowledge regarding the exact mechanism of formation of DSIT ferrite. Therefore, part of this work aimed to investigate the microstructure, chemical composition, and crystallography of DSIT ferrite using APT, STEM, and EBSD to shed light on the formation mechanism of DSIT ferrite.

5 Published content

All appended publications are listed in the following chapter. In addition to the peer - reviewed papers, several theses were co - supervised. The co - supervised theses and one presentation at a conference are listed at the end of the chapter.

Contributions of the author: The author of this thesis is responsible for planning, conception and writing of all papers. The steel samples were provided by voestalpine Wire Rod Austria GmbH, Leoben, Austria and voestalpine Stahl Donawitz GmbH, Leoben, Austria. All investigations (i.e., experiments and data evaluation) were carried out at Montanuniversität Leoben and interpreted by the author of this thesis himself or under his supervision, with the following exceptions:

Paper I: The single - hit deformation experiments were performed with a deformation dilatometer DIL 805 A/D at the Institute of Materials Science, Joining and Forming at TU Graz, Graz, Austria by Nikolaus Kostwein and Thomas Fischer.

Paper III: The double - hit deformation experiments were performed with a deformation dilatometer DIL 805 A/D/T at TA Instruments, Hüllhorst, Germany by Fabian Schramme.

5.1 Appended peer - reviewed papers

Paper I: Stefan Monschein, Nikolaus Kostwein, Katharina S. Ragger, Dominik Zügner, Josef Fasching and Ronald Schnitzer

Determination of the degree of recrystallization of a microalloyed HSLA steel by using metallographic methods / Ermittlung des Rekristallisationsgrads eines mikrolegierten HSLA - Stahls unter Verwendung metallographischer Methoden

Practical Metallography 59 (2022), 6, 317-339; DOI: 10.1515/pm-2022-1007

Paper II: Stefan Monschein, Marlene Kapp, Dominik Zügner, Josef Fasching, Andreas Landefeld and Ronald Schnitzer

Influence of Microalloying Elements and Deformation Parameters on the Recrystallization and Precipitation Behavior of Two Low-Alloyed Steels

steel research international 2021, 2100065; DOI: 10.1002/srin.202100065

Paper III: Stefan Monschein, Katharina S. Ragger, Dominik Zügner, Josef Fasching and Ronald Schnitzer

Influence of the Ti Content on the Grain Stability and the Recrystallization Behavior of Nb Alloyed HSLA Steels

steel research international 2022, 2200094; DOI: 10.1002/srin.202200094

Paper IV: Stefan Monschein, Katharina S. Ragger, Josef Fasching, Dominik Zügner and Ronald Schnitzer

Microstructural, Chemical and Crystallographic Investigations of Dynamic Strain-Induced Ferrite in a Microalloyed QT Steel

Metals 2022, 12, 313; DOI: 10.3390/met12020313

Paper I

Stefan Monschein, Nikolaus Kostwein, Katharina S. Ragger, Dominik Zügner, Josef Fasching and Ronald Schnitzer

Determination of the degree of recrystallization of a microalloyed HSLA steel by using metallographic methods / Ermittlung des Rekrystallisationsgrads eines mikrolegierten HSLA - Stahls unter Verwendung metallographischer Methoden

Practical Metallography 59 (2022), 6, 317-339;

DOI: 10.1515/pm-2022-1007

S. Monschein, N. Kostwein, K. S. Ragger, D. Zügner, J. Fasching, R. Schnitzer

Determination of the degree of recrystallization of a microalloyed HSLA steel by using metallographic methods

Ermittlung des Rekristallisationsgrads eines mikrolegierten HSLA-Stahls unter Verwendung metallographischer Methoden

Received: March 25, 2022

Accepted: April 25, 2022

Translation: E. Engert

Eingegangen: 25. März 2022

Angenommen: 25. April 2022

Abstract

On the one hand, this work aims at describing the grain elongation of compressed samples of a microalloyed high-strength steel using appropriate parameters. On the other hand, the degree of recrystallization is to be determined based on the samples' grain elongation. For this purpose, single-hit compression tests were performed with varying test parameter settings using a de-

Kurzfassung

Ziel dieser Arbeit war es einerseits die Kornstreckung von gestauchten Proben eines mikrolegierten hochfesten Stahls durch geeignete Parameter zu beschreiben und andererseits anhand der Kornstreckung den Rekristallisationsgrad der Proben zu ermitteln. Hierfür wurden mit Hilfe eines Umformdilatometers Einzelstauchversuche mit variierenden Versuchsparametern durchgeführt, um Proben mit unterschiedli-

Authors:

Stefan Monschein, Nikolaus Kostwein, Ronald Schnitzer Department of Materials Science, Montanuniversität Leoben, Franz Josef-Straße 18, 8700 Leoben, Austria; E-Mail: stefan.monschein@unileoben.ac.at

Katharina S. Ragger voestalpine Wire Rod Austria GmbH, Drahtstraße 1, 8792 St. Peter-Freienstein, Austria

Dominik Zügner voestalpine Forschungsservicegesellschaft Donawitz GmbH, Kerpelystraße 199, 8700 Leoben, Austria

Josef Fasching voestalpine Stahl Donawitz GmbH, Kerpelystraße 199, 8700 Leoben, Austria

formation dilatometer to generate samples characterized by various degrees of recrystallization. Three parameters were chosen to describe the grain elongation. It was found that the parameter defining the ratio length/width of the original grain provides the highest sensitivity regarding changes in the grain elongation. Aiming at determining the degree of recrystallization, a critical grain elongation threshold value was determined below which it is assumed that a grain is recrystallized. The results show that choosing the right threshold value allows an automated determination of the degree of recrystallization of a microalloyed high-strength steel in the light microscope.

Keywords: *Static recrystallization, HSLA steel, single-hit compression tests, metallographic analysis of prior austenite grains*

1 Introduction

High-strength low-alloyed (HSLA) steels belong to the group of microalloyed steels. Owing to a combination of thermomechanical rolling processes and the addition of microalloying elements such as niobium, titanium or vanadium, they are characterized by excellent strength and toughness while also providing good weldability and processability [1]. Thermomechanical rolling processes are to provide a possibly fine-grained microstructure which has a positive impact on both strength and toughness [2]. When niobium is added, the non-recrystallization temperature (T_{NR}), the temperature below which no complete recrystallization of the microstructure occurs between the rolling steps, will rise [3]. This can be explained by the solute-drag effect [3, 4] as well as by the formation of strain-induced NbC precipitates [3, 5]. During thermomechanical rolling, these effects are deliberately sought to obtain a non-recrystallized, flattened post finish rolling "pancake structure". Owing to the great number of nucleation sites, subse-

chen Rekristallisationsgraden zu erzeugen. Für die Beschreibung der Kornstreckung wurden drei Parameter gewählt, wobei sich zeigte, dass jener Parameter, der das Längen-zu-Breiten-Verhältnis des Originalkorns beschreibt, die größte Sensitivität im Hinblick auf Veränderungen der Kornstreckung liefert. Für die Bestimmung des Rekristallisationsgrads wurde ein kritischer Grenzwert der Kornstreckung ermittelt, unter welchem ein Korn als rekristallisiert angenommen wurde. Die Ergebnisse zeigen, dass die Wahl des richtigen Grenzwerts eine automatisierte lichtmikroskopische Bestimmung des Rekristallisationsgrads eines mikrolegierten hochfesten Stahls ermöglicht.

Schlagwörter: *statische Rekristallisation, HSLA Stahl, Einzelstauchversuche, metallographische Analyse ehemaliger Austenitkörner*

1 Einleitung

Hochfeste niedriglegierte (HSLA, „engl.: high-strength low-alloyed“) Stähle zählen zur Gruppe der mikrolegierten Stähle und erreichen durch eine Kombination von thermomechanischen Walzprozessen und der Zugabe von Mikrolegierungselementen, wie zum Beispiel Niob, Titan oder Vanadium, hervorragende Festigkeiten und Zähigkeiten bei ebenso guter Schweiß- und Verarbeitbarkeit [1]. Das Ziel der thermomechanischen Walzprozesse besteht darin, ein möglichst feinkörniges Gefüge nach dem Walzen zu erhalten, da dieses gleichzeitig sowohl die Festigkeit, als auch Zähigkeit positiv beeinflusst [2]. Durch die Zugabe von Niob steigt die Rekristallisationsstoptemperatur (T_{NR} , „engl.: non-recrystallization temperature“) an, die jene Temperatur ist, unter der es zu keiner vollständigen Rekristallisation des Gefüges zwischen den Walzschritten kommt [3]. Erklärt werden kann dies einerseits durch den „Solute-Drag“-Effekt [3, 4], als auch durch die Bildung dehnungsinduzierter NbC-Ausscheidungen [3, 5]. Beim thermomechanischen Walzen werden diese Effekte bewusst

quent cooling induces a fine-grained microstructure. As early as when choosing the furnace temperature, attention must be paid to bring into solution the niobium present in the alloy to take full advantage of the positive effect of niobium during the thermomechanical rolling process. The material is therefore typically annealed in the range of about 1200 °C thus increasing the risk of grain coarsening. For this reason, titanium is used as an additional alloying element. On the one hand, it forms thermally stable TiN precipitates which, at elevated temperatures, inhibit the grain growth. On the other hand, due to its high affinity for nitrogen, titanium inhibits the formation of Nb(C,N) which facilitates the dissolution of NbC precipitates [2, 6]. The kinetics of the microalloying precipitates as well as the recrystallization behavior are highly dependent on the choice of parameters for the rolling process. Another aspect to be taken into account is the fact that the microalloying elements may themselves interact. Studies already provide evidence for such interactions of niobium and titanium [7–10]. It is therefore imperative to understand the effect of microalloying elements on the precipitation kinetics and the recrystallization behavior to choose the optimum rolling parameters.

In the past, double-hit compression tests have proven their worth in investigating the influence of the temperature, the degree of deformation, and the rate of deformation on the static recrystallization and the precipitation behavior of microalloyed steels [8, 11–15]. These tests represent an indirect method for the determination of the statistical recrystallization based on analyzing the flow curves of two consecutive compressions. However, these tests have the disadvantage of an elaborate sample preparation and the fact that the degree of recrystallization of

gewählt, um nach dem Endwalzen eine nicht rekristallisierte, flachgedrückte Gefügestruktur („engl.: pancake structure“) zu erhalten. Bei der anschließenden Abkühlung resultiert daraus, aufgrund der großen Anzahl an Keimstellen, ein feinkörniges Gefüge. Um die positive Wirkung von Niob beim thermomechanischen Walzen optimal nutzen zu können, muss bereits durch die Wahl der Ofentemperatur darauf geachtet werden, das in der Legierung befindliche Niob in Lösung zu bringen. Üblicherweise wird daher im Bereich um 1200 °C geglüht, wodurch das Risiko von Kornvergrößerung erhöht wird. Aus diesem Grund kommt Titan als weiteres Legierungselement zum Einsatz. Dieses bildet einerseits thermisch stabile TiN-Ausscheidungen, welche das Kornwachstum bei erhöhten Temperaturen hemmen. Andererseits hindert Titan aufgrund der hohen Affinität zu Stickstoff die Bildung von Nb(C,N), was das Auflösen von NbC-Ausscheidungen begünstigt [2, 6]. Die Kinetik der Mikrolegierungsausscheidungen als auch das Rekristallisationsverhalten sind stark abhängig von der Wahl der Parameter während des Walzprozesses. Ebenfalls muss berücksichtigt werden, dass es zu einer Wechselwirkung der Mikrolegierungselemente selbst kommen kann, die für Niob und Titan bereits in Studien gezeigt wurde [7–10]. Für die Wahl der optimalen Walzparameter ist ein Verständnis der Wirkungsweise der Mikrolegierungselemente auf die Ausscheidungskinetik und das Rekristallisationsverhalten daher essentiell.

In der Vergangenheit haben sich Doppelstauchversuche („engl.: double-hit deformation tests“) bewährt, um den Einfluss von Temperatur, Umformgrad und Umformrate auf die statische Rekristallisation sowie das Ausscheidungsverhalten mikrolegierter Stähle zu untersuchen [8, 11–15]. Bei diesen Versuchen handelt es sich um eine indirekte Methode zur Bestimmung der statischen Rekristallisation durch Analyse der Fließkurven zweier aufeinanderfolgender Stauchungen. Ein Nachteil dieser Versuche ist jedoch einerseits die aufwendige Probenfertigung und andererseits,

rolled products cannot be directly determined in the as-rolled condition.

Therefore, other indirect and direct methods, such as metallographic methods using the light optical microscopy (LOM) [16–19], microhardness measurements [20, 21], or electron backscatter diffraction, provide an alternative for the determination of the degree of recrystallization [20–22].

Light microscopes are part of the standard metallography equipment. Determining the degree of recrystallization using light-optical methods is thus the simplest and cheapest of the above mentioned possibilities. The basic principle of this technique used to determine the recrystallization degree of steels is to “freeze” the deformed austenitic microstructure by direct quenching from the austenite region which induces the formation of a martensitic microstructure. A suitable etching methodology using picric acid offers the possibility to reveal the prior austenite grain boundaries (PAGB) [23, 24]. In previous works, the degree of recrystallization was determined from the ratio of the recrystallized grains' intersections to the total number of all intersections using a line intercept method [17, 19]. However, one disadvantage of this method is the fact that one must decide for each and every single grain whether it is considered a recrystallized or a non-recrystallized grain which complicates an automated evaluation of the degree of recrystallization.

As part of this work, deformation dilatometer compression tests were performed on a microalloyed HSLA steel aiming at producing samples with different degrees of recrystallization. Here, the main objective was to develop a methodology to directly determine

dass der Rekristallisationsgrad von gewalzten Produkten nicht direkt im walzharten Zustand ermittelt werden kann.

Als Alternative bieten sich daher weitere indirekte sowie direkte Methoden für die Bestimmung des Rekristallisationsgrads an, wie beispielsweise lichtmikroskopische (LIMI) metallographische Methoden [16–19], Mikrohärtmessungen [20, 21] oder die Elektronenrückstreubeugung („engl.: electron backscatter diffraction“) [20–22].

Ein Lichtmikroskop zählt zum Standardrepertoire in der Metallographie, weswegen die Ermittlung des Rekristallisationsgrads durch lichtoptische Methoden die vergleichsweise einfachste und günstigste der oben genannten Möglichkeiten bietet. Das Grundprinzip dieser Technik bei der Ermittlung des Rekristallisationsgrads von Stählen besteht darin, das verformte austenitische Gefüge durch direktes Abschrecken aus dem Austenitgebiet einzufrieren, wodurch es zur Ausbildung eines martensitischen Gefüges kommt. Durch die Wahl einer geeigneten, auf Pikrinsäure basierenden Ätzmethodik ist es anschließend möglich, die ehemaligen Austenitkorgrenzen (PAGB, „engl.: prior austenite grain boundaries“) sichtbar zu machen [23, 24]. Mittels eines Linienschnittverfahrens wurde in vergangenen Arbeiten [17, 19] der Rekristallisationsgrad aus dem Verhältnis der Schnittpunkte der rekristallisierten Körner zur Gesamtzahl aller Schnittpunkte ermittelt. Ein Nachteil dieser Methodik besteht jedoch darin, dass für jedes einzelne Korn individuell bestimmt werden muss, ob dieses zu den rekristallisierten oder nicht rekristallisierten Körnern gezählt wird. Dies erschwert eine automatisierte Auswertung des Rekristallisationsgrads.

In dieser Arbeit wurden mit einem Umformdilatometer Einzelstauchversuche an einem mikrolegierten HSLA-Stahl durchgeführt, mit dem Ziel, Proben mit unterschiedlichen Rekristallisationsgraden zu erzeugen. Das Hauptziel dieser Arbeit war es, eine Methodik

the degree of recrystallization of compressed samples in the light microscope. For this purpose, a grain elongation threshold value was used as a measure to decide whether a grain is considered as recrystallized or non-recrystallized. Therefore, this work also aims at defining the grain elongation based on appropriate parameters and at comparing these parameters. The time-dependent degree of recrystallization of the steel examined in this work was already subject of prior double-hit compression tests and investigations by the authors [8]. Thus, the results of the prior published work could be used to determine suitable parameters to determine the recrystallization degree from the analysis of the grain elongation.

2 Experimental Work

Table 1 outlines the chemical composition of the examined microalloyed steel.

Single-hit compression tests were performed applying varying test parameters to produce samples with various degrees of recrystallization. The single-hit compression tests were carried out using a TA Instruments dilatometer DIL 805 A/D. The samples had a diameter of 5 mm and a length of 10 mm. They were manufactured by machining from rolled starting material. A type S thermocouple was welded to the samples to control the temperature during the test.

	C	Mn	Ni	Cr	Mo	Si	Nb	Ti	Fe
m%	0.22	1.27	0.48	0.49	0.24	0.22	0.026	0.015	bal.

Table 1: Chemical composition of the examined microalloyed steel.

Tabelle 1: Chemische Zusammensetzung des untersuchten mikrolegierten Stahls.

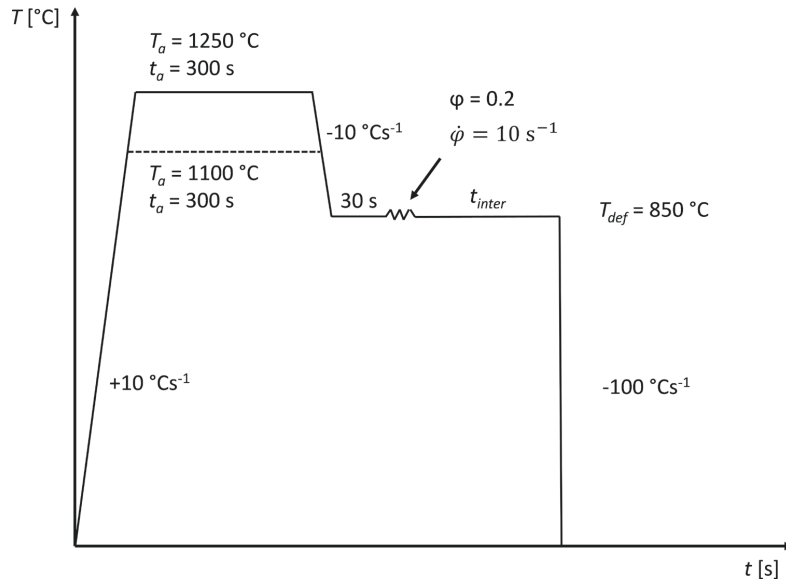
zu entwickeln, um den Rekristallisationsgrad von gestauchten Proben direkt lichtmikroskopisch zu ermitteln. Hierfür wurde ein Grenzwert der Kornstreckung als Maß herangezogen, um zu entscheiden, ob ein Korn als rekristallisiert oder nicht rekristallisiert angenommen wird. Aus diesem Grund war es ein weiteres Ziel dieser Arbeit, die Kornstreckung über geeignete Parameter zu definieren und diese miteinander zu vergleichen. Der zeitabhängige Rekristallisationsgrad des in dieser Arbeit untersuchten Stahls wurde von den Autoren bereits vorab durch Doppelstauchversuche untersucht [8], weswegen die Ergebnisse der vorab publizierten Arbeit verwendet werden konnten, um geeignete Parameter für die Ermittlung des Rekristallisationsgrads aus der Analyse der Kornstreckung zu ermitteln.

2 Experimentelle Arbeit

Die chemische Zusammensetzung des untersuchten mikrolegierten Stahls befindet sich in Tabelle 1.

Um Proben mit unterschiedlichen Rekristallisationsgraden zu erzeugen wurden Einzelstauchversuche mit variierenden Versuchsparametern durchgeführt. Die Einzelstauchversuche wurden mit einem Dilatometer DIL 805 A/D der Firma TA Instruments realisiert. Die Proben hatten einen Durchmesser von 5 mm und eine Länge von 10 mm und wurden durch zerspannende Methoden aus dem gewalzten Ausgangsmaterial gefertigt. Um die Temperatur während des Versuchs zu steuern wurde ein Thermoelement Typ S an den Proben angeschweißt.

Figure 1: Schematic representation of the time-temperature-deformation schedule for the single-hit compression tests. Step 1: heating the sample to the annealing temperature $T_a = 1100^\circ\text{C}$ or 1250°C at a heating rate of $+10^\circ\text{Cs}^{-1}$; step 2: holding time for the annealing temperature $t_a = 300$ s; step 3: cooling down to the deformation temperature T_{def} of 850°C at a cooling rate of -10°Cs^{-1} ; step 4: holding time of 30 s to ensure a uniform heating of the sample cross section; step 5: compression of the sample at a degree of



deformation φ of 0,2 and a rate of deformation $\dot{\varphi} = 10 \text{ s}^{-1}$; step 6: holding the T_{def} for different holding times (t_{inter}) between 0 and 2000 s; step 7: quenching of the samples at a quenching rate of -100°Cs^{-1} .

Bild 1: Schematische Darstellung des Zeit-Temperatur-Umform-Verlaufs der Einzelstauchversuche. Schritt 1: Aufheizen der Probe auf Glühtemperatur $T_a = 1100^\circ\text{C}$, bzw. 1250°C mit einer Aufheizrate von $+10^\circ\text{Cs}^{-1}$; Schritt 2: Haltezeit der Glühtemperatur $t_a = 300$ s; Schritt 3: Abkühlen auf die Umformtemperatur $T_{def} = 850^\circ\text{C}$ mit einer Kühlrate von -10°Cs^{-1} ; Schritt 4: Haltezeit von 30 s, um eine gleichmäßige Durchwärmung des Probenquerschnitts zu gewährleisten; Schritt 5: Stauchung der Probe mit einem Umformgrad $\varphi = 0,2$ und einer Umformrate $\dot{\varphi} = 10 \text{ s}^{-1}$; Schritt 6: Halten der T_{def} für unterschiedliche Haltezeiten (t_{inter}) zwischen 0 und 2000 s; Schritt 7: Abschrecken der Proben mit einer Abschreckgeschwindigkeit von -100°Cs^{-1} .

Figure 1 is a schematic illustration of the time-temperature-deformation schedule of the single-hit compression tests. In the first series of tests, the samples were heated to an annealing temperature (T_a) of 1100°C at a heating rate of $+10^\circ\text{Cs}^{-1}$. After an annealing time (t_a) of 300 s, they were cooled down to the deformation temperature (T_{def}) of 850°C at a cooling rate of -10°Cs^{-1} . After a holding time of 30 s, which was to ensure a uniform temperature profile along the sample cross section, the samples were compressed up to a degree of deformation (φ) of 0.2 at a strain rate ($\dot{\varphi}$) of 10 s^{-1} . After the deformation, different holding times (t_{inter}) between 0 and 2000 s were applied for T_{def} to analyze the influence of time on the recrystallization progress. The samples were directly quenched from the austenite region

Bild 1 zeigt schematisch den Temperatur-Zeit-Umform-Verlauf der durchgeführten Einzelstauchversuche. Die Proben wurden in der ersten Versuchsreihe mit einer Heizrate von $+10^\circ\text{Cs}^{-1}$ auf eine Glühtemperatur (T_a) von 1100°C aufgeheizt und nach einer Glühzeit (t_a) von 300 s mit einer Abkühlrate von -10°Cs^{-1} auf die Umformtemperatur (T_{def}) von 850°C abgekühlt. Nach einer Haltezeit von 30 s, welche einen gleichmäßigen Temperaturverlauf entlang des Probenquerschnitts gewährleisten sollte, wurden die Proben mit einer Dehnrates ($\dot{\varphi}$) von 10 s^{-1} bis zu einem Umformgrad (φ) von 0,2 gestaucht. Um den Einfluss der Zeit auf den Rekristallisationsfortschritt zu untersuchen wurde T_{def} nach der Umformung für unterschiedliche Haltezeiten (t_{inter}) zwischen 0 und 2000 s gehalten. Abschließend wurden die Proben mit einer Abkühlrate von -100°Cs^{-1}

at a cooling rate of $-100\text{ }^{\circ}\text{C}\cdot\text{s}^{-1}$ resulting in a martensitic microstructure. In addition to the first series of tests, a second series was performed at a T_a of $1250\text{ }^{\circ}\text{C}$. The remaining test parameters were kept the same in both series of tests.

After the single-hit compression tests, the samples were cut in longitudinal direction to examine the microstructure of the compressed and quenched samples. The cut samples were mounted with the aid of a hot mounting press. They were ground up to a grit of 4000 using SiC grinding paper and subsequently polished up to a grit of $1\text{ }\mu\text{m}$ with diamond suspension. The polished samples were etched using the CRIDA CHEMIE etchant CRIDA QT plus to reveal the PAGB structure within the martensitic microstructure. For this purpose, the freshly polished samples were thoroughly cleaned using isopropanol and immersed in the etching solution for 15 minutes at room temperature. When the etching attack was weak or insufficient, the samples were cleaned using isopropanol and re-polished for a minute using a $1\text{ }\mu\text{m}$ diamond suspension. Subsequent to a second isopropanol cleaning process, the re-polished samples were immersed in the etching solution for another 5–10 minutes. The structure of the PAGB was made visible using a ZEISS light microscope Axio Imager M1. At least three LOM images were acquired of adjacent positions of the compressed samples for the quantitative evaluation of the grain elongation to obtain statistical information on the determined grain elongation values (see Figure 2). In this context, the magnification of the microscope was chosen such that the image contained between 400 and 600 grains.

The quantitative evaluation of the grain elongation was carried out using the image analysis software MIPAR 3.3.4. The software not only allows an automated identifi-

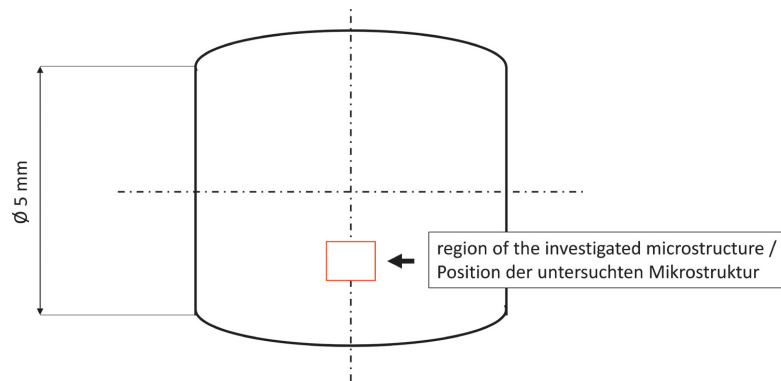
direkt aus dem Austenitgebiet abgeschreckt, wodurch sich ein martensitisches Gefüge ausbildete. Zusätzlich wurde zur ersten Versuchsreihe eine zweite Versuchsreihe mit einer T_a von $1250\text{ }^{\circ}\text{C}$ durchgeführt. Die restlichen Versuchsparameter blieben in beiden Versuchsreihen gleich.

Um die Mikrostruktur der gestauchten und abgeschreckten Proben untersuchen zu können, wurden diese nach den Einzelstauchversuchen in Längsrichtung zerteilt. Die zerteilten Proben wurden mit einer Warmeinbettpresse eingebettet, mit SiC-Schleifpapier bis zu einer Körnung von 4000 geschliffen und anschließend bis zu einer Körnung von $1\text{ }\mu\text{m}$ mit Diamantsuspension poliert. Um die Struktur der PAGB innerhalb des martensitischen Gefüges sichtbar zu machen, wurden die polierten Proben mit dem Ätzmittel CRIDA QT plus der Firma CRIDA CHEMIE geätzt. Hierzu wurden die frisch polierten Proben gründlich mit Isopropanol gereinigt und bei Raumtemperatur für 15 Minuten in die Ätzlösung gelegt. Im Fall eines schwachen, beziehungsweise unzureichenden Ätzangriffs, wurden die Proben mit Isopropanol gereinigt und circa eine Minute mit einer Diamantsuspension von $1\text{ }\mu\text{m}$ nachpoliert. Nach einer erneuten Reinigung mit Isopropanol wurden die nachpolierten Proben für weitere 5-10 Minuten in die Ätzlösung getaucht. Die Struktur der PAGB wurde mittels Lichtmikroskopie unter Verwendung eines ZEISS Axio Imager M1 Mikroskops sichtbar gemacht. Für die quantitative Auswertung der Kornstreckung wurden mindestens drei LOM-Aufnahmen an benachbarten Positionen der gestauchten Proben angefertigt, um eine statistische Aussage über die ermittelten Werte der Kornstreckung zu erhalten (siehe Bild 2). Dabei wurde die Vergrößerung des Mikroskops so gewählt, dass sich innerhalb der Aufnahme zwischen 400 und 600 Körner befanden.

Die quantitative Auswertung der Kornstreckung erfolgte mit der Bildanalysesoftware MIPAR 3.3.4. Diese Software ermöglicht einerseits eine automatisierte Erkennung der einzel-

Figure 2: Schematic representation of the compressed samples to illustrate the position of the examined microstructure.

Bild 2: Skizze der gestauchten Proben zur Beschreibung der Position der untersuchten Mikrostruktur.



cation of individual grains but also provides a description of the grains' shape based on various parameters. Three different parameters were applied in the present work to quantitatively determine the grain elongation: the Y/X aspect ratio ($AR_{Y/X}$) described in formula 1, the a/b aspect ratio ($AR_{a/b}$) described in formula 2, and the eccentricity (E) described in formula 3.

$$AR_{Y/X} = \frac{Y}{X} \quad (1)$$

$$AR_{a/b} = \frac{a}{b} \quad (2)$$

$$E = \frac{\sqrt{a^2 - b^2}}{a} \quad (3)$$

In formula 1, Y and X describe the maximum grain diameters in the vertical and horizontal image direction of the respective grain. In order for $AR_{Y/X}$ to be used, the LOM image needs to be oriented in a way such that the samples' compression plane in the longitudinal section runs parallel to the vertical image axis. An ellipse was fitted into each grain using the evaluation software in order to determine $AR_{a/b}$ and E, where a describes the length of the major axis and b the length of the minor axis of the fitted ellipse. Figure 3 shows a LOM image of an etched sample

nen Körner und ermöglicht andererseits die Kornform durch unterschiedliche Parameter beschreiben zu können. In vorliegender Arbeit wurden für die quantitative Bestimmung der Kornstreckung drei unterschiedliche Parameter herangezogen: das Y/X-Seitenverhältnis ($AR_{Y/X}$, „engl.: Y/X-aspect-ratio“), welches durch Formel 1 beschrieben wird; das a/b-Seitenverhältnis ($AR_{a/b}$, „engl.: a/b-aspect-ratio“), welches durch Formel 2 beschrieben wird und die Exzentrizität (E), welche durch Formel 3 beschrieben wird.

$$AR_{Y/X} = \frac{Y}{X} \quad (1)$$

$$AR_{a/b} = \frac{a}{b} \quad (2)$$

$$E = \frac{\sqrt{a^2 - b^2}}{a} \quad (3)$$

In Formel 1 beschreiben Y und X die maximalen Korndurchmesser in vertikaler sowie horizontaler Bildrichtung des jeweiligen Kornes. Für die Verwendung des $AR_{Y/X}$ war es daher erforderlich, die LIMI-Aufnahme so auszurichten, dass die Stauchebene der Proben im Längsschliff parallel zur vertikalen Bildachse war. Für die Bestimmung von $AR_{a/b}$ sowie von E wurde durch die Auswertesoftware eine Ellipse in jedes Korn gefittet, wobei a die Länge der Hauptachse und b die Länge der Nebenachse der gefitteten Ellipse beschreibt. Bild 3 zeigt eine LIMI-Aufnahme eines geätzten

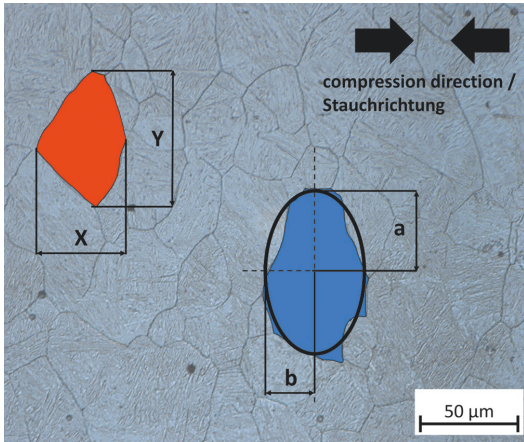


Figure 3: LOM image of an etched section of a compressed sample after a $T_a = 1250^\circ\text{C}$ and $t_{\text{inter}} = 10\text{ s}$. The red and blue grains are to illustrate the grain parameters Y , X , a , and b .

Bild 3: LIMI-Aufnahme eines geätzten Schiffs einer gestauchten Probe nach einer $T_a = 1250^\circ\text{C}$ und $t_{\text{inter}} = 10\text{ s}$. Das rote und blaue Korn dienen zur Veranschaulichung der Kornparameter Y , X , a und b .

section subsequent to a single-hit compression test after a T_a of 1250°C and a t_{inter} of 10 s as well as a schematic illustration of the grain shape using the grain parameters Y , X , a , and b .

The curves were normalized in order to improve the comparability of the time-dependent profile of the grain elongation (see formula 4).

$$e_{g,\text{norm},i} = \frac{e_{g,i}}{e_{g,t0}} \quad (4)$$

Formula 4 describes the determination of the normalized grain elongation ($e_{g,\text{norm}}$), where $e_{g,i}$ is the grain elongation after $t_{\text{inter}} = i$ and $e_{g,t0}$ is the mean grain elongation after a t_{inter} of 0 s (direct quenching after compression).

In [8], the recrystallization behavior was indirectly determined from the flow curve of two successive compressions. The tests in the present work differ only in that the samples were directly quenched after t_{inter} . As the degree of recrystallization is a function of t_{inter} , the same degree of recrystallization was obtained, regardless of whether a second compression was carried out. Therefore, the recrystallization values indirectly determined by the authors [8] can be used in this work to determine appropriate pa-

Schiffs einer Probe nach einem Einzelstauchversuch nach einer $T_a = 1250^\circ\text{C}$ und einer $t_{\text{inter}} = 10\text{ s}$, sowie schematisch die Beschreibung der Kornform durch die Kornparameter Y , X , a und b .

Um die zeitabhängigen Verläufe der Kornstreckung besser vergleichbar zu machen, wurden die Kurven normiert (siehe Formel 4).

$$e_{g,\text{norm},i} = \frac{e_{g,i}}{e_{g,t0}} \quad (4)$$

Formel 4 beschreibt die Ermittlung der normierten Kornstreckung ($e_{g,\text{norm}}$, „engl.: normalized grain elongation“), wobei $e_{g,i}$ die Kornstreckung nach einer $t_{\text{inter}} = i$ und $e_{g,t0}$ die mittlere Kornstreckung nach einer $t_{\text{inter}} = 0\text{ s}$ beschreibt (direktes Abschrecken nach der Stauchung).

In [8] wurde das Rekristallisationsverhalten indirekt über den Verlauf der Fließspannung von zwei aufeinanderfolgenden Stauchungen ermittelt. Die Versuche in vorliegender Arbeit unterscheiden sich dahingehend lediglich darin, dass die Proben nach t_{inter} direkt abgeschreckt wurden. Da der Rekristallisationsgrad abhängig ist von t_{inter} , hat sich unabhängig davon ob eine zweite Stauchung durchgeführt wurde, in beiden Fällen der gleiche Rekristallisationsgrad eingestellt. Aus diesem Grund können die von den Autoren [8] indirekt ermittelten Rekristallisationswerte

rameters for the light microscope analysis of the degree of recrystallization.

Similar to what *Chen et al.* [20] described for the examination of an aluminum alloy, a criterion was introduced in this work which defines when a grain is considered as recrystallized. A critical threshold value (f_{crit}) was defined as a criterion for the three parameters of the grain elongation ($AR_{y/x}$, $AR_{a/b}$, and E). The degree of recrystallization (R_{xx}) of the microstructure is subsequently obtained from formula 5:

$$R_{xx} = \frac{A_{Rxx}}{A_{total}} \quad (5)$$

Here, A_{Rxx} describes the total area of all recrystallized grains in the respective LOM image, whereas A_{total} is the total area of all grains, regardless of whether they are recrystallized or not.

The aim of the work was to choose f_{crit} for $AR_{y/x}$, $AR_{a/b}$, and E such that a difference between the recrystallization values determined from formula 5 and the values previously determined by the authors [8] is as small as possible. For this purpose, f_{crit} was varied and the results were plotted together with the results of the double-hit compression test. In order for the deviation of the curves showing the recrystallization values of the double-hit compression tests [8] and the recrystallization values of the light microscope examinations after the single-hit compression tests to be quantified, the Euclidean distance (d_E) between the measurement values was used. This process is described in formula 6:

$$d_E = \sqrt{\sum_{i=1}^n (Rxx_{i,DH} - Rxx_{i,SH})^2} \quad (6)$$

Thus, the degree of recrystallization after the double-hit compression tests at the time i ($Rxx_{i,DH}$) and the mean value of the degree of

herangezogen werden, um geeignete Parameter für die lichtmikroskopische Analyse des Rekristallisationsgrads in dieser Arbeit zu ermitteln.

Ähnlich wie von *Chen et al.* [20] für die Untersuchung einer Aluminium-Legierung beschrieben, wurde in dieser Arbeit ein Kriterium eingeführt, welches definiert, wann ein Korn als rekristallisiert angesehen wird. Als Kriterium wurde für die drei Parameter der Kornstreckung ($AR_{y/x}$, $AR_{a/b}$ und E) ein kritischer Grenzwert (f_{crit}) definiert. Der Rekristallisationsgrad (R_{xx}) des Gefüges ergibt sich anschließend aus Formel 5:

$$R_{xx} = \frac{A_{Rxx}}{A_{total}} \quad (5)$$

Hierbei beschreibt A_{Rxx} die Gesamtfläche aller in der jeweiligen LIMI-Aufnahme rekristallisierten Körner und A_{total} die Gesamtfläche aller Körner, unabhängig ob rekristallisiert, oder nicht.

Ziel dieser Arbeit war es für $AR_{y/x}$, $AR_{a/b}$ und E f_{crit} so zu wählen, dass zwischen den aus Formel 5 ermittelten Rekristallisationswerten und den vorab von den Autoren [8] ermittelten Werten eine möglichst geringe Differenz besteht. Hierfür wurde f_{crit} variiert und die Ergebnisse gemeinsam mit den Ergebnissen der Doppelstauchversuche geplottet. Um die Abweichung der Kurven der Rekristallisationswerte der Doppelstauchversuche [8] und der Rekristallisationswerte der lichtmikroskopischen Untersuchungen nach den Einzelstauchversuchen quantifizierbar zu machen, wurde der euklidische Abstand (d_E) zwischen den Messwerten als Maß hierfür herangezogen. Dies ist in Formel 6 beschrieben:

$$d_E = \sqrt{\sum_{i=1}^n (Rxx_{i,DH} - Rxx_{i,SH})^2} \quad (6)$$

Für die Bestimmung von d_E zwischen den Ergebnissen der Doppelstauchversuche und der Einzelstauchversuche benötigt man dem-

recrystallization after the single-hit compression tests at the same instant ($Rxx_{i,SH}$) is required in order to determine d_E between the results of the double-hit compression tests and the single-hit compression tests. In general, the progression of the curves becomes increasingly similar with decreasing d_E .

nach den Rekrystallisationsgrad nach den Doppelstauchversuchen zum Zeitpunkt i ($Rxx_{i,DH}$) sowie den Mittelwert des Rekrystallisationsgrads nach den Einzelstauchversuchen zum jeweils selben Zeitpunkt ($Rxx_{i,SH}$). Generell gilt, dass der Verlauf der Kurven mit sinkendem d_E ähnlicher wird.

3 Results

3 Ergebnisse

3.1 Quantitative determination of the grain elongation

3.1 Quantitative Bestimmung der Kornstreckung

Figure 4 shows the progression of the $e_{g,norm}$ curve over time after the single-hit compression tests, described by the three parameters $AR_{Y/X}$, $AR_{a/b}$ and E for different T_a , respectively. Figure 4a shows the value chart for a T_a of 1100 °C in which a temporal decrease of the grain elongation can be observed for all three parameters. The highest decrease of $e_{g,norm} = 0.92$ at a t_{inter} of 10 s to 0.70 at a t_{inter} of 2000 s can be observed for $AR_{Y/X}$, whereas the grain elongation for $AR_{a/b}$ only decreases from 0.95 to 0.80 and from 0.97 to 0.90 for E . For a t_{inter} of between 100 s and 300 s, the $e_{g,norm}$ curves for $AR_{a/b}$ and E

Bild 4 zeigt den zeitlichen Verlauf der $e_{g,norm}$ nach den Einzelstauchversuchen, jeweils beschrieben durch die drei Parameter $AR_{Y/X}$, $AR_{a/b}$ und E für unterschiedliche T_a . Bild 4a zeigt den Verlauf für eine T_a von 1100 °C, wobei eine zeitliche Abnahme der Kornstreckung für alle drei Parameter ersichtlich wird. Die stärkste Abnahme der $e_{g,norm}$ von 0,92 bei einer t_{inter} von 10 s auf 0,70 bei einer t_{inter} von 2000 s ist für $AR_{Y/X}$ zu beobachten, wohingegen die Kornstreckung für $AR_{a/b}$ lediglich von 0,95 auf 0,80 und bei E von 0,97 auf 0,90 abnimmt. Der $e_{g,norm}$ -Verlauf des $AR_{a/b}$ und der E zeigt zwischen einer t_{inter} von 100 s bis 300 s ein Abfla-

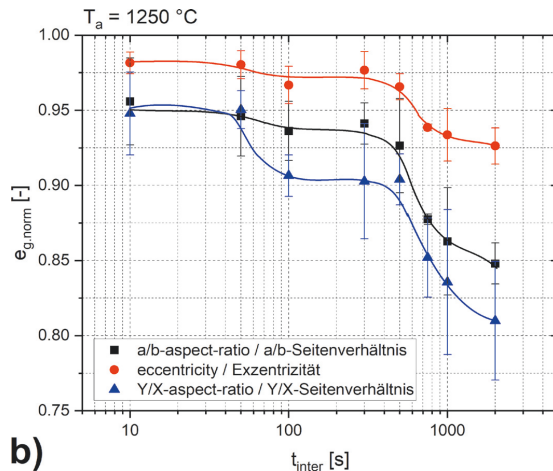
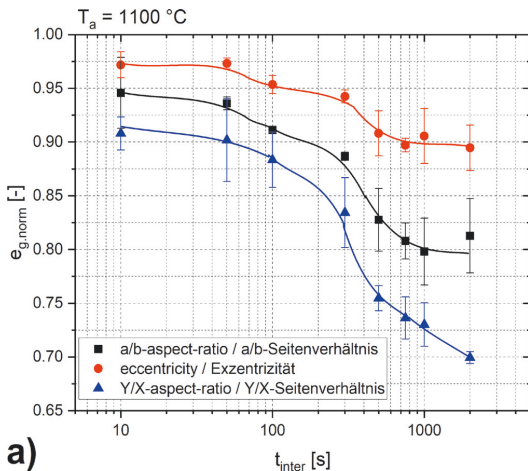


Figure 4a and b: Profile of $e_{g,norm}$ over time after the single compression tests, described by the parameters $AR_{Y/X}$, $AR_{a/b}$ and E for a T_a of a) 1100 °C and b) 1250 °C.

Bild 4a und b: zeitlicher Verlauf von $e_{g,norm}$ nach den Einzelstauchversuchen, beschrieben durch die Parameter $AR_{Y/X}$, $AR_{a/b}$ und E für eine T_a von a) 1100 °C und b) 1250 °C.

flatten. Figure 4b shows the progression of the $e_{g,norm}$ curve for $T_a = 1250^\circ\text{C}$ over time. Here, $e_{g,norm}$ remains approximately constant for all three parameters up to a t_{inter} of 100 s, while values subsequently decrease and a plateau is formed for a t_{inter} of between 100 and 400 s. As already outlined for a T_a of 1100°C , the $AR_{Y/X}$ curve progression over time shows the largest decrease of $e_{g,norm}$ for a T_a of 1250°C resulting in the most pronounced plateau formation in the curves' progression.

3.2 Determination of the degree of recrystallization

Figure 5 shows the profiles for the degree of recrystallization for different annealing temperatures (1100°C and 1250°C) over time determined by the authors in [8] in double-hit compression tests' as well as the recrystallization degree after the single-hit compression tests determined from formula 5 as a function of the grain elongation parameter and f_{crit} . Figure 5a shows the curves for the recrystallization established from $AR_{Y/X}$ after a T_a of 1100°C and a variation of f_{crit} between 1.05 and 1.25. For $t_{inter} < 300$ s, a f_{crit} of 1.20 corresponds most closely to the recrystallization curve after the double-hit compression tests. For longer t_{inter} , a better agreement is obtained for $f_{crit} = 1.15$. In Figure 5b, the curve for $AR_{Y/X}$ and a f_{crit} of 1.10 shows the best agreement with the values of the double-hit compression tests after a T_a of 1250°C up to a t_{inter} of 500 s. For $t_{inter} > 500$ s, a better agreement is obtained for a f_{crit} of 1.15. After a T_a of 1250°C , the double-hit compression tests result in the formation of

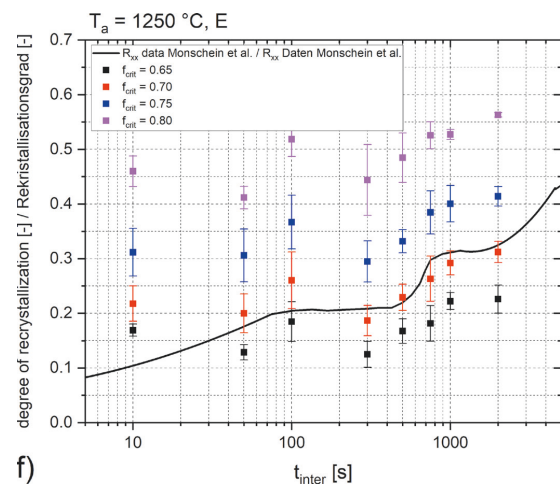
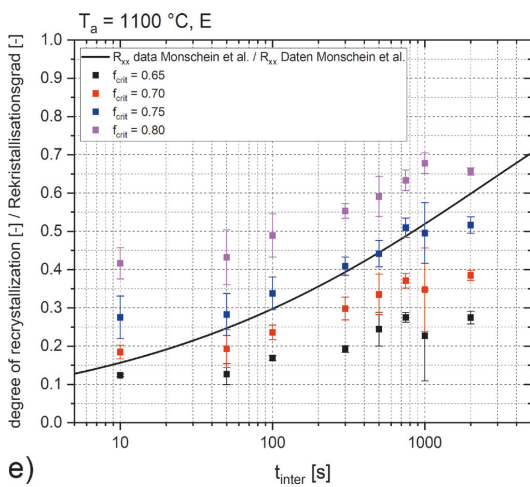
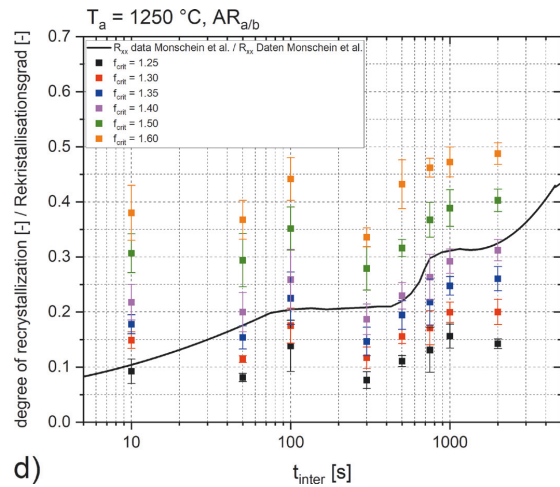
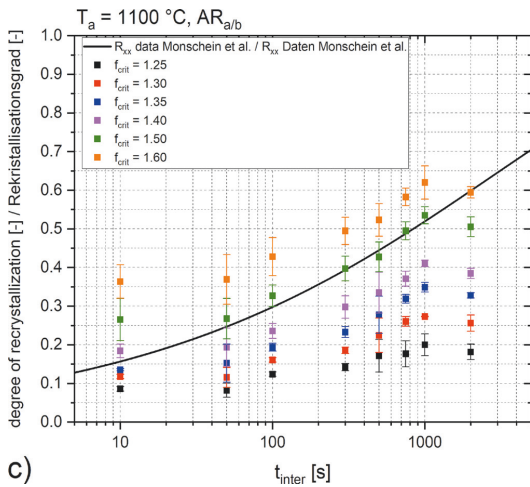
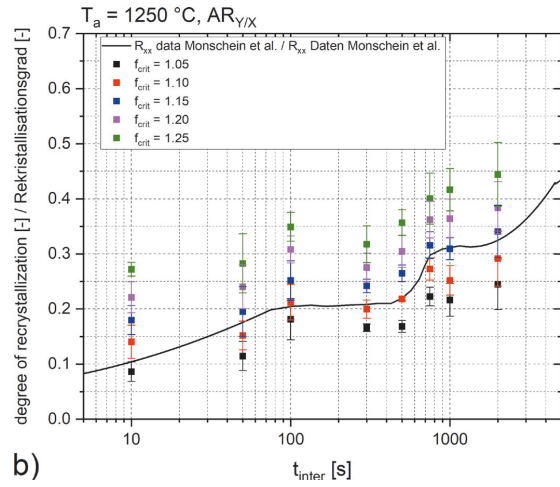
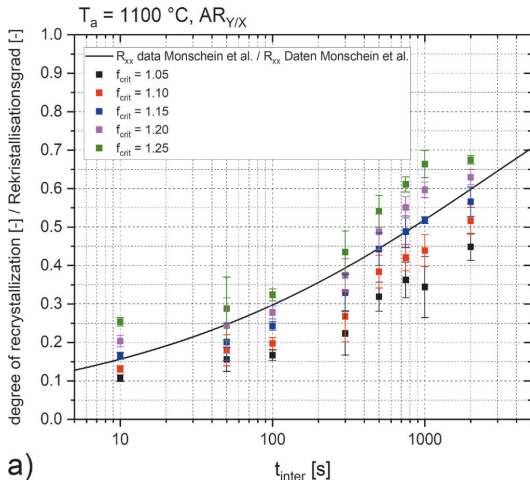
chen. Bild 4b zeigt den zeitlichen Verlauf von $e_{g,norm}$ für eine T_a von 1250°C . Hierbei zeigt sich für alle drei Parameter, dass bis zu einer t_{inter} von 100 s die $e_{g,norm}$ annähernd konstant bleibt und es anschließend zu einer Abnahme und der Ausbildung eines Plateaus zwischen t_{inter} von 100-400 s kommt. Wie bereits für eine T_a von 1100°C beschrieben, zeigt auch bei einer T_a von 1250°C der zeitliche Verlauf von $AR_{Y/X}$ die größte Verringerung von $e_{g,norm}$, was zur deutlichsten Ausprägung des Plateaus im Kurvenverlauf führt.

3.2 Ermittlung des Rekristallisationsgrads

Bild 5 zeigt die anhand von Doppelstauchversuchen von den Autoren in [8] ermittelten zeitlichen Verläufe des Rekristallisationsgrads für unterschiedliche Glühtemperaturen (1100°C und 1250°C) sowie die aus Formel 5 ermittelten Rekristallisationsgrade nach den Einzelstauchversuchen abhängig vom Kornstreckungsparameter und f_{crit} . Bild 5a zeigt die aus $AR_{Y/X}$ ermittelten Verläufe der Rekristallisation nach einer T_a von 1100°C und einer Variation von f_{crit} zwischen 1,05 und 1,25. Für $t_{inter} > 300$ s zeigt ein f_{crit} von 1,20 die größte Übereinstimmung zum Rekristallisationsverlauf nach den Doppelstauchversuchen. Für längere t_{inter} gibt es eine bessere Übereinstimmung für $f_{crit} = 1,15$. Nach einer T_a von 1250°C zeigt in Bild 5b jene Kurve von $AR_{Y/X}$ und f_{crit} von 1,10 bis zu einer t_{inter} von 500 s die beste Übereinstimmung zu den Werten der Doppelstauchversuche. Für $t_{inter} > 500$ s zeigt sich eine bessere Übereinstimmung bei einem f_{crit} von 1,15. Die Ergebnisse der Doppelstauchversuche zeigen nach einer T_a von 1250°C die Bildung

Figure 5a to f: Profile of the recrystallization over time as a function of f_{crit} for the different grain elongation parameters and different T_a as well as the profile of the recrystallization previously determined by the authors [8] in double-hit compression tests. a) $AR_{Y/X}$, $T_a = 1100^\circ\text{C}$; b) $AR_{Y/X}$, $T_a = 1250^\circ\text{C}$; c) $AR_{a/b}$, $T_a = 1100^\circ\text{C}$; d) $AR_{a/b}$, $T_a = 1250^\circ\text{C}$; e) E , $T_a = 1100^\circ\text{C}$; f) E , $T_a = 1250^\circ\text{C}$.

Bild 5a bis f: zeitlicher Verlauf der Rekristallisation abhängig von f_{crit} für die unterschiedlichen Kornstreckparameter und unterschiedliche T_a , sowie der von den Autoren [8] vorab durch Doppelstauchversuche ermittelte Verlauf der Rekristallisation. a) $AR_{Y/X}$, $T_a = 1100^\circ\text{C}$; b) $AR_{Y/X}$, $T_a = 1250^\circ\text{C}$; c) $AR_{a/b}$, $T_a = 1100^\circ\text{C}$; d) $AR_{a/b}$, $T_a = 1250^\circ\text{C}$; e) E , $T_a = 1100^\circ\text{C}$; f) E , $T_a = 1250^\circ\text{C}$.



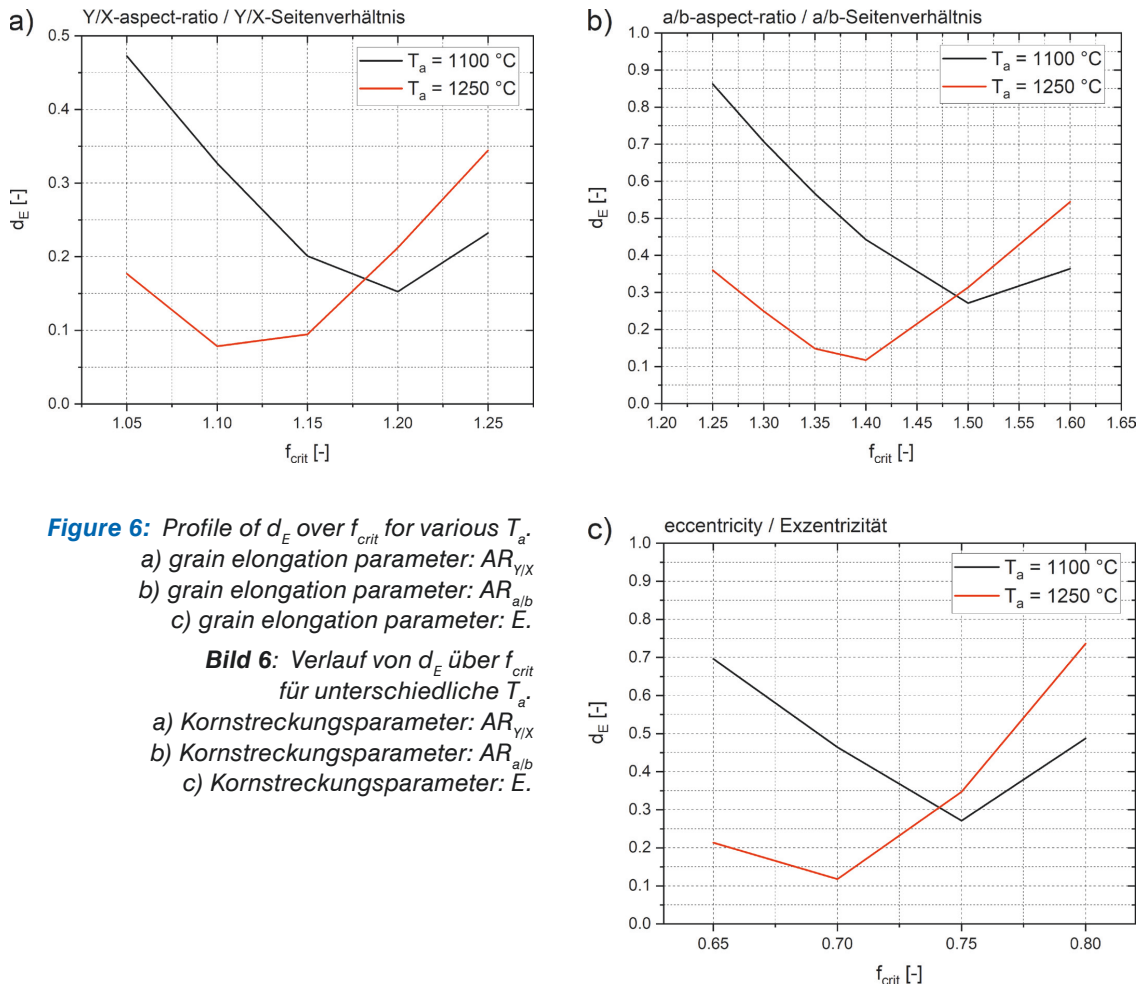


Figure 6: Profile of d_E over f_{crit} for various T_a .
 a) grain elongation parameter: $AR_{Y/X}$
 b) grain elongation parameter: $AR_{a/b}$
 c) grain elongation parameter: E .

Bild 6: Verlauf von d_E über f_{crit} für unterschiedliche T_a .
 a) Kornstreckungsparameter: $AR_{Y/X}$
 b) Kornstreckungsparameter: $AR_{a/b}$
 c) Kornstreckungsparameter: E .

a plateau for t_{inter} between 100 s and 500 s. This could be attributed to the formation of strain-induced Nb(C,N) precipitates [8]. All curves in Figure 5b show the formation of a plateau at the same position, regardless of f_{crit} . d_E was used as a measure to quantify the similarity of the recrystallization profiles as a function of f_{crit} after the double-hit compression tests [8] and single-hit compression tests (see formula 6). Figure 6a shows the progression of d_E as a function of T_a and f_{crit} , where $AR_{Y/X}$ was included as a grain elongation parameter. After a T_a of 1100 °C, the progression of d_E shows a minimum at a f_{crit} of 1.20, whereas a rise in T_a to 1250 °C leads to a further reduction of the minimum to $f_{crit} = 1.10$.

eines Plateaus für t_{inter} zwischen 100 s und 500 s, was auf die Bildung dehnungsinduzierter Nb(C,N) Ausscheidungen zurückzuführen war [8]. Unabhängig von f_{crit} zeigen alle Kurven in Bild 5b die Formation eines Plateaus an derselben Stelle. Um die Ähnlichkeit der Rekristallisationsverläufe nach den Doppelstauchversuchen [8] und Einzelstauchversuchen, abhängig von f_{crit} , zu quantifizieren, wurde d_E als Maß herangezogen (siehe Formel 6). Bild 6a zeigt den Verlauf von d_E , abhängig von T_a und f_{crit} , wobei $AR_{Y/X}$ als Kornstreckungsparameter herangezogen wurde. Nach einer T_a von 1100 °C zeigt der Verlauf von d_E ein Minimum bei einem f_{crit} von 1,20, wobei eine Erhöhung der T_a auf 1250 °C das Minimum auf $f_{crit} = 1,10$ senkt.

Figure 5c shows the recrystallization profiles for a T_a of 1100 °C determined from $AR_{a/b}$. It is found that a f_{crit} of 1.50 gives the best agreement with the recrystallization curve of the double-hit compression tests, this is further confirmed by a minimum of d_E in Figure 6b. Figure 5d shows the profiles for a T_a of 1250 °C determined from $AR_{a/b}$. Except for a t_{inter} of 10 s and 100 s, the profile for a $f_{crit} = 1.40$ gives the best agreement with the curve after the double-hit compression tests. This is also confirmed by the occurrence of a minimum at the aforementioned f_{crit} in the profile of d_E in Figure 6b.

The recrystallization curves over time in which the eccentricity of the fitted ellipse was used as a grain elongation parameter are shown in Figure 5e ($T_a = 1100$ °C) and Figure 5f ($T_a = 1250$ °C). A T_a of 1100 °C gives the best agreement for a f_{crit} of 0.75, though there are two outliers at a t_{inter} of 10 s and 2000 s. After a $T_a = 1250$ °C, the profile for a $f_{crit} = 0.70$ gives the best agreement, whereas two outliers occurred after a t_{inter} of 10 s and 100 s (here, a f_{crit} of 0.65 gives a better agreement). In Figure 6c the minima of the d_E curves can be found at a f_{crit} of 0.75 for a T_a of 1100 °C and at a f_{crit} of 0.70 for a T_a of 1250 °C. The d_E curves thus confirm the visual assessment of the profiles described above.

4 Discussion

The present work mainly aimed at determining the degree of recrystallization of a microalloyed steel by analyzing compressed samples using a light microscope. For that, single-hit compression tests were carried out with the aid of a deformation dilatometer to produce compressed samples with different degrees of recrystallization.

In previous works, for example those by Gomez et al. [17] and Fernandez et al. [19],

In Bild 5c sind die aus $AR_{a/b}$ ermittelten Verläufe der Rekristallisation für eine T_a von 1100 °C abgebildet. Es zeigt sich, dass ein f_{crit} von 1,50 die größte Übereinstimmung mit dem Rekristallisationsverlauf der Doppelstauchversuche liefert, was ebenfalls durch ein Minimum von d_E in Bild 6b bestätigt wird. Bild 5d zeigt die aus $AR_{a/b}$ ermittelten Verläufe für eine T_a von 1250 °C. Bis auf eine t_{inter} von 10 s und 100 s zeigt der Verlauf bei einem $f_{crit} = 1,40$ die beste Übereinstimmung mit dem Verlauf nach den Doppelstauchversuchen. Dies bestätigt auch der Verlauf von d_E in Bild 6b durch das Auftreten eines Minimums bei besagtem f_{crit} .

Die zeitlichen Verläufe der Rekristallisation, in denen die Exzentrizität der gefitteten Ellipse als Kornstreckungsparameter herangezogen wurde, sind in Bild 5e ($T_a = 1100$ °C) und Bild 5f ($T_a = 1250$ °C) abgebildet. Bei einer T_a von 1100 °C gibt es die beste Übereinstimmung für ein f_{crit} von 0,75, wobei es zwei Ausreißer bei einer t_{inter} von 10 s und 2000 s gibt. Nach einer $T_a = 1250$ °C zeigt jene Kurve mit einem $f_{crit} = 0,70$ die beste Übereinstimmung mit zwei Ausreißern nach einer t_{inter} von 10 s und 100 s (Hier liefert ein f_{crit} von 0,65 eine bessere Übereinstimmung.). Die Minima in den d_E -Verläufen in Bild 6c befinden sich bei einer T_a von 1100 °C bei einem f_{crit} von 0,75 und bei einer T_a von 1250 °C bei einem f_{crit} von 0,70. Die d_E -Verläufe bestätigen demnach die weiter oben beschriebene optische Begutachtung der Kurvenverläufe.

4 Diskussion

Das Hauptziel der vorliegenden Arbeit war es, den Rekristallisationsgrad eines mikrolegierten Stahls durch eine lichtmikroskopische Analyse von gestauchten Proben zu ermitteln. Hierfür wurden Einzelstauchversuche mit einem Umformdilatometer durchgeführt, um gestauchte Proben mit unterschiedlichen Rekristallisationsgraden zu erzeugen.

In vergangenen Arbeiten, beispielsweise von Gomez et al. [17] und Fernandez et al. [19],

a line intercept method was used to analyze the degree of recrystallization of microalloyed steels. In both works, the degree of recrystallization was calculated from the ratio of line intersections of recrystallized grains to the number of intersections of all grains. However, both works do not provide any detailed information on which grains were considered recrystallized and which were not. *Chen et al.* [20] investigated the recrystallization behavior of an aluminum alloy. However, they chose another approach. In their work, they arbitrarily chose a threshold value of the $AR_{Y/X}$ of 1.75 as a criterion to decide whether a grain was recrystallized or not. Again, the grounds for choosing this threshold value were not specified. The degree of recrystallization was subsequently calculated from the ratio of the surface area of recrystallized grains and the total surface area of all grains.

A similar approach was chosen in the present work to determine the degree of recrystallization of a microalloyed steel. Three parameters were defined in a first step to describe the grain elongation, namely $AR_{Y/X}$, $AR_{a/b}$, and E , where $AR_{Y/X}$ is the Y/X aspect-ratio of the elongated grain. In this context, it must be made sure that the LOM image is oriented in such a way that the samples' compression plane runs parallel to the image axis. However, using $AR_{Y/X}$ has the advantage over using $AR_{a/b}$ and E in that the ellipses do not have to be fitted into each and every grain. Thus, the grain shape directly provides information on the grain elongation.

In the next step, the profile of the grain elongation over time was normalized and the results were plotted (see Figure 4) in order to compare the curves. The same tendency can be observed for all profiles. However, it can also be observed that the $AR_{Y/X}$ curves show the largest temporal decrease after a

wurde ein Linienschnittverfahren angewendet, um den Rekristallisationsgrad mikrolegierter Stähle zu untersuchen. Der Rekristallisationsgrad errechnete sich in beiden Arbeiten aus dem Verhältnis der Linienschnittpunkte rekristallisierter Körner zur Anzahl der Schnittpunkte aller Körner. Jedoch wurde in beiden zitierten Arbeiten nicht näher erläutert, welche Körner als rekristallisiert angenommen wurden und welche nicht. *Chen et al.* [20] untersuchten das Rekristallisationsverhalten einer Aluminium-Legierung und wählten einen anderen Ansatz. In deren Arbeit diente ein willkürlich gewählter Grenzwert des $AR_{Y/X}$ von 1,75 als Kriterium, um zu entscheiden, ob es sich um ein rekristallisiertes oder nicht rekristallisiertes Korn handelte. Auch hier wurde nicht näher erläutert, weshalb gerade dieser Grenzwert für die Entscheidung herangezogen wurde. Der Rekristallisationsgrad errechnete sich anschließend aus dem Verhältnis der Fläche der rekristallisierten Körner zur Gesamtfläche aller Körner.

In der vorliegenden Arbeit wurde für die Bestimmung des Rekristallisationsgrads eines mikrolegierten Stahls ein ähnlicher Ansatz gewählt. Im ersten Schritt wurden drei Parameter definiert, um die Kornstreckung zu beschreiben, nämlich das $AR_{Y/X}$, das $AR_{a/b}$ und die E . Beim $AR_{Y/X}$ handelt es sich um das Y/X-Seitenverhältnis des gestreckten Korns. Hierbei muss darauf geachtet werden, die LOM-Aufnahme so auszurichten, dass die Stauchebeine der Proben parallel zur Bildachse ist. Die Verwendung des $AR_{Y/X}$ hat jedoch gegenüber dem $AR_{a/b}$ und der E den Vorteil, dass keine Ellipse virtuell in jedes Korn gefittet werden muss und somit die Kornform direkt eine Auskunft über die Kornstreckung liefert.

Im nächsten Schritt wurden die zeitlichen Verläufe der Kornstreckung normiert und die Ergebnisse geplottet (siehe Bild 4), um die Verläufe untereinander zu vergleichen. Hier zeigt sich einerseits, dass alle Verläufe den selben Trend haben. Es zeigt sich aber auch andererseits, dass sowohl nach einer T_a von 1100 °C,

T_a of 1100 °C and a T_a of 1250 °C. The results of these analyses thus suggest that the $AR_{\gamma/\chi}$ provides the highest sensitivity with regard to changes in the grain elongation. The time-dependent degree of recrystallization of the examined steels was already previously determined by the authors in double-hit compression tests. The results were published in [8]. In that work, the authors could show that a plateau formed in the recrystallization curves after a T_a of 1250 °C and between a t_{inter} of 100 s to 500 s. This can be attributed to the formation of strain-induced Nb(C,N)-precipitates. Other authors could also observe this effect in works investigating the recrystallization behavior of microalloyed steels [12–15]. The profile of $e_{g,norm}$ in Figure 4b shows the formation of a plateau at the same position. Hence, the presented methodology is also suitable to indicate the formation of strain-induced microalloying precipitates.

In order to extrapolate the degree of recrystallization from the grain elongation, a grain elongation threshold value (f_{crit}) was taken as a criterion to define if a grain is considered as recrystallized or non-recrystallized. Figure 5 shows the determined recrystallization profiles for the different grain elongation parameters, as well as for the two varying annealing temperatures of 1100 °C and 1250 °C. Not only the recrystallization curves determined from the single-hit compression tests were plotted but also those based on the double-hit compression tests published by the authors in [8]. In a comparison of the curves after a T_a of 1100 °C and those after a T_a of 1250 °C, those representing the values after a higher annealing temperature are characterized by a slower recrystallization. As has already been stated above, this can be attributed to the formation of strain-induced Nb(C,N)-precipitates after a $T_a = 1250$ °C. In addition to that, an increase in the austenite grain size can be observed

als auch nach einer T_a von 1250 °C die Verläufe des $AR_{\gamma/\chi}$ die größte zeitliche Abnahme aufweisen. Die Ergebnisse dieser Untersuchungen legen daher nahe, dass das $AR_{\gamma/\chi}$ die größte Sensitivität im Hinblick auf Veränderungen der Kornstreckung liefert. Der zeitabhängige Rekristallisationsgrad des untersuchten Stahls wurde von den Autoren bereits vorab durch Doppelstauchversuche bestimmt und die Ergebnisse in [8] publiziert. Die Autoren konnten dort zeigen, dass es nach einer T_a von 1250 °C sowie zwischen einer t_{inter} von 100 s bis 500 s zur Ausbildung eines Plateaus in den Rekristallisationskurven kam. Verantwortlich hierfür war die Bildung dehnungsinduzierter Nb(C,N)-Ausscheidungen. Diesen Effekt konnten auch andere Autoren bei der Untersuchung des Rekristallisationsverhaltens mikrolegierter Stähle beobachten [12–15]. Der $e_{g,norm}$ -Verlauf in Bild 4 b) zeigt die Ausbildung eines Plateaus an derselben Stelle, weswegen sich diese Methodik ebenfalls eignet, um die Bildung dehnungsinduzierter Mikrolegierungsausscheidungen anzuzeigen.

Um von der Kornstreckung auf den Rekristallisationsgrad schließen zu können, wurde ein Grenzwert der Kornstreckung (f_{crit}) als Kriterium herangezogen, unter welchem ein Korn als rekristallisiert, beziehungsweise über welchem ein Korn als nicht rekristallisiert gilt. Bild 5 zeigt die dadurch ermittelten Rekristallisationsverläufe für die unterschiedlichen Kornstreckungsparameter sowie die zwei variierenden Glühtemperaturen von 1100 °C und 1250 °C. Neben den aus den Einzelstauchversuchen ermittelten Rekristallisationsverläufen sind ebenfalls die von den Autoren in [8] veröffentlichten Verläufe der Doppelstauchversuche geplottet. Vergleicht man die Kurven nach einer T_a von 1100 °C mit jenen von 1250 °C zeigen die Verläufe nach einer höheren Glühtemperatur eine verlangsamte Rekristallisation. Dies liegt, wie bereits weiter oben beschrieben, an der Formation dehnungsinduzierter Nb(C,N)-Ausscheidungen nach einer $T_a = 1250$ °C. Des Weiteren kommt es nach einer Erhöhung der T_a von 1100 °C auf 1250 °C

during annealing after the rise of T_a from 1100 °C to 1250 °C, which has a decelerating effect on the recrystallization owing to the lower number of nucleation sites.

The similarity of the recrystallization curves of the single-hit and the double-hit compression tests was quantified based on d_E . The curves for d_E plotted over f_{crit} shown in Figure 6 confirm the optically determined agreements of the profiles in Figure 5. The Euclidean distance is a single value. It thus does not allow any statement on the occurrence of curve outliers. Taking a closer look at the curve profiles, some isolated deviations of the degrees of recrystallization in the single-hit compression tests and the profiles of the double-hit compression tests can be observed. For $AR_{a/b}$ after a T_a of 1100 °C (Figure 5c), this is evidenced by a dropping degree of recrystallization between a t_{inter} of 1000 s and 2000 s. After a T_a of 1250 °C (Figure 5d), the degrees of recrystallization of the single-hit compression tests after a t_{inter} of 10 s and 100 s show higher values than the profiles after the double-hit compression tests. The same tendency can be observed in Figure 5e and Figure 5f where the eccentricity is used as a measure for the grain elongation. The smallest deviations between the profiles of the single-hit and the double-hit compression tests can be observed for the curves in which $AR_{y/x}$ is taken as a grain elongation parameter. See Figures 5a and 5b. The results of this work demonstrate that, owing also to its increased sensitivity regarding changes in the grain elongation, using $AR_{y/x}$ as a parameter for the grain elongation is best suited to analyze the degree of recrystallization of microalloyed steels. Figure 5a, Figure 5b, and Figure 6 thus show that a f_{crit} of 1.20 after a T_a of 1100 °C and a f_{crit} of 1.10 after a T_a of 1250 °C provide the best results when $AR_{y/x}$ was used as a grain elongation parameter. In concrete terms, this means that grains whose ratio grain length to grain width fall

während der Glühung zu einer Erhöhung der Austenitkorngröße, was in weiterer Folge auf Grund der geringeren Anzahl an Keimstellen ebenfalls einen rekristallisationsverzögernden Effekt verursacht.

Die Ähnlichkeit der Verläufe der Rekristallisationskurven der Einzelstauch- und Doppelstauchversuche wurde mit Hilfe dem d_E quantifiziert. Die in Bild 6 abgebildeten Verläufe des d_E über dem f_{crit} bestätigen die optischen Übereinstimmungen der Kurven in Bild 5. Bei dem euklidischen Abstand handelt es sich um einen Einzelwert, welcher demnach keine Aussage über das Auftreten von Ausreißern zwischen den Kurvenverläufen liefert. Bei genauer Betrachtung der Kurvenverläufe zeigen sich jedoch teilweise punktuelle Abweichungen der Rekristallisationsgrade der Einzelstauchversuche und den Verläufen der Doppelstauchversuche. Dies zeigt sich für das $AR_{a/b}$ nach einer T_a von 1100 °C (Bild 5c) in einer Abnahme des Rekristallisationsgrads zwischen einer t_{inter} von 1000 s und 2000 s. Nach einer T_a von 1250 °C (Bild 5d) liefern die Rekristallisationsgrade der Einzelstauchversuche nach einer t_{inter} von 10 s sowie 100 s höhere Werte als die Verläufe nach den Doppelstauchversuchen. Der gleiche Trend ist zu beobachten, wenn die Exzentrizität als Maß für die Kornstreckung herangezogen wird, was sich in Bild 5e und Bild 5f zeigt. Die geringsten Abweichungen zwischen den Verläufen der Einzelstauch- und Doppelstauchversuche zeigen jene Kurven, in denen $AR_{y/x}$ als Kornstreckungsparameter verwendet wurde, was in Bild 5a und Bild 5b ersichtlich wird. In Kombination mit der erhöhten Sensitivität, welches das $AR_{y/x}$ im Hinblick auf Veränderungen der Kornstreckung zeigt, zeigen die Ergebnisse dieser Arbeit, dass sich die Verwendung des $AR_{y/x}$ als Parameter der Kornstreckung am besten eignet um den Rekristallisationsgrad mikrolegierter Stähle zu untersuchen. Bild 5a, Bild 5b und Bild 6 zeigen demnach, dass in den Verläufen in denen $AR_{y/x}$ als Kornstreckungsparameter verwendet wurde, nach einer T_a von 1100 °C ein $f_{crit} = 1,20$ und nach einer T_a von

below 1.10 or 1.20, respectively, are considered as recrystallized.

In this work, it could be shown that f_{crit} is a function of the grain elongation parameter and that it is also slightly dependent of the deformation parameters. However, once f_{crit} is determined for a deformation process, the method presented here allows an automated analysis of the degree of recrystallization in microalloyed steels using the light microscope.

5 Summary

This work aimed at directly determining the degree of recrystallization of compressed samples of a microalloyed HSLA steel in the light microscope. For this purpose, single-hit compression tests were performed with varying test parameters using a deformation dilatometer to produce samples with various degrees of recrystallization. The time-dependent degree of recrystallization of the examined steels was already previously determined by the authors in double-hit compression tests. Based on the respective results, the evaluation parameters for the direct light microscope analysis of the degree of recrystallization could be adjusted in order to obtain the best possible agreement between the recrystallization curves of the single-hit and the double-hit compression tests. A critical grain elongation threshold value (f_{crit}) was taken as a measure to decide whether the respective grains were recrystallized or not. Three parameters were chosen to describe the grain elongation, namely the Y/X aspect-ratio ($AR_{Y/X}$), the a/b aspect-ratio ($AR_{a/b}$), and the eccentricity (E). The results of this work can be summarized as follows:

- After an annealing temperature (T_a) of 1100 °C, the curves for the normalized

1250 °C ein $f_{crit} = 1,10$ die besten Resultate liefert. Konkret bedeutet dies, dass in besagtem Fall Körner als rekristallisiert gelten, in denen das Kornlänge-zu-Kornbreite-Verhältnis unter 1,10, beziehungsweise 1,20 liegt.

Bezüglich f_{crit} konnte in dieser Arbeit gezeigt werden, dass dieser Wert abhängig ist vom Kornstreckungsparameter sowie ebenfalls geringfügig von den Umformparametern. Wird f_{crit} für einen Umformprozess jedoch einmal bestimmt, ermöglicht die hier gezeigte Methode eine automatisierte lichtmikroskopische Analyse des Rekristallisationsgrads mikrolegierter Stähle.

5 Zusammenfassung

Diese Arbeit hatte das Ziel, den Rekristallisationsgrad von gestauchten Proben eines mikrolegierten HSLA-Stahls direkt lichtmikroskopisch zu ermitteln. Hierfür wurden mittels eines Umformdilatometers Einzelstauchversuche mit variierenden Versuchsparametern durchgeführt, um Proben mit unterschiedlichem Rekristallisationsgrad zu erzeugen. Der zeitabhängige Rekristallisationsgrad des untersuchten Stahls wurde von den Autoren bereits vorab durch Doppelstauchversuche bestimmt [8]. Anhand dieser Ergebnisse war es möglich, die Auswerteparameter für die direkte lichtmikroskopische Analyse des Rekristallisationsgrads anzupassen, um eine bestmögliche Übereinstimmung zwischen den Rekristallisationsverläufen der Einzelstauch- und Doppelstauchversuche zu erhalten. Ein kritischer Grenzwert der Kornstreckung (f_{crit}) wurde als Maß herangezogen, um zu entscheiden, ob es sich bei den jeweiligen Körnern um rekristallisierte oder nicht rekristallisierte Körner handelt. Um die Kornstreckung zu beschreiben wurden drei Parameter ausgewählt, nämlich das Y/X-Seitenverhältnis ($AR_{Y/X}$), das a/b-Seitenverhältnis ($AR_{a/b}$) und die Exzentrizität (E). Die Ergebnisse der Arbeit lassen sich wie folgt zusammenfassen:

- Nach einer Glühtemperatur (T_a) von 1100 °C zeigen die Verläufe der normierten Korn-

grain elongation ($e_{g,norm}$) for all three grain elongation parameters are characterized by a temporal decrease. The most pronounced decrease can be observed for the $AR_{Y/X}$ curve, followed by $AR_{a/b}$, and E. After a $T_a = 1250^\circ\text{C}$, the profile of $e_{g,norm}$ over time shows a constant progression for all grain elongation parameters up to a holding time (t_{inter}) of 100 s. A plateau is subsequently formed between a t_{inter} of 100 s to 400 s. For this annealing temperature, the profile of $AR_{Y/X}$ over time also shows the strongest decrease of $e_{g,norm}$ as well as the most pronounced plateau.

- The double-hit compression tests previously performed [8] indicated that strain-induced Nb(C,N) precipitates formed after a $T_a = 1250^\circ\text{C}$ and a t_{inter} of 100 s. This is evidenced by the formation of a plateau in the recrystallization diagram. With regard to the profile of $e_{g,norm}$ after a T_a of 1250°C and a t_{inter} of 100 s, all three grain elongation parameters are characterized by the same trend. The profile of $e_{g,norm}$ over time is therefore also suited to show the beginning of the formation of strain-induced precipitates. The most pronounced plateau is formed for $AR_{Y/X}$, followed by $AR_{a/b}$ and E.
- After a T_a of 1100°C , the recrystallization profiles for which $AR_{Y/X}$ is chosen as a grain elongation parameter show that the best agreement of the recrystallization profiles between the double-hit and the single-hit compression tests is obtained for a f_{crit} of 1.20 up to a t_{inter} of 300 s. For $t_{inter} > 300$ s, a f_{crit} of 1.15 shows the best agreement. The Euclidean distance (d_E), taken as a measure to quantify the similarity of the curves, shows the best agreement of the recrystallization profiles for a f_{crit} of 1.20. The curves determined from $AR_{a/b}$ as well as d_E show that the greatest similarity for the recrystallization profiles is obtained for $f_{crit} = 1.50$. For the recrystallization profiles in which E is used as a grain elongation parameter, the best

streckung ($e_{g,norm}$) für alle drei Kornstreckungsparameter eine zeitliche Abnahme. Die stärkste Abnahme zeigt die Kurve des $AR_{Y/X}$, gefolgt vom $AR_{a/b}$ und der E. Nach einer $T_a = 1250^\circ\text{C}$ zeigt der zeitliche Verlauf der $e_{g,norm}$ für alle Kornstreckungsparameter bis zu einer Haltezeit (t_{inter}) von 100 s einen konstanten Verlauf, wobei es im Anschluss zur Ausbildung eines Plateaus zwischen einer t_{inter} von 100 s bis 400 s kommt. Der zeitliche Verlauf der $AR_{Y/X}$ -Kurve zeigt auch bei dieser Glüh Temperatur die stärkste zeitliche Abnahme von $e_{g,norm}$ sowie die deutlichste Ausprägung des Plateaus.

- Die vorab durchgeführten Doppelstauchversuche [8] zeigten, dass es nach einer $T_a = 1250^\circ\text{C}$ und einer t_{inter} von 100 s zur Bildung dehnungsinduzierter Nb(C,N)-Ausscheidungen kam. Dies zeigte sich durch die Ausbildung eines Plateaus im Rekristallisationsdiagramm. Alle drei Kornstreckungsparameter weisen für den Verlauf der $e_{g,norm}$ denselben Trend nach einer T_a von 1250°C und einer t_{inter} von 100 s auf, weswegen sich der zeitliche Verlauf der $e_{g,norm}$ ebenfalls eignet, um den Beginn der Formation dehnungsinduzierter Ausscheidungen anzuzeigen. Am deutlichsten ausgeprägt ist die Plateaubildung für das $AR_{Y/X}$, gefolgt von dem $AR_{a/b}$ und der E.
- Nach einer T_a von 1100°C zeigen die Rekristallisationsverläufe, in denen das $AR_{Y/X}$ als Kornstreckungsparameter gewählt wurde, dass es bei einem f_{crit} von 1,20 bis zu einer t_{inter} von 300 s die beste Übereinstimmung der Rekristallisationsverläufe zwischen den Doppelstauch- und den Einzelstauchversuchen gibt. Für $t_{inter} > 300$ s zeigt ein f_{crit} von 1,15 die beste Übereinstimmung. Die euklidische Distanz (d_E), welche als Maß herangezogen wurde, um die Ähnlichkeit der Kurven zu quantifizieren, zeigt bei einem f_{crit} von 1,20 die größte Übereinstimmung der Rekristallisationsverläufe. Die aus den $AR_{a/b}$ ermittelten Verläufe, sowie die d_E , zeigen, dass bei einem $f_{crit} = 1,50$ die größte Ähnlichkeit für die Rekristallisationsverläufe besteht. Für die Verläufe der Rekristallisation,

agreement is obtained after a $f_{crit} = 0.75$, though two outliers occur after a t_{inter} of 10 s and 2000 s. d_E likewise has a minimum at $f_{crit} = 0.75$, indicating the best curve agreement.

- After a T_a of 1250 °C, the recrystallization profiles for which $AR_{Y/X}$ was taken as a grain elongation parameter show that the best agreement is obtained for a f_{crit} of 1.10 up to a t_{inter} of 500 s. A f_{crit} of 1.15 provides the best agreement for $t_{inter} > 500$ s, whereas d_E shows the best agreement of the recrystallization profiles for a f_{crit} of 1.10. d_E , as well as the profiles determined from the $AR_{a/b}$, show that, apart from two outliers after a t_{inter} of 10 s and 100 s, the best agreement of the recrystallization profiles is obtained for a $f_{crit} = 1.40$. For the recrystallization profiles in which E is used as a grain elongation parameter, the best curve agreement is obtained after a $f_{crit} = 0.70$, though two outliers occur after a t_{inter} of 10 s and 100 s. d_E also has a minimum for $f_{crit} = 0.70$, indicating the best agreement of the curves.
 - After a T_a of 1250 °C, recrystallization profiles over time are characterized by the formation of a plateau for a t_{inter} of between 100 s to 400 s for all three grain elongation parameters. Hence, a light microscope analysis of the grain elongation is suited for indicating the recrystallization inhibiting properties of strain-induced microalloying precipitates.
 - Taking the $AR_{Y/X}$ as a grain elongation parameter is best suited for the determination of the degree of recrystallization in the light microscope. No ellipse must be fitted into each and every grain so that the grain shape itself provides information on the grain elongation. Furthermore, the
- in denen E als Kornstreckungsparameter herangezogen wurde, zeigt sich die beste Übereinstimmung in den Kurvenverläufen nach einem $f_{crit} = 0,75$, wobei es zwei Ausreißer nach einer t_{inter} von 10 s und 2000 s gibt. Auch der d_E weist bei einem $f_{crit} = 0,75$ ein Minimum auf, was die beste Übereinstimmung der Kurven anzeigt.
 - Nach einer T_a von 1250 °C zeigen die Rekristallisationsverläufe, in denen das $AR_{Y/X}$ als Kornstreckungsparameter gewählt wurde, dass es bei einem f_{crit} von 1,10 bis zu einer t_{inter} von 500 s die beste Übereinstimmung der Rekristallisationsverläufe gibt. Für $t_{inter} > 500$ s zeigt ein f_{crit} von 1,15 die beste Übereinstimmung. d_E zeigt bei einem f_{crit} von 1,10 die größte Übereinstimmung der Rekristallisationsverläufe. Die d_E sowie die aus dem $AR_{a/b}$ ermittelten Verläufe zeigen, dass es bis auf zwei Ausreißer nach einer t_{inter} von 10 s und 100 s, die beste Übereinstimmung der Rekristallisationsverläufe bei einem $f_{crit} = 1,40$ gibt. Für die Rekristallisationsverläufe, in denen E als Kornstreckungsparameter herangezogen wurde, zeigt sich die beste Übereinstimmung in den Kurvenverläufen nach einem $f_{crit} = 0,70$, wobei es zwei Ausreißer nach einer t_{inter} von 10 s und 100 s gibt. Auch die d_E weist bei einem $f_{crit} = 0,70$ ein Minimum auf, was die beste Übereinstimmung der Kurven anzeigt.
 - Nach einer $T_a = 1250$ °C weisen die zeitlichen Rekristallisationsverläufe für alle drei Kornstreckungsparameter das Ausbilden eines Plateaus zwischen einer t_{inter} von 100 bis 400 s auf. Durch eine lichtmikroskopische Analyse der Kornstreckung ist es daher möglich, die rekristallisationshemmenden Eigenschaften von dehnungsinduzierten Mikrolegierungsausscheidungen zu zeigen.
 - Die Verwendung des $AR_{Y/X}$ als Kornstreckungsparameter eignet sich am besten für die lichtmikroskopische Ermittlung des Rekristallisationsgrads. Einerseits muss keine Ellipse in jedes einzelne Korn gefittet werden, wodurch bereits die Kornform selbst eine Aussage über die Kornstre-

$AR_{y/x}$ is characterized by the highest sensitivity regarding changes in the grain elongation and presents the lowest number of outliers among the recrystallization profiles.

- The results of this work show that f_{crit} is a function of the deformation parameters and the grain elongation parameters. However, once f_{crit} is determined for a deformation process, this methodology allows an automated evaluation of the degree of recrystallization in the light microscope.

ckung liefert. Andererseits weist das $AR_{y/x}$ die größte Sensitivität im Hinblick auf Veränderungen der Kornstreckung auf und liefert die geringste Zahl an Ausreißern in den Rekristallisationsverläufen.

- Die Ergebnisse dieser Arbeit zeigen, dass f_{crit} abhängig ist von den Umformparametern und dem Kornstreckungsparameter. Wurde f_{crit} für einen Umformprozess jedoch einmal bestimmt, ermöglicht diese Methodik eine automatisierte lichtmikroskopische Auswertung des Rekristallisationsgrads.

6 Acknowledgement

This work was supported by: the Austrian Federal Ministry of Climate Action and Energy, BMK, (846933) under the program “Produktion der Zukunft” (Production for the Future) of the “BMK Stiftungsprofessur für Industrie” (BMK Endowed Professorship for Industry); Austrian Research Promotion Agency GmbH (FFG:885187); Austrian Research Promotion Agency GmbH (FFG:873200).

6 Danksagung

Diese Arbeit wurde unterstützt durch: Österreichisches BMK (846933) im Rahmen des Programms “Produktion der Zukunft” der “BMK Stiftungsprofessur für Industrie”; Österreichische Forschungsförderungs GmbH (FFG:885187); Österreichische Forschungsförderungs GmbH (FFG:873200).

References / Literatur

- [1] Baker, T. N.: Ironmaking & Steelmaking 43 (2016) 4, pp. 264–307.
DOI: 10.1179/1743281215Y.0000000063
- [2] Vervynckt, S.; Verbeken, K.; Lopez, B.; Jonas, J. J.: International Materials Reviews 57 (2012) 4, pp. 187–207.
DOI: 10.1179/1743280411Y.0000000013
- [3] DeArdo, A. J.: International Materials Reviews 48 (2003) 6, pp. 371–402.
DOI: 10.1179/095066003225008833
- [4] Cahn, J. W.: Acta Metallurgica 10 (1962) 9, pp. 789–798.
DOI: 10.1016/0001-6160(62)90092-5
- [5] Dutta, B.; Sellars, C. M.: Materials Science and Technology 3 (1987) 3, pp. 197–206.
DOI: 10.1179/mst.1987.3.3.197
- [6] Baker, T. N.: Ironmaking & Steelmaking 46 (2019) 1, pp. 1–55.
DOI: 10.1080/03019233.2018.1446496
- [7] Hong, S. G.; Kang, K. B.; Park, C. G.: Scripta Materialia 46 (2002), pp. 163–168.
DOI: 10.1016/S1359-6462(01)01214-3
- [8] Monschein, S.; Kapp, M.; Zügner, D.; Fasching, J.; Landefeld, A.; Schnitzer, R.: steel research int. 92 (2021) 9, p. 2100065
DOI: 10.1002/srin.202100065
- [9] Hegetschweiler, A.; Borovinskaya, O.; Staudt, T.; Kraus, T.: Analytical chemistry 91 (2019) 1, pp. 943–950.
DOI: 10.1021/acs.analchem.8b04012
- [10] Webel, J.; Herges, A.; Britz, D.; Detemple, E.; Flaxa, V.; Mohrbacher, H.; Mücklich, F.: Metals 10

- (2020) 2, p. 243.
DOI: 10.3390/met10020243
- [11] Homsher, C. N.: Determination of the non-recrystallization temperature (TNR) in multiple microalloyed steels, 2013.
- [12] Esterl, R.; Sonnleitner, M.; Schnitzer, R.: Steel Research International 90 (2019) 3, 1800500.
- [13] Medina, S. F.; Mancilla, J. E.: ISIJ International 33 (1993) 12, pp. 1257–1264.
DOI: 10.2355/isijinternational.33.1257
- [14] Medina, S. F.; Mancilla, J. E.: Acta Metallurgica et Materialia 42 (1994) 12, pp. 3945–3951.
DOI: 10.1016/0956-7151(94)90172-4
- [15] Medina, S. F.; Mancilla, J. E.: ISIJ Int. 36 (1996) 8, pp. 1063–1069.
DOI: 10.2355/isijinternational.36.1063
- [16] Rossi, P. L. O.; Sellars, C. M.: Acta Materialia 45 (1997) 1, pp. 137–148.
DOI: 10.1016/S1359-6454(96)00167-X
- [17] Gómez, M.; Rancel, L.; Fernández, B. J.; Medina, S. F.: Materials Science and Engineering: A 501 (2009) 1-2, 188–196.
DOI: 10.1016/j.msea.2008.09.074
- [18] Perttula, J. S.; Karjalainen, L. P.: Materials Science and Technology 14 (1998) 7, 626–630.
DOI: 10.1179/mst.1998.14.7.626
- [19] Fernandez A. I.; Lopez, B.; Rodriguez-Ibabe, J. M.: Scripta Materialia Vol. 40 (1999) 5, pp. 543–549.
DOI: 10.1016/S1359-6462(98)00452-7
- [20] Chen, S. P.; Hanlon, D. N.; van der Zwaag, S.; Pei, Y. T.; Dehossion, J. T. M.: J Mater Sci 37 (2002) 5, pp. 989–995.
DOI: 10.1023/A:1014356116058
- [21] Malta, P. O.; Alves, D. S.; Ferreira, A. O. V.; Moutinho, I. D.; Dias, C. A. P.; Santos, D. B.: Metall and Mat Trans A 48 (2017) 3, pp. 1288–1309.
DOI: 10.1007/s11661-016-3935-3
- [22] Black, M. P.; Higginson, R. L.: Scripta Materialia 41 (1999) 2, pp. 125–129.
DOI: 10.1016/s1359-6462(99)00051-2
- [23] Béchet, S.; Beaujard, L.: Rev. Met. Paris 52 (1955) 10, pp. 830–836.
DOI: 10.1051/metal/195552100830
- [24] Esterl, R.; Sonnleitner, M.; Stadler, M.; Wölger, G.; Schnitzer, R.: Practical Metallography 55 (2018) 4, pp. 203–222.
DOI: 10.3139/147.110491

Bibliography

DOI 10.1515/pm-2022-1007
Pract. Metallogr. 59 (2022) 6; page 317–339
© 2022 Walter de Gruyter GmbH,
Berlin/Boston, Germany
ISSN 0032–678X · e-ISSN 2195–8599

Stefan Monschein



was born 1992 in Bruck an der Mur (Austria) and studied materials science at the Montanuniversität Leoben (Austria). He is now working on his PhD thesis about the improvement of the properties of high performance wire products.

Nikolaus Kostwein



was born 1996 in Klagenfurt (Austria) and studies materials science at the Montanuniversität Leoben (Austria). He is currently working on his master's thesis dealing with the solubility and precipitation of Niobium in thermomechanically processed steel plates.

Paper II

Stefan Monschein, Marlene Kapp, Dominik Zügner, Josef Fasching,
Andreas Landefeld and Ronald Schnitzer

*Influence of Microalloying Elements and Deformation Parameters on
the Recrystallization and Precipitation Behavior of Two Low-Alloyed
Steels*

steel research international 2021, 2100065;

DOI: 10.1002/srin.202100065

Influence of Microalloying Elements and Deformation Parameters on the Recrystallization and Precipitation Behavior of Two Low-Alloyed Steels

Stefan Monschein,* Marlene Kapp, Dominik Zügner, Josef Fasching, Andreas Landefeld, and Ronald Schnitzer

The alloy design of modern high-strength low-alloy (HSLA) steels aims for a well-balanced combination of high toughness and strength. Using niobium and titanium as microalloying elements together with thermomechanical processing is a common way to obtain a fine-grained microstructure and therefore enhance the strength and toughness of HSLA steels. Herein, a low-alloyed steel and a microalloyed HSLA steel are investigated in the as-rolled condition and by double-hit experiments using various deformation parameters. Atom probe tomography, scanning transmission electron microscopy inside a scanning electron microscope, transmission kikuchi diffraction, and energy-dispersive X-ray spectroscopy are used to investigate the precipitates in the as-rolled condition and after deformation. It is shown that Nb-enriched TiN precipitates with an average size of around 15 nm are responsible for grain refinement in the as-rolled condition. The annealing temperature prior to the rolling process is set below the solution temperature of Nb(C,N). Enhancing the annealing temperature in the double-hit deformation tests above the solution temperature of Nb(C,N) leads to the precipitation of fine NbC precipitates with a size of around 5 nm. These precipitates are responsible for inhibited static recrystallization behavior.

processing of choice to obtain a fine-grained microstructure for industrially relevant applications.^[1,2] Adding microalloying elements like niobium, titanium, or vanadium increases the temperature nonrecrystallization (T_{NR}), which is the temperature below which no complete static recrystallization between two rolling passes takes place. Higher rolling temperatures allow lower rolling forces but have the disadvantage of resulting in grain growth. Titanium as a microalloying element retards the grain coarsening because it leads to the formation of TiN precipitates. These TiN precipitates are stable at temperatures, where Nb is in solution and which often is the starting temperature of the rolling process.^[3] The equilibrium temperature for Nb(C,N) in austenite was estimated by Irvine et al.^[4,5] and is given in Equation (1).

1. Introduction

Modern high-strength low-alloy (HSLA) steels have to fulfill a combination of high strength and toughness. In general, these properties are contrary, due to the fact that a high strength normally decreases the toughness of the material. Nevertheless, a grain refinement increases both, the toughness and the strength of steels. For HSLA steels, thermomechanical rolling is the

$$\log \left[(m\%Nb) \left(m\%C + \frac{12}{14} m\%N \right) \right] = -\frac{6770}{T} + 2.26 \quad (1)$$

Nb delays the recrystallization of austenite in two ways. On the one hand, by the solute-drag effect and on the other hand, by precipitates. The solute-drag effect retards the recrystallization when Nb is dissolved in the austenite but is less effective than Nb-enriched precipitates, e.g., carbides, nitrides, and carbonitrides

S. Monschein, Dr. A. Landefeld, Prof. R. Schnitzer
Department of Materials Science
Montanuniversität Leoben
Franz-Josef Straße 18, 8700 Leoben, Austria
E-mail: Stefan.monschein@unileoben.ac.at

 The ORCID identification number(s) for the author(s) of this article can be found under <https://doi.org/10.1002/srin.202100065>.

© 2021 The Authors. Steel Research International published by Wiley-VCH GmbH. This is an open access article under the terms of the Creative Commons Attribution-NonCommercial-NoDerivs License, which permits use and distribution in any medium, provided the original work is properly cited, the use is non-commercial and no modifications or adaptations are made.

DOI: 10.1002/srin.202100065

Dr. M. Kapp
voestalpine Wire Rod Austria GmbH
Drahtstraße 1, 8792 St. Peter-Freienstein, Austria

Dr. M. Kapp
Erich Schmid Institute of Materials Science
Austrian Academy of Sciences
Jahnstraße 12, 8700 Leoben, Austria

D. Zügner
voestalpine Forschungsservicegesellschaft Donawitz GmbH
Kerpelystraße 199, 8700 Leoben, Austria

J. Fasching
voestalpine Stahl Donawitz GmbH
Kerpelystraße 199, 8700 Leoben, Austria

in austenite.^[6] A recent study published by Weibel et al.^[7] has shown that the amount of Nb dissolved in the matrix can be correlated with the electrical resistance of a Nb and Ti microalloyed steel. A further reason for the good recrystallization-inhibiting properties of Nb is its high diffusivity compared with other microalloying elements. For this reason, Nb interacts faster with interstitials and dislocations, thereby promoting faster formation of precipitates.^[8] Deformation in the austenite increases the number density of precipitates due to the creation of nucleation sites at dislocations.^[5,9,10] Nb precipitation can also occur in the ferrite, where their formation is even promoted because of a lower solubility.^[11] These fine particles also have the required size, around 5 nm, for increasing the strength via precipitation hardening.^[5,10,12]

Hong et al.^[13] have shown that adding Ti to a Nb-alloyed steel delays the start time of strain-induced NbC precipitation, because of a lower supersaturation of Nb in the austenite. This is because Nb already forms stable primary (Ti,Nb) carbonitrides, which remain during reheating, and therefore, Nb is less available in the matrix. Hegetschweiler et al.^[14] published similar results and showed that precipitates in a Nb and Ti microalloyed steel can be graded into two size-dependent groups. Precipitates with a size below 49 nm mainly contain Nb, whereas precipitates with a size above 49 nm were shown to be (Ti,Nb) carbonitrides.

In general, the kinetics of static recrystallization can be described with an Avrami-type equation.^[15]

$$X_a = 1 - \exp \left[-0.693 \left(\frac{t}{t_{0.5}} \right)^n \right] \quad (2)$$

where X_a is the recrystallized fraction depending on the time t , n is a constant, and $t_{0.5}$ is the time when half of the volume is recrystallized and can be calculated by Equation (3).^[15]

$$t_{0.5} = A \varepsilon^p \dot{\varepsilon}^q D^s e^{\frac{Q}{RT}} \quad (3)$$

ε is the strain, $\dot{\varepsilon}$ is the strain rate, D is the grain size, Q the activation energy, $R = 8.314 \text{ J}/(\text{molK})$, and p , q , s , and A are constants.

For the evaluation of the static recrystallization behavior, double-hit experiment is a common investigation method.^[1,16] In the past, several studies have shown that strain-induced precipitations inhibit static recrystallization, which can be seen in a deviation from Avrami-like behavior, i.e., the formation of a plateau in a recrystallization curve.^[17–20] An understanding of the precipitation behavior of the microalloying elements is therefore essential for controlling the thermomechanical rolling processes.

Nb and Ti microalloyed HSLA steels with C contents below 0.1 wt% have already been examined in detail in the past.^[13,21,22] However, the development toward lightweight construction requires higher strength levels for quenched and tempered steels not accessible with low-carbon levels. Thus, to enhance the steels' strength but simultaneously utilize the beneficial thermo-mechanical processing, the Ti–Nb microalloying concept was transferred to higher C contents. As the amount of carbon significantly impacts the precipitation kinetics, a thorough investigation of the recrystallization behavior is necessary to derive optimum annealing and deformation parameters for the desired microstructure. In addition, a sound experimental investigation

is of utmost importance to reveal how the precipitates' chemistry, size, and crystallography control recrystallization and structural fineness, which is the clue to design a high-strength and yet tough structural steel.

The goal of this work was to determine the influence of Nb and Ti on the recrystallization behavior of a low-alloyed steel with a C content of 0.23 wt%. For this reason, a common low-alloyed steel and a microalloyed HSLA steel were investigated in the as-rolled condition and after deformation using a deformation dilatometer. Special attention was paid to the influence of different process parameters, such as the annealing temperature and the finishing deformation temperature, on the static recrystallization behavior. Therefore, double-hit experiments were conducted.

The precipitates in the as-rolled condition and after several deformation steps were characterized via scanning transmission electron microscopy inside a scanning electron microscope (STEM-in-SEM), transmission kichu diffraction (TKD), energy-dispersive X-ray spectroscopy (EDX), and atom probe tomography (APT) to be able to draw conclusions about the correlation of the nanostructure and the recrystallization behavior.

2. Experimental Section

2.1. Investigated Materials

Table 1 shows the chemical composition of the two investigated steels. Steel 1 is a low-alloyed steel without microalloying elements, whereas steel 2 has a certain amount of Nb and Ti.

Both steels were annealed at a temperature of 1100 °C before rolling and went through an identical rolling process with a finishing rolling temperature between 800 and 900 °C.

2.2. Double-Hit Experiments

Double-hit experiments were conducted with a dilatometer DIL 805 A/D from TA Instruments. A schematic drawing of the applied time–temperature–deformation schedule is shown in **Figure 1**. Silicon nitride tools were used for the uniaxial compression of the material, and the size of the sample was 5 mm in diameter and 10 mm in length. The samples were fabricated via milling and lathing. To control the temperature during the processing, a type S thermocouple was spot welded onto the surface of the sample. The annealing process for steel 1 consisted of heating up to 1100 °C with a heating rate of +10 °C s^{−1} and holding for 5 min, subsequently followed by cooling with a cooling rate of −10 °C s^{−1} to the deformation temperature (T_{def}) of 850 or 900 °C, respectively. After 30 s, the first deformation hit was conducted with a strain of 0.2 and a strain rate of 10 s^{−1}. The interpass time (t_{inter}) between the two hits varied

Table 1. Chemical composition of steel 1 and steel 2.

		C	Mn	Ni	Cr	Mo	Si	Nb	Ti	Fe
Steel 1	[wt%]	0.23	1.25	0.48	0.48	0.23	0.21	0.00	0.00	bal.
Steel 1	[at%]	1.05	1.26	0.45	0.52	0.13	0.41	0.00	0.00	bal.
Steel 2	[wt%]	0.22	1.27	0.48	0.49	0.24	0.22	0.026	0.015	bal.
Steel 2	[at%]	1.00	1.28	0.45	0.52	0.14	0.44	0.016	0.018	bal.

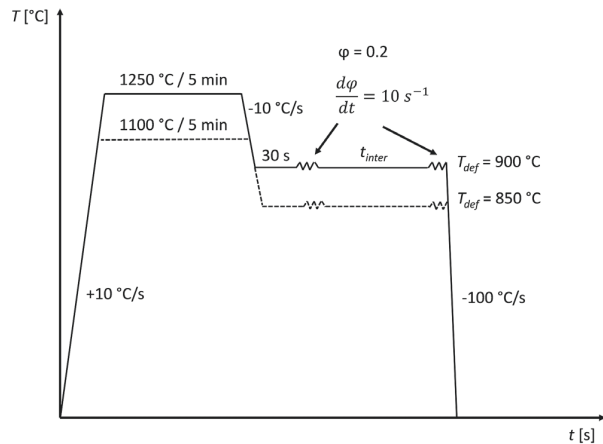


Figure 1. Schematic illustration of the double-hit experiment. Step 1: Heating to 1100 or 1250 °C with a heating rate of +10 °C s⁻¹ and holding the temperature for 5 min. Step 2: Cooling to the deformation temperature (T_{def}) of 850 °C or 900 °C with a cooling rate of -10 °C s⁻¹. Step 3: Waiting for 30 s. Step 4: Hit 1, strain = 0.2, strain rate = 10 s⁻¹. Step 5: Interspace time (t_{inter}) between 1 and 30 000 s. Step 6: Hit 2, strain = 0.2, strain rate = 10 s⁻¹. Step 7: Gas quenching with a cooling rate of -100 °C s⁻¹ to room temperature.

between 1 and 30 000 s. The deformation parameters for hit 2 were the same as for hit 1. After the second hit, the samples were gas quenched immediately with a cooling rate of -100 °C s⁻¹. In addition to the aforementioned parameters, for steel 2, heating to 1250 °C followed by a deformation at 850 °C was conducted. From the stress-strain curves obtained during deformation, recrystallization, respectively, fractional softening, was evaluated using the 5% true strain method.^[21]

2.3. Microstructural Characterization

The microstructure in the as-rolled condition was examined with light-optical microscopy. Therefore, the samples were ground with

SiC paper, polished with a 1 μm diamond suspension, and etched with 3% nital etchant. Electron backscatter diffraction (EBSD), STEM-in-SEM, EDX, and TKD were conducted with a FEI Versa 3D Dual Beam device. The characterization of the grain size in the as-rolled condition was done via EBSD using the software package TSL OIM Analysis 8. The precipitates of steel 2 in the as-rolled condition and after deformation were visualized via STEM-in-SEM. The thin-foil transmission electron microscopy specimens were prepared by polishing with SiC paper, subsequently followed by a thinning step in a double-jet electropolishing device. The precipitates in steel 2 in the as-rolled condition were extracted using a carbon replica method and chemically analyzed via EDX and TKD.^[23] For analyzing the precipitates after the deformation process, APT was used. Small rods with a cross section of 0.3 μm × 0.3 μm were cut out of the deformed dilatometer samples and tips were prepared with a standard two-step electropolishing method.^[24] The APT measurements were carried out with a LEAP 3000X HR from Cameca in the laser mode with a pulse frequency of 250 kHz, a base temperature of 40 K, and a laser energy of 60 pJ. The data reconstruction was done with the software IVAS 3.6.14 from Cameca.

3. Results

3.1. Double-Hit Experiments

To investigate the static recrystallization behavior, double-hit experiments were conducted. The results of these experiments are shown in **Figure 2**. Figure 2a shows the results for steel 1. The annealing temperature (T_a) in both experiments was 1100 °C and T_{def} was in one case 850 °C and in the other case 900 °C. To plot the two curves, it was necessary to determine the constants n and $t_{0.5}$ from Equation (2). This was done by linear regression from the evaluated fractional softening values. For steel 1, it can be seen that a T_{def} of 850 °C shifts the curve and, thus the recrystallization kinetics to longer times compared with T_{def} of 900 °C. This is in accordance with Equation (3). The same behavior for a T_a of 1100 °C is shown for steel 2 in Figure 2b. For

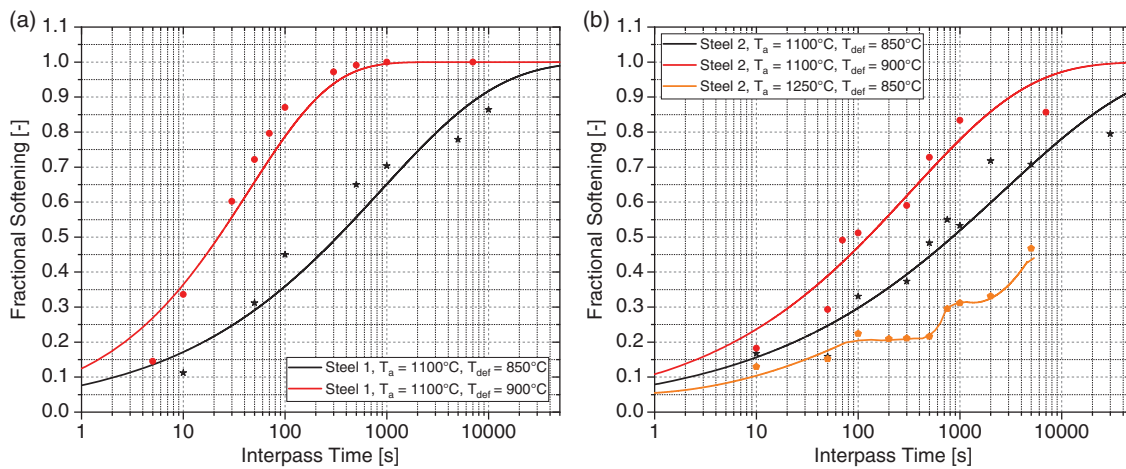


Figure 2. Fractional softening determined by double-hit experiments using the 5% true strain method for a) steel 1: $T_a = 1100$ °C and $T_{\text{def}} = 850$ °C and $T_a = 1100$ °C and $T_{\text{def}} = 900$ °C and b) steel 2: $T_a = 1100$ °C and $T_{\text{def}} = 850$ °C, $T_a = 1100$ °C and $T_{\text{def}} = 900$ °C, and $T_a = 1250$ °C and $T_{\text{def}} = 850$ °C.

Table 2. $t_{0.5}$ values for steel 1 and steel 2 after different deformation conditions.

	$T_a = 1100\text{ }^\circ\text{C}$ and $T_{def} = 850\text{ }^\circ\text{C}$	$T_a = 1100\text{ }^\circ\text{C}$ and $T_{def} = 900\text{ }^\circ\text{C}$
	$t_{0.5}$ [s]	$t_{0.5}$ [s]
Steel 1	325.5	22.1
Steel 2	839.4	124.5

the two curves with a T_a of $1100\text{ }^\circ\text{C}$, the constants n and $t_{0.5}$ were also determined by linear regression. To investigate the influence of dissolved Nb in steel 2, further measurements were carried out with a T_a of $1250\text{ }^\circ\text{C}$. According to Equation (1), this temperature is above the equilibrium solution temperature of Nb(C,N) and led therefore to the complete dissolution of the precipitates after 5 min of annealing. The T_a of $1250\text{ }^\circ\text{C}$ followed by a T_{def} of $850\text{ }^\circ\text{C}$ results in a plateau in the recrystallization curve at a t_{inter} between 100 and 750 s. For this reason, it was not possible to use

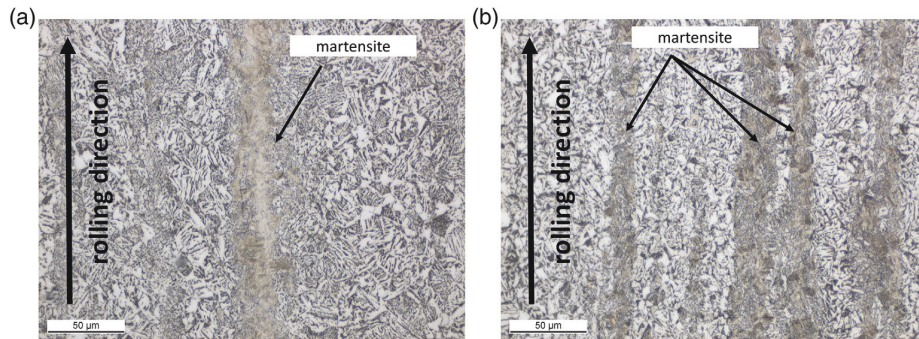


Figure 3. Optical micrographs of the as-rolled condition for a) steel 1 and b) steel 2. The samples were etched with 3% nital etchant. Martensitic areas parallel to the rolling direction are highlighted with arrows between a ferritic/bainitic matrix. The microstructure of steel 2 seems finer than for steel 1.

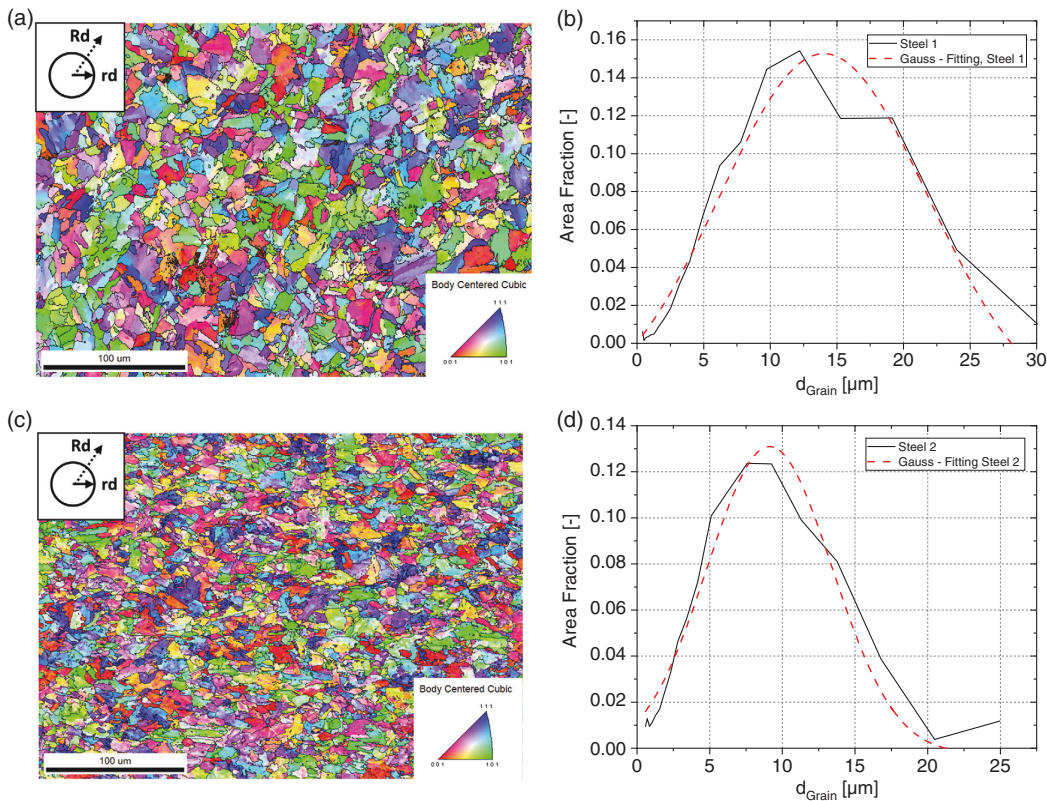


Figure 4. a,c) IPF maps after an EBSD scan of steel 1 and steel 2 in the bainitic as-rolled condition perpendicular to the radial direction (rd). The rolling direction (Rd) is in the plane of the images. b,d) Grain size distribution of the corresponding EBSD images of steel 1 and steel 2. The grain tolerance angle was set at 5° .

the model from Equation (2), which is why the curve was drawn manually. The $t_{0.5}$ values for a T_a of 1100 °C are shown in Table 2, which demonstrates that the recrystallization behavior of steel 2 is inhibited compared with steel 1.

3.2. Microstructure

The microstructure of steel 1 and steel 2 in the as-rolled condition is shown in Figure 3. The matrix consists of a ferritic/bainitic microstructure, which has martensitic areas parallel to the rolling direction. The microstructure for steel 2 seems finer in the as-rolled condition compared with steel 1. To quantify this behavior, EBSD measurements were carried out in the as-rolled condition to evaluate the mean grain size. The results are shown in Figure 4. Figure 4a,c shows the inverse pole figure (IPF) maps of the EBSD measurements of the as-rolled condition of steel 1 and steel 2, respectively. The black lines indicate the high-angle

grain boundaries, whose misorientation is higher than 15°. Figure 4b,d shows the corresponding grain size distribution of the EBSD images for steel 1 and steel 2, respectively. The grain tolerance angle, which was used to create the grain size distribution, was set to 5°. The medium grain size for steel 1 is around 15 µm, whereas the value for steel 2 is around 9 µm.

To conduct an in-depth characterization of the microstructure in the as-rolled condition and reveal their influence on the recrystallization behavior, high-resolution characterization methods such as STEM-in-SEM, EDX, and TKD were used. Figure 5a,b shows STEM-in-SEM-images of steel 2 in the as-rolled condition. Figure 5a shows various ferrite grains with two carbide laths marked with arrows. Figure 5b shows small rectangular precipitates with an average size of around 15 nm evenly distributed within the grain.

To better understand the influence of T_a and t_{inter} on the precipitation behavior, STEM-in-SEM-analysis was conducted

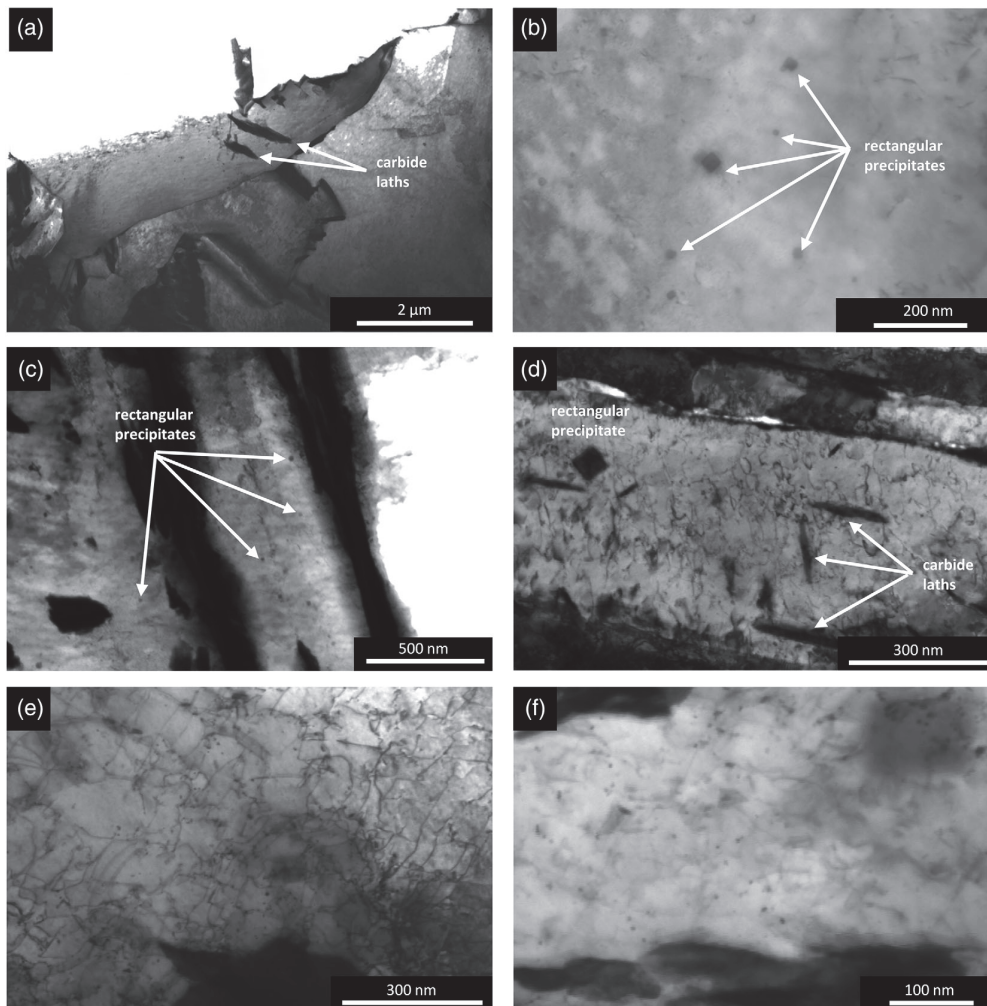


Figure 5. STEM-in-SEM images of steel 2 in the as-rolled condition and on samples at various states along the recrystallization curves after the double-hit experiments. a,b) As-rolled condition. c) $T_a = 1100$ °C, $T_{def} = 850$ °C, and $t_{inter} = 300$ s. d) $T_a = 1250$ °C, $T_{def} = 850$ °C, and $t_{inter} = 10$ s. e,f) $T_a = 1250$ °C, $T_{def} = 850$ °C, and $t_{inter} = 300$ s (higher magnification in (f)).

on samples along certain points of the recrystallization curve, as shown in Figure 2.

Figure 5c shows a STEM-in-SEM-image of a deformed and quenched dilatometer sample after $T_a = 1100^\circ\text{C}$, $T_{\text{def}} = 850^\circ\text{C}$, and $t_{\text{inter}} = 300$ s. As in the as-rolled condition, rectangular precipitates with an average size of around 15 nm are visible in the ferrite. Figure 5d shows a STEM-in-SEM-image of a deformed and quenched dilatometer sample after $T_a = 1250^\circ\text{C}$, $T_{\text{def}} = 850^\circ\text{C}$, and $t_{\text{inter}} = 10$ s, prior to the plateau in Figure 2b. The grain in Figure 5d consists of 100–300 nm large carbide laths, a 50 nm large precipitate, and a few small precipitates with a size of 5–10 nm along the dislocation lines.

Figure 5e,f shows STEM-in-SEM-images of a deformed and quenched dilatometer sample after $T_a = 1250^\circ\text{C}$, $T_{\text{def}} = 850^\circ\text{C}$, and $t_{\text{inter}} = 300$ s, which corresponds to the area in the plateau in Figure 2b. Small precipitates with a size of around 5–10 nm close to dislocation lines were found in a much higher number in Figure 5e,f compared with a short t_{inter} of 10 s in Figure 5d.

The STEM-in-SEM-images in Figure 5 show different precipitation behaviors in the as-rolled condition and after deformations conducted by double-hit experiments. For a further determination of the chemical composition of the precipitates, EDX and TKD measurements on carbon replica foils were carried out.

Figure 6 shows STEM-in-SEM-images and corresponding spectra of EDX measurements of the precipitates in the as-rolled

condition of steel 2, which were extracted using the carbon replica method. Figure 6a shows a particle with a size at around 20 nm (marked with a red circle). The associated EDX spectrum in Figure 6b shows that Ti, C, N, and Al peaks were detected. The Al peak appears dominant and stems from the aluminum sample holder.

A bigger precipitate with a size of around 90 nm was analyzed in Figure 6c and shows an additional Nb peak in the corresponding EDX spectrum in Figure 6d. The Cu peaks in Figure 6d stem from the grid on which the carbon replica foil was placed.

The EDX measurements enabled a qualitative chemical analysis of the particles, thus allowing for fast screening, but are not capable of revealing the crystallographic structure of the precipitates. Therefore, TKD measurements were carried out on the carbon replica foils. Figure 7a shows a 20 nm small precipitate and the associated Kikuchi pattern is shown in Figure 7b. The colored lines in Figure 7c correspond to the best matching solution according to the database of the software package TEAM v. 4.3. The results were compared with a body-centered cubic (bcc) NbC structure and a bcc ferrite structure and show that the best match is obtained using a bcc TiN structure.

Using the carbon replica method allowed an analysis of the cubic particles, which are larger than 10 nm, whereas the smaller precipitates in steel 2 could not be characterized with these

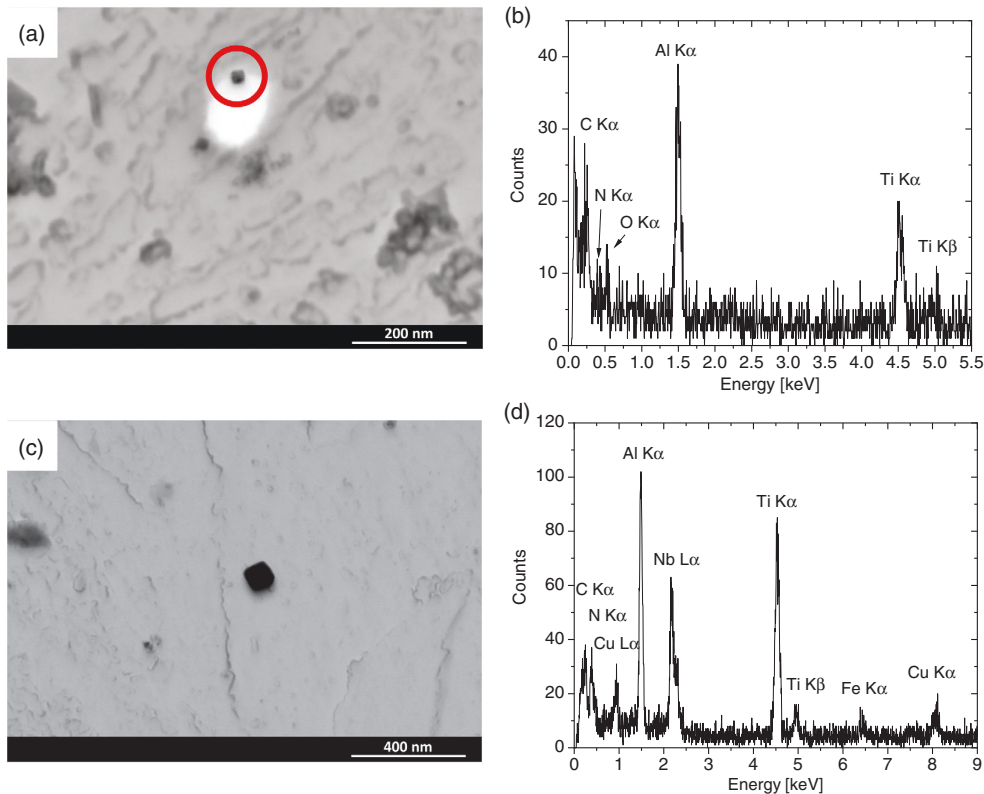


Figure 6. a) STEM-in-SEM image of a 20 nm rectangular precipitate in steel 2 in the as-rolled condition and b) the corresponding EDX spectra. The Al peak stems from the sample holder. c) STEM-in-SEM image of a 90 nm rectangular precipitate in steel 2 in the as-rolled condition and d) the corresponding EDX spectra. The Al and Cu peak stem from the sample holder and the sample grid, respectively.

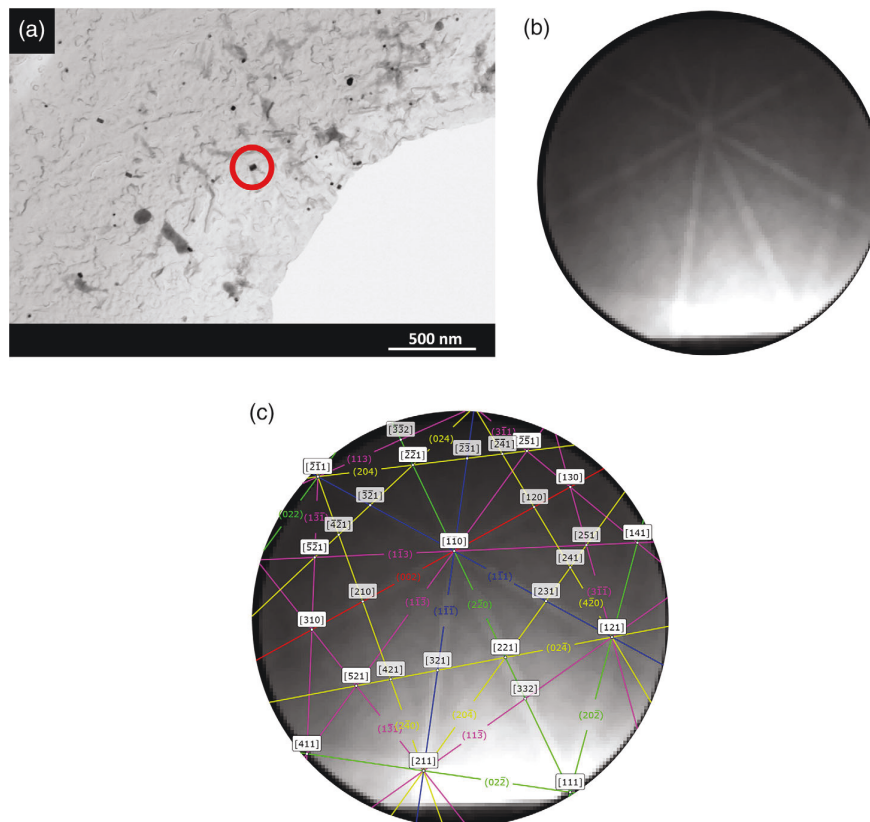


Figure 7. a) A 20 nm small precipitate in the as-rolled condition of steel 2 extracted via carbon replica method. b) Kikuchi pattern after TKD with the best matching solution according to the database in the software package TEAM v. 4.3 in c).

methods. For this reason, APT was used, as this method enables the analysis of even the smallest precipitate, thanks to its almost atomic resolution. To analyze the precipitates that are formed in the plateau of the recrystallization curve, which is shown in Figure 2b, APT measurements were carried out before the plateau and in the area of the plateau.

Figure 8 shows 3D reconstructions of APT measurements on samples after the double-hit deformation tests. Figure 8a shows a measurement of steel 2 taken after $T_a = 1250\text{ }^\circ\text{C}$, $T_{\text{def}} = 850\text{ }^\circ\text{C}$, and $t_{\text{inter}} = 10\text{ s}$ and shows clustering (green circle) of C atoms, whereas Nb is distributed evenly across the whole tip. The proxigrams in Figure 8b and Figure 8c also reveal that only a clustering of C atoms occurred, whereas the concentration of the other alloying elements is evenly distributed. An APT measurement, which reveals the small precipitates in steel 2 after $T_a = 1250\text{ }^\circ\text{C}$, $T_{\text{def}} = 850\text{ }^\circ\text{C}$, and $t_{\text{inter}} = 300\text{ s}$, is shown in Figure 8d. The proxigrams in Figure 8e,f of the three precipitates reveal that the precipitates are carbides with around 40 at% Nb, 5–10 at% N, and small amounts of Mo, Cr, and Ti.

4. Discussion

To determine the recrystallization and precipitation behavior of a low-alloyed and a microalloyed HSLA steel, the steels were first

investigated in the as-rolled condition using high-resolution techniques such as STEM-in-SEM, TKD, and EDX. Figure 3 and 4 show that the microstructure in the as-rolled condition is finer for the microalloyed steel compared with steel 1. The annealing temperature before rolling was set to $1100\text{ }^\circ\text{C}$ and was below the equilibrium solution temperature of Nb(C,N) according to Equation (2). STEM-in-SEM-images of steel 2 in Figure 5a,b and TKD measurements on carbon replica samples of steel 2 have shown that TiN particles with an average size of around 15 nm were present in the as-rolled condition. It seems that these precipitates were responsible for the finer grain structure of steel 2. These particles inhibited grain growth during the annealing process, which led to the finer microstructure after the rolling process. The EDX spectrum in Figure 6a shows that the small rectangular particles mainly contain Ti and N, whereas certain amounts of Nb are found in bigger particles (Figure 6b). This is also in accordance with Hong et al.^[13] and Hegetschweiler et al.,^[14] who have shown that Nb nucleates on TiN precipitates in Nb–Ti microalloyed HSLA steels.

The recrystallization behavior was investigated using double-hit experiments, whereby, both the annealing and the final deformation temperature were varied. The results were analyzed using the 5% true strain method. This evaluation method was chosen to limit the effect of recovery on the fractional softening.^[1] It has been shown for both steels that a higher deformation temperature leads

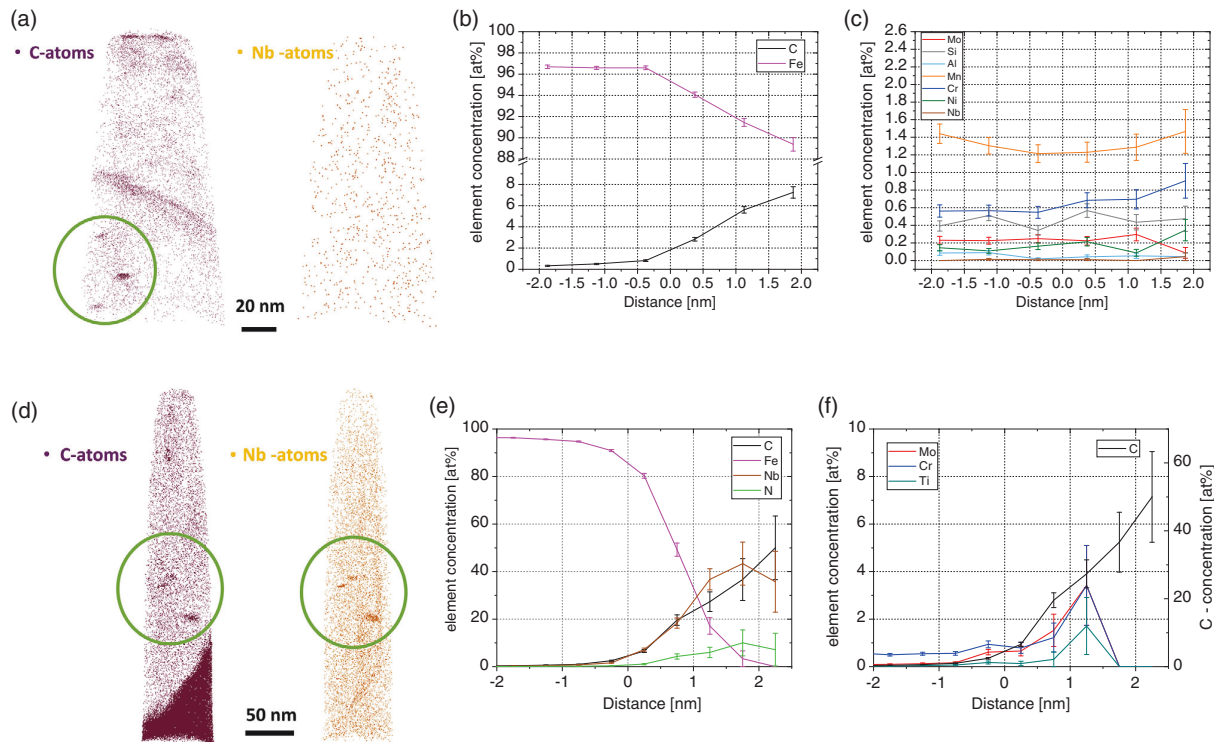


Figure 8. Reconstruction of APT measurements of deformed dilatometer samples of steel 2 with $T_a = 1250\text{ }^\circ\text{C}$ and $T_{def} = 850\text{ }^\circ\text{C}$ a) before the plateau at $t_{inter} = 10\text{ s}$ and d) in the area of the plateau at $t_{inter} = 300\text{ s}$. b,c,e,f) The proxigrams show the chemical composition of C clusters (marked with green circles) in the tips.

to faster recrystallization, which is detrimental to realize a fine prior austenite grain size and a tough final martensitic structure. From Figure 2 and Table 2, it is shown that, under the same experimental conditions ($T_a = 1100\text{ }^\circ\text{C}$ and $T_{def} = 850$ and $900\text{ }^\circ\text{C}$), the recrystallization of steel 2 is retarded compared with steel 1. This is in contradiction to the finer microstructure prior deformation.^[1] In general, a finer austenitic grain structure leads to more potential nucleation sites for recrystallization, which is why the slower recrystallization behavior for steel 2 can only be explained by the addition of Ti and Nb. STEM-in-SEM-images (Figure 5c) did not reveal the formation of fine NbC precipitates in steel 2 for an annealing temperature of $1100\text{ }^\circ\text{C}$ prior to the double compression steps in the double deformation tests. Therefore, the retarded recrystallization of steel 2 compared with steel 1 is most probably due to the TiN precipitates in the matrix. Another explanation for the slower recrystallization behavior is the solute-drag effect of dissolved Nb next to the grain boundaries. This effect should be small, as the annealing temperature of $1100\text{ }^\circ\text{C}$ is below the equilibrium solution temperature of NbC. Therefore, only small amounts of Nb should be present in the dissolved form in the matrix after annealing.

When the annealing temperature was set to $1250\text{ }^\circ\text{C}$ for steel 2, the recrystallization behavior was retarded compared with $1100\text{ }^\circ\text{C}$, which is shown in Figure 2b. The additional formation of a plateau indicates strain-induced precipitation. These precipitates, in combination with a bigger austenite grain size due to the

higher annealing temperature, are responsible for the retarded recrystallization behavior compared with an annealing temperature of $1100\text{ }^\circ\text{C}$. STEM-in-SEM-images in Figure 5d,e,f show fine precipitates close to dislocation lines after the double-hit experiments after annealing at $1250\text{ }^\circ\text{C}$. APT measurements of samples at interpass times prior to the occurrence of the plateau in the recrystallization diagram, an example of which is shown in Figure 8a, revealed that no NbC was found in the APT tips. The precipitates which are shown in Figure 5d for an interpass time of 10 s are mainly clusters of carbon with no enrichment of other alloying elements. To analyze the strain-induced precipitates in the area of the plateau, further APT measurements after an interpass time of 300 s were carried out. The reconstruction of one measurement is shown in Figure 8b and reveals that the particles are NbC precipitates with certain amounts of N, Ti, and Mo. The results of this work coincide well with the results of other research groups, which have described similar recrystallization behavior for different HSLA steels in the past.^[17,18,20]

Particularly, in this work, it was shown that the annealing temperature before deformation is decisive for an increased recrystallization-inhibiting effect of Nb- and Ti-alloyed HSLA steels. Annealing temperatures below the equilibrium solution temperature of Nb(C,N) do not ensure sufficient dissolution of Nb and, thus, prevent the formation of strain-induced precipitates after deformation. When the annealing temperature is high enough, a complete dissolution of Nb(C,N) during annealing takes

place, which is necessary for the precipitation of strain-induced particles. Given a C content of 0.25 wt%, at least an annealing temperature of 1250 °C is required to derive the optimum fine-scaled microstructure related to the Ti–Nb microalloying concept. With respect to higher C contents, annealing at even higher temperatures might be necessary to make use of the beneficial strain-induced NbC. Thus, an optimized annealing temperature is indispensable to improve toughness and strength by effective grain refinement in the final quench and tempering treatment.

5. Conclusion

In this study, a low-alloyed steel and a microalloyed HSLA steel were investigated in the as-rolled condition and with double-hit experiments under various deformation parameters. The precipitation behavior was analyzed using high-resolution characterization methods. The results of this work allow to draw the following conclusions. 1) In the as-rolled condition the microalloyed steel had a finer microstructure compared with the alloy without the addition of Nb and Ti, although the annealing temperature prior to the rolling process was set below the equilibrium solution temperature of Nb(C,N). STEM-in-SEM, TKD, and EDX measurements have shown that TiN precipitates with an average size of around 15 nm were distributed evenly in the ferritic/bainitic matrix. These precipitates inhibited the grain growth during annealing prior to rolling and led to a finer microstructure. 2) The results of the double-hit experiments have shown that a higher deformation temperature leads to faster recrystallization. 3) At an annealing temperature of 1100 °C, the recrystallization behavior of the microalloyed steel was retarded compared with steel 1. A combination of TiN precipitates and the solute-drag effect was responsible for the retarded recrystallization. 4) The recrystallization in steel 2 was retarded at an annealing temperature of 1250 °C compared with an annealing temperature of 1100 °C. This was due to a bigger austenite grain size after the annealing step and the formation of strain-induced NbC precipitates, which were revealed by STEM-in-SEM and APT measurements. The precipitates are indicated via a plateau in the recrystallization curve and occur at interpass times between 100 and 750 s. 5) It was proofed that increasing the annealing temperatures close to the equilibrium solution temperature of Nb(C,N) has a stronger impact on the recrystallization behavior than mere reduction of the final deformation temperature. Depending on the cooling parameters, this leads to a finer bainitic or martensitic structure after deformation and subsequently improved toughness and strength.

Acknowledgements

Funding of the Austrian BMK (846933) in the framework of the program “Production of the future” and the “BMK Professorship for Industry” is gratefully acknowledged.

Conflict of Interest

The authors declare no conflict of interest.

Data Availability Statement

Research data are not shared.

Keywords

atom probe tomography, double-hit deformation test, microalloyed steels, scanning transmission electron microscopy in a scanning electron microscope, static recrystallization, steels, titanium

Received: January 28, 2021

Revised: March 16, 2021

Published online:

- [1] S. Vervynck, K. Verbeken, B. Lopez, J. J. Jonas, *Int. Mater. Rev.* **2012**, *57*, 187.
- [2] A. J. DeArdo, *Int. Mater. Rev.* **2003**, *48*, 371.
- [3] a) T. N. Baker, *Ironmak. Steelmak.* **2016**, *43*, 264; b) L. J. Cuddy, J. C. Raley, *Metall. Trans. A* **1983**, *14A*, 1989.
- [4] K. J. Irvine, F. B. Pickering, T. Gladman, *J. Iron Steel Res. Int.* **1967**, *205*, 161.
- [5] C. Klinkenberg, K. Hulka, W. Bleck, *Steel Res. Int.* **2004**, *75*, 744.
- [6] a) S. S. Hansen, J. V. Sande, M. Cohen, *Metall. Mater. Trans. A* **1980**, *11*, 387; b) J. G. Speer, S. S. Hansen, *Metall. Mater. Trans. A* **1989**, *20*, 25; c) S. Vervynck, K. Verbeken, P. Thibaux, M. Liebeherr, Y. Houbaert, *ISIJ Int.* **2009**, *49*, 911; d) P. Gong, E. J. Palmiere, W. M. Rainforth, *Acta Mater.* **2015**, *97*, 392.
- [7] J. Webel, A. Herges, D. Britz, E. Detemple, V. Flaxa, H. Mohrbacher, F. Mücklich, *Metals* **2020**, *10*, 243.
- [8] N. Maruyama, R. Uemori, M. Sugiyama, *Mater. Sci. Eng. A* **1998**, *250*, 2.
- [9] a) B. Dutta, C. M. Sellars, *Mater. Sci. Technol.* **1987**, *3*, 197; b) B. Dutta, E. J. Palmiere, C. M. Sellars, *Acta Mater.* **2001**, *49*, 785; c) W. J. Liu, *Metall. Mater. Trans. A* **1995**, *26*, 1641.
- [10] Y.-B. Cao, F.-R. Xiao, G.-Y. Qiao, C.-J. Huang, X.-B. Zhang, Z.-X. Wu, B. Liao, *Mater. Sci. Eng. A* **2012**, *552*, 502.
- [11] M. G. Burke, L. J. Cuddy, J. Piller, M. K. Miller, *Mater. Sci. Technol.* **1988**, *4*, 113.
- [12] M. Charleux, W. J. Poole, M. Militzer, A. Deschamps, *Metall. Mater. Trans. A* **2001**, *32A*, 1635.
- [13] S. G. Hong, K. B. Kang, C. G. Park, *Scr. Mater.* **2002**, *46*, 163.
- [14] A. Hegetschweiler, O. Borovinskaya, T. Staudt, T. Kraus, *Analyt. Chem.* **2019**, *91*, 943.
- [15] S. F. Medina, V. Lopez, *ISIJ Int.* **1993**, *33*, 605.
- [16] C. N. Homsher, *Master Thesis*, Colorado School of Mines **2013**.
- [17] S. F. Medina, J. E. Mancilla, *ISIJ Int.* **1993**, *33*, 1257.
- [18] S. F. Medina, J. E. Mancilla, *Acta Metall. Mater.* **1994**, *42*, 3945.
- [19] a) S. F. Medina, J. E. Mancilla, *ISIJ Int.* **1996**, *36*, 1063; b) S. F. Medina, J. E. Mancilla, *ISIJ Int.* **1996**, *36*, 1077.
- [20] R. Esterl, M. Sonnleitner, R. Schnitzer, *Steel Res. Int.* **2019**, *90*, 1800500.
- [21] S. Vervynck, K. Verbeken, P. Thibaux, Y. Houbaert, *Steel Res. Int.* **2010**, *81*, 234.
- [22] S. Vervynck, K. Verbeken, P. Thibaux, Y. Houbaert, *Steel Res. Int.* **2011**, *82*, 369.
- [23] A. Bhattacharya, C. M. Parish, J. Henry, Y. Katoh, *Ultramicroscopy* **2019**, *202*, 33.
- [24] I. Blum, F. Cuvilly, W. Lefebvre-Ulrikson, in *Atom Probe Tomography: Put Theory into Practice* (Ed: W. Lefebvre-Ulrikson), Academic Press, London **2016**, pp. 97–123.

Paper III

Stefan Monschein, Katharina S. Ragger, Dominik Zügner, Josef Fasching and Ronald Schnitzer

Influence of the Ti Content on the Grain Stability and the Recrystallization Behavior of Nb Alloyed HSLA Steels

steel research international 2022, 2200094;

DOI: 10.1002/srin.202200094

Influence of the Ti Content on the Grain Stability and the Recrystallization Behavior of Nb-Alloyed High-Strength Low-Alloyed Steels

Stefan Monschein,* Katharina S. Ragger, Dominik Zügner, Josef Fasching, and Ronald Schnitzer

To achieve higher strength and good hardenability and at the same time use the positive effects of thermomechanical controlled processing, the concept of Nb and Ti microalloyed steels is increasingly used for high-strength low-alloy (HSLA) steels with higher C contents. Herein, how the addition of Ti affects the grain growth and static recrystallization behavior of a Nb microalloyed HSLA steel with a C content of 0.23 wt% is investigated. For this reason, alloys with varying Ti and constant Nb content are produced and investigated by means of annealing and double-hit deformation experiments. Atom probe tomography measurements reveal that the Nb concentration in the matrix decreases with increasing Ti content. Therefore, the static recrystallization behavior is steadily inhibited with decreasing Ti content, as more dissolved Nb is available for the formation of strain-induced NbC precipitates. The annealing experiments show that the combined addition of Ti and Nb is most effective against grain coarsening, regardless of whether the Ti content is 90 or 180 ppm. To use the positive properties of Ti against grain coarsening and Nb to inhibit recrystallization, a middle content must be chosen when alloying Ti to HSLA steels with higher C content.

1. Introduction

The development of modern high-strength low-alloy (HSLA) steels aims for high strength and toughness through the addition of microalloying elements, such as Nb, Ti, and V and thermomechanical controlled processing (TMCP).^[1] Nb and Ti are among the two most important microalloying elements in HSLA steels, as both elements complement each other very well.^[2] On the one hand, the annealing temperature (T_a) prior to the rolling process must be high enough to bring Nb into solution, and on the other hand, high temperatures above 1100 °C can lead to abnormal grain growth, which in turn would have a negative effect on the mechanical properties of the rolled product.^[3] Therefore, Ti is added to the steel, which leads to the formation of stable TiN precipitates.^[4] These precipitates are able to inhibit grain growth at elevated temperatures, where Nb is in solution and which often is the starting

temperature of the rolling process. Hence, higher rolling starting temperatures can be chosen, which enable lower rolling forces. Nb is mainly alloyed because of its excellent recrystallization-inhibiting properties and its strengthening effect through 5–10 nm fine NbC particles.^[5] Both dissolved Nb at austenite grain boundaries and strain-induced NbC precipitates inhibit the recrystallization of the microstructure through the solute drag effect and a pinning effect, respectively. The formation of strain-induced NbC precipitates is promoted by the presence of deformation-induced dislocations in austenite, as these serve as nucleation sites.^[6] To be able to realize rolling processes on an industrial scale under optimal rolling conditions, an understanding of the precipitation behavior of the microalloying elements is therefore of utmost importance, as these precipitates directly affect the recrystallization behavior.


To investigate the static recrystallization behavior, the so-called double-hit experiments are common methods.^[2,7] These experiments allow an indirect determination of the degree of static recrystallization. Interactions between Nb and Ti with regard to precipitation and recrystallization behavior must be taken into account and were already investigated in the past for HSLA steels with typical C levels below 0.1 wt%.^[8,9] For

S. Monschein, R. Schnitzer
Department of Materials Science
Montanuniversität Leoben
Franz - Josef Straße 18, 8700 Leoben, Austria
E-mail: Stefan.monschein@unileoben.ac.at

K. S. Ragger
voestalpine Wire Rod Austria GmbH
Drahtstraße 1, 8792 St. Peter - Freienstein, Austria

D. Zügner
voestalpine Forschungsservicegesellschaft Donawitz GmbH
Kerpelystraße 199, 8700 Leoben, Austria

J. Fasching
voestalpine Stahl Donawitz GmbH
Kerpelystraße 199, 8700 Leoben, Austria

 The ORCID identification number(s) for the author(s) of this article can be found under <https://doi.org/10.1002/srin.202200094>.

© 2022 The Authors. Steel Research International published by Wiley-VCH GmbH. This is an open access article under the terms of the Creative Commons Attribution-NonCommercial-NoDerivs License, which permits use and distribution in any medium, provided the original work is properly cited, the use is non-commercial and no modifications or adaptations are made.

DOI: 10.1002/srin.202200094

example, Hong et al.^[8] could show that the NbC precipitation start time was shifted toward longer times due to the addition of Ti. A lower concentration of dissolved Nb in the matrix is responsible for this behavior, as certain amounts of Nb have already been bound to (Ti,Nb)(C,N) precipitates. Therefore, less Nb was available for the formation of strain-induced NbC. Similar results were shown by Hegetschweiler et al.,^[10] which could show that precipitates above a certain size were shown to be (Ti,Nb) carbonitrides.

HSLA steels usually have a low C content of less than 0.1 wt%. However, this limits their use for high-strength applications and lowers their hardenability, as both properties strongly depend on the C content of the steel.^[11] To achieve higher strength and at the same time use the positive effects of TMCP, the concept of Nb and Ti microalloyed steels is increasingly used for steels with higher C contents. The positive effects of these two elements on the recrystallization behavior, as well as on the grain refinement in a HSLA steel alloyed with 0.23 wt% C, could be shown in a recently published work by the authors.^[12] To further investigate microalloyed HSLA steels with C contents above 0.2 wt%, the aim of this work was to investigate how different Ti contents affect the grain growth and recrystallization behavior of Nb microalloyed HSLA steel.

For this reason, alloys with a constant Nb content of around 200 ppm, but a varying Ti content between 20 and 180 ppm were produced. Both grain coarsening and recrystallization behavior were investigated by means of annealing experiments and double-hit deformation tests, respectively, and compared with a microalloy-free steel. After the double-hit deformation experiments, atom probe tomography (APT) was used to characterize the precipitates and the chemical composition of the deformed samples.

2. Experimental Section

2.1. Investigated Materials

The chemical composition of the investigated steels is displayed in Table 1. The reference alloy (Ref) did not contain any microalloying elements, whereas the Ti content in MA1–MA3 varied with the Nb content remaining constant. As the chemical composition of deformed samples was determined by APT measurements in this work, the chemical composition of the investigated steels was given both in wt% and at%.

Table 1. Chemical composition of the investigated steels.

		Fe	C	N	Mn	Si	Cr	Ni	Al	Mo	Nb	Ti
Ref	wt%	bal.	0.21	0.005	1.33	0.21	0.57	1.06	0.04	0.56	–	–
Ref	at%	bal.	0.99	0.021	1.34	0.41	0.61	1.00	0.07	0.32	–	–
MA1	wt%	bal.	0.24	0.012	1.34	0.20	0.56	1.05	0.02	0.55	0.022	0.002
MA1	at%	bal.	1.12	0.045	1.35	0.39	0.59	0.99	0.04	0.32	0.013	0.003
MA2	wt%	bal.	0.24	0.012	1.32	0.20	0.55	1.04	0.02	0.54	0.020	0.009
MA2	at%	bal.	1.09	0.048	1.33	0.39	0.59	0.98	0.04	0.31	0.012	0.010
MA3	wt%	bal.	0.24	0.014	1.32	0.20	0.55	1.04	0.02	0.54	0.021	0.018
MA3	at%	bal.	1.10	0.055	1.33	0.39	0.59	0.98	0.04	0.31	0.013	0.021

The alloys were prepared by vacuum induction melting to ingots. After reannealing to 1150 °C the ingots were forged to a diameter of 30 mm.

2.2. Annealing Experiments

For the annealing experiments, 10 mm-thick pieces were cut off the forged specimens and were annealed at temperatures (T_a) between 900 and 1300 °C for 30 min (t_a) in a Carbolite RHF chamber furnace. After the annealing process, the specimens were directly quenched into water. A schematic drawing of the applied time–temperature schedule is shown in Figure 1.

The quenched specimens were ground with SiC paper and polished with a diamond suspension up to a grain size of 1 μm. To visualize the prior austenite grain boundaries (PAGBs), a picric acid-based etchant from CRIDA Chemie was used for etching. The samples were etched for 10–15 min and cleaned with water and isopropanol. After that, the microstructure was examined with light optical microscopy (LOM) with a ZEISS Axio Imager M1 microscope. The size of the prior austenite grains (PAGs) was determined using the DIN EN ISO 643 standard.

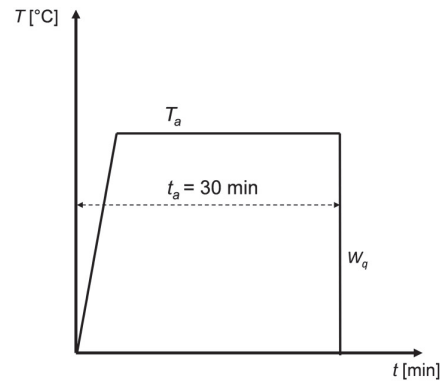


Figure 1. Schematic illustration of the annealing experiment. The samples were heated to an annealing temperature (T_a) between 900 and 1300 °C and the entire annealing process (t_a) lasted 30 min. After annealing, the samples were directly quenched in water (W_q).

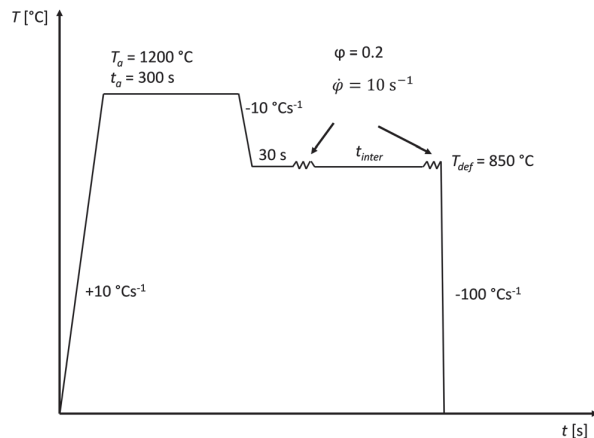


Figure 2. Schematic illustration of the double-hit experiment. Step 1: Heating to 1200 °C with a heating rate of +10 °C s⁻¹ and holding for 300 s. Step 2: Cooling to deformation temperature (T_{def}) of 850 °C with a cooling rate of -10 °C s⁻¹. Step 3: Waiting for 30 s. Step 4: Hit 1, $\varphi = 0.2$ and $\dot{\varphi} = 10 \text{ s}^{-1}$. Step 5: Interpass time (t_{inter}) between 10 and 10000 s. Step 6: Hit 2, $\varphi = 0.2$ and $\dot{\varphi} = 10 \text{ s}^{-1}$. Step 7: Gas quenching to room temperature with a cooling rate of -100 °C s⁻¹.

2.3. Double-Hit Experiments

The static recrystallization behavior of the alloys was investigated using double-hit experiments, which were carried out with a deformation dilatometer DIL 805 A/D/T from TA instruments. Silicon nitride tools were used for the uniaxial compression of the material and the size of the sample was 5 mm in diameter and 10 mm in length. To control the temperature during the processing, a type S thermocouple was spot welded onto the surface of the sample. A schematic drawing of the time-temperature-deformation schedule is shown in **Figure 2**. The samples were heated up to a T_a of 1200 °C with a heating rate of +10 °C s⁻¹ and held for 300 s. In the next step, the samples were cooled down to the deformation temperature (T_{def}) of 850 °C with a cooling rate of -10 °C s⁻¹. After waiting for 30 s, the first deformation hit was carried out with a strain (φ) of 0.2 and a strain rate ($\dot{\varphi}$) of 10 s⁻¹. The interpass time (t_{inter}) between the first and the second hit was varied between 10 and 10000 s followed by the second deformation hit, which had the same deformation parameters as hit 1. Directly after the second hit, the samples were gas quenched down to room temperature with a cooling rate of -100 °C s⁻¹. The degree of static recrystallization, respectively, fractional softening, was determined using the 5% true strain method on the recorded stress-strain curves of the two deformation hits.^[2]

2.4. Microstructural and Chemical Characterization

APT was used for analyzing the precipitates and the chemical composition of the matrix after certain conditions after the deformation process. Therefore, rods with a cross section of 0.3 mm × 0.3 mm were cut out of the deformed dilatometer samples and APT tips were prepared by a standard electropolishing method.^[13] The APT measurements were carried out with a

LEAP 3000X HR from Cameca in the laser mode with a pulse frequency of 250 kHz, a base temperature of 40 K, and a laser energy of 60 pJ. The data reconstruction was done with the software IVAS 3.6.14 from Cameca. With APT, peak overlaps could occur within the mass spectrum. In the present case, Nb had a unique Nb²⁺ peak at 46.5 Da in the mass spectrum but a peak overlap of Nb³⁺ with Ni²⁺ at 31 Da. The peak at 31 Da was labeled as Ni due to the higher Ni content in all alloys. The software IVAS 3.6.14 offered the possibility of peak decomposition, which means that the actual concentration of the alloying elements was calculated if there was a peak overlap with two or more elements.

3. Results

3.1. Annealing Experiments

The results of the determination of the mean PAG size (d_{mean}) depending on the annealing temperature are shown in **Figure 3**. In the logarithmic scale, d_{mean} of the reference alloy (Ref) shows a steady increase between 900 and 1300 °C. For MA1, MA2, and MA3, the Ti content increases from 20 to 180 ppm and an unsteady behavior for d_{mean} can be observed between 1000 and 1100 °C.

To further investigate this unsteady behavior in more detail, LOM images of the quenched samples were made. **Figure 4** shows the LOM images of the polished and etched samples of MA2 after annealing temperatures between 900 and 1100 °C. For better visualization, the PAGBs were redrawn and the software Adobe Fresco was used for this. Figure 4a depicts the PAGB after a T_a of 900 °C and b) after a T_a of 1000 °C and both cases show uniform grain growth of the PAGB. Abnormal grain growth can be seen in Figure 4c after T_a of 1050 °C. After T_a of 1100 °C, uniform grain growth of the PAGB can be observed again in Figure 4d.

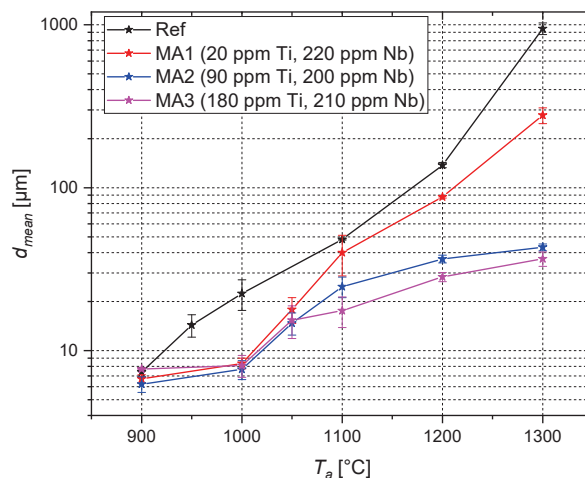


Figure 3. Mean size of the PAG (d_{mean}) after various T_a for the investigated alloys. In the logarithmic scale, Ref shows a linear behavior, while MA1–MA3 shows a jump in the grain size behavior between 1000 and 1100 °C.

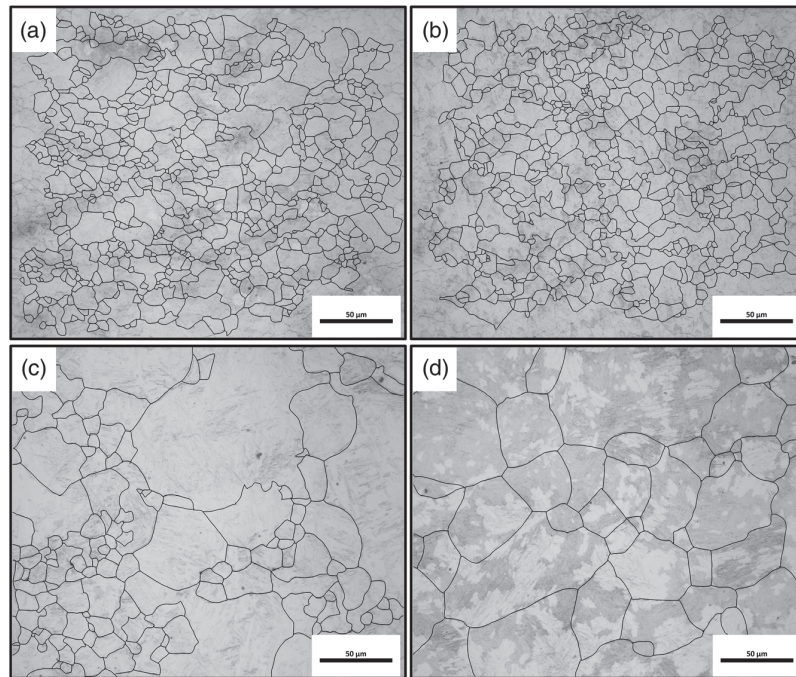


Figure 4. LOM images of the grain size evolution of MA2 after different T_a : a) 900 °C, b) 1000 °C, c) 1050 °C, and d) 1100 °C.

3.2. Double-Hit Experiments

The recrystallization curves determined by double-hit experiments are presented in **Figure 5**. The T_a was 1200 °C and T_{def} was 850 °C for all experiments. The results for the reference alloy (Ref) show an Avrami-like behavior and no plateau is present in the recrystallization curve. Adding Ti and Nb shifts all

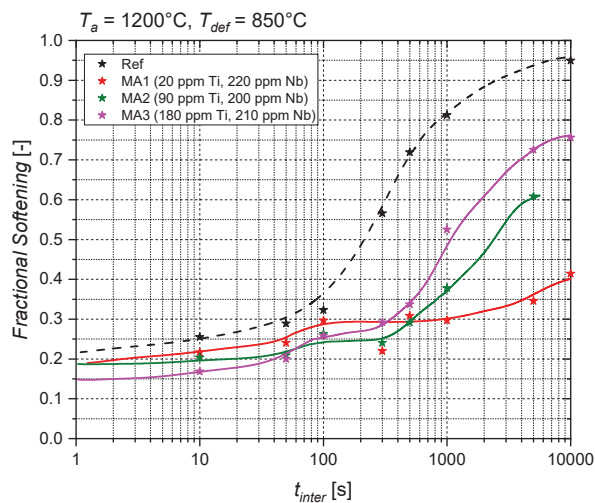


Figure 5. Recrystallization degree, respectively, fractional softening, determined using double-hit experiments and using the 5% true strain method. For all alloys, T_a was 1200 °C and T_{def} was 850 °C.

recrystallization curves to longer times and leads to the formation of a plateau in the recrystallization behaviors. The plateau is most pronounced for MA1 and can be found between a t_{inter} of 100 and 1000 s. For MA2 and MA3, the plateau is present between 100 and 300 s.

3.3. Microstructural Characterization

The results of the double-hit experiments suggest that the formation of strain-induced precipitates starts at a t_{inter} of around 100 s, as this is shown by the formation of plateaus in the recrystallization curves for all three microalloyed steels. To characterize these postulated precipitates, APT measurements were carried out on deformed and quenched samples after a t_{inter} of 300 s. **Figure 6** shows 3D reconstructions of a representative APT measurements of each of the three microalloyed steels after a t_{inter} of 300 s. In the reconstructions in **Figure 6**, Nb and C atoms are highlighted with orange and purple dots, respectively. In each alloy, precipitates were found with different sizes. **Figure 6a,c** shows clusters of Nb atoms with a size around 5 to 10 nm, whereas **Figure 6b** shows a Nb cluster with a size of around 40 nm. For better visualization in **Figure 6a,c**, the Nb clusters are highlighted with isosurfaces corresponding to Nb concentration of 1 at%.

For analyzing the chemical composition of the precipitates, a 1D concentration profile was created by placing a virtual cylinder through the precipitates in the 3D reconstructions. **Figure 7a** shows a typical 1D concentration profile of a 5–10 nm small Nb(C,N) precipitate. Besides Nb, C, and N, the particle also contains small amounts of Mo and Cr. The chemical composition of a precipitate with a bigger size of around 40 nm, an example of which is

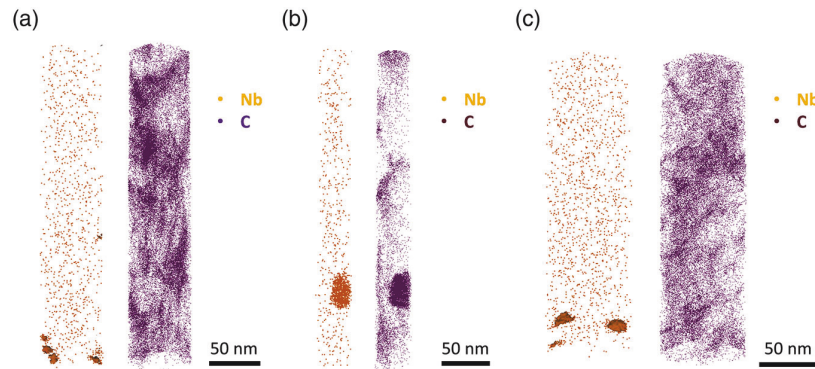


Figure 6. 3D reconstructions of representative APT measurements of compressed and quenched samples after a t_{inter} of 300 s for a) MA1, b) MA2, and c) MA3.

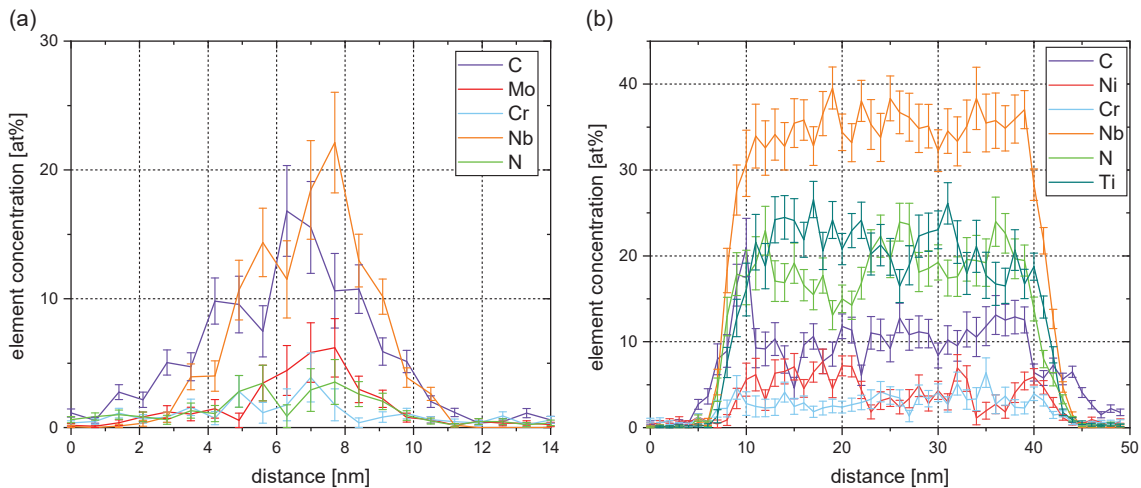


Figure 7. 1D concentration profile of a) 5–10 nm small Nb(C,N) precipitate and b) 40 nm small (Nb,Ti)(C,N) precipitate.

depicted in Figure 6b, is shown in Figure 7b. The particle mainly consists of Nb, Ti, C, and N with small amounts of Cr and Ni.

As described earlier, Nb is often found in (Ti,Nb)(C,N) precipitates and is therefore less present in a dissolved state in the matrix. To investigate the influence of the Ti content of the alloy on the concentration of Nb in solute solution in the matrix, the chemical compositions of the matrix in deformed samples were determined after a t_{inter} of 300 s. For this, only areas that did not include precipitates were used for determination.

An overview of the results for Nb concentration in the matrix is shown in Figure 8. It can be seen that the Nb concentration in the matrix decreases with increasing Ti content in the alloys. In MA1, the average Nb concentration in solute solution is about 0.0090 at%, whereas the value decreases for MA2 and MA3 to 0.0070 at% and 0.0050 at%, respectively.

4. Discussion

The aim of this work was to investigate the influence of different Ti contents on the recrystallization and grain growth behavior

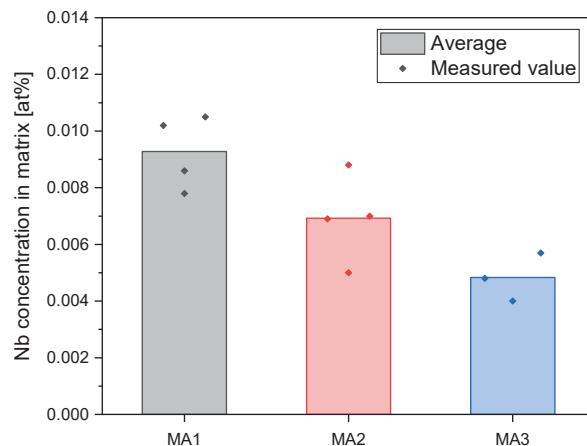


Figure 8. Graphical visualization of the Nb concentration in solute solution in the matrix after the double-hit experiments after a t_{inter} of 300 s for all three microalloyed steels.

of a HSLA steel microalloyed with Nb and a C content above 0.2 wt%. Therefore, alloys with a constant Nb content of around 200 ppm, but a varying Ti content between 20 and 180 ppm were produced. To investigate the influence of both microalloying elements, a microalloy-free reference alloy (Ref) was produced as well. For the determination of the grain growth behavior, annealing experiments were carried out and their results are depicted in Figure 3.

The absence of Nb and Ti in Ref explains the steady increase of d_{mean} over T_a in Figure 3. The microalloying elements would result in a deviation of the linear grain growth behavior in the logarithmic scale due to the solute drag effect and the pinning effect through precipitates. On the one hand, in a precipitate-free microalloyed steel, the solute drag effect would lead to a sharp increase in grain growth once a critical temperature is reached.^[14] If, on the other hand, there are microalloyed precipitates in the matrix, there is a sudden increase in grain growth accompanied with abnormal grain growth, when a certain critical temperature is reached.^[15] According to Moon et al.,^[16] the grain growth depends on a critical precipitate size (r_{cr}) and temperature. r_{cr} can be determined as follows.

$$r_{\text{cr}} = \frac{2\gamma V_m}{RT} \left(\ln \left(\frac{C_m}{C_\infty} \right) \right)^{-1} \quad (1)$$

where γ is the interfacial energy between the particle and the matrix, V_m is the molar volume of the precipitates, T is the temperature, R is the universal gas constant, and C_m and C_∞ are the nominal concentration and the equilibrium concentration of solute atoms in the matrix, respectively. At a given temperature, particles with a size $r > r_{\text{cr}}$ become coarser, whereas particles with a size $r < r_{\text{cr}}$ dissolve. As a result, the precipitates that inhibit grain coarsening dissolve in the matrix and abnormal grain growth occurs in these areas. Such a behavior is visible for MA2 in Figure 4c where large grains grow locally within the microstructure at T_a of 1050 °C. Abnormal grain growth can also be observed for MA1 and MA3 in this temperature range. This can also be seen in the sudden increase of d_{mean} for MA1, MA2 and MA3 in Figure 3. Both MA2 and MA3 are alloyed with Nb and Ti, whereas MA1 is only alloyed additionally with Nb. As all three microalloyed steels show abnormal grain growth in the same temperature range, it is attributed to the dissolution of Nb(C,N) precipitates. Abnormal grain growth was found in the same temperature range in a steel alloyed with Ti and Nb by Karmakar et al.^[17] and was also ascribed to the dissolution of Nb(C,N).

Figure 3 also reveals that there are hardly any differences in grain growth between MA2 and MA3 over the entire temperature range. Even at high T_a of 1300 °C, the difference in d_{mean} is small compared with MA1. The d_{mean} for MA1 at this temperature is 278.7 μm and for MA2 and MA3 43.1 μm and 36.7 μm, respectively. The smaller increase in d_{mean} over T_a for MA2 and MA3 compared with MA1 is due to the addition of Ti. The equilibrium solubility temperature of TiN is around 1400 °C in most Ti-alloyed HSLA steels and is therefore added to HSLA steels to inhibit grain growth at a high T_a . In the present study, with regard to inhibiting grain coarsening, it makes only little difference in d_{mean} whether 90 ppm Ti, as in MA2, or 180 ppm Ti, as in MA3, are added. To be able to explain in detail why this is the

case, further investigations would be necessary. Most likely it is due to a similar number of precipitates, which have the required size for pinning the grain boundaries.

For a precipitation-free C–Mn steel, the static recrystallization behavior can be described with an Avrami-type equation.^[18]

$$X_a = 1 - \exp \left[-0.693 \left(\frac{t}{t_{0.5}} \right)^n \right] \quad (2)$$

where X_a is the recrystallized fraction depending on the time t , n is a constant, and $t_{0.5}$ is the time, when half of the volume is recrystallized. The static recrystallization behavior of Ref is depicted in Figure 5 and can be described with Equation (2), as in this steel no precipitates are formed during the double-hit deformation experiment. Due to the addition of Nb in MA1 and Nb and Ti in MA2 and MA3, the recrystallization behavior of these microalloyed steels shows the formation of a plateau in Figure 5. In the past, it could be shown that the formation of these plateaus is caused by the formation of strain-induced Nb(C,N) precipitates.^[12,19] In the present study, such 5–10 nm small precipitates were found in the 3D reconstructions of APT measurements in Figure 6a,c of deformed samples after a t_{inter} of 300 s. The analysis of the chemical composition (Figure 7a) revealed that the precipitates mainly consist of Nb and C, with small additions of Cr, Mo, and N. A bigger precipitate with a size of around 40 nm was found in the 3D reconstruction in Figure 6b. The chemical analysis of this precipitate revealed that in this case it is a (Nb,Ti)(C,N) particle with small amounts of Cr and Ni. The authors^[12] could show in a previous work that the small Nb(C,N) precipitates are formed strain-induced after deformation, which they were able to show in a similar steel under similar experiment conditions. In contrast, bigger (Nb,Ti)(C,N) precipitates, an example of which is seen in Figure 6b, can already be found in the as-rolled condition, which was also shown in the aforementioned study.^[12]

As mentioned earlier, the results of the annealing experiments showed that there is only little difference in d_{mean} whether 90 ppm Ti, as in MA2, or 180 ppm Ti, as in MA3, are added to the steel. However, a different trend was observed for the static recrystallization behavior in Figure 5. In the present case, the recrystallization was inhibited with a decreasing amount of Ti in the alloy. This means that the degree of fractional softening decreased with a decreasing Ti content in the steel, especially at higher $t_{\text{inter}} > 1000$ s. Upon all microalloying elements, Nb has the strongest recrystallization-inhibiting properties.^[2] The results of this work suggest that with an increasing Ti content, less Nb is in solute solution in the matrix and therefore not available for the formation of strain-induced Nb(C,N) precipitates. To prove this assumption, the chemical composition of the matrix of deformed samples after a t_{inter} of 300 s was analyzed using APT. The results of the measurements are illustrated in Figure 8 and confirm the assumption that with an increasing Ti content in the steel, the Nb concentration in the matrix decreases. As a consequence, the recrystallization inhibiting effects of Nb(C,N) are mostly pronounced in MA1, as there is almost no Ti alloyed to the steel. For the same reason, the plateau is also most pronounced between a t_{inter} of 100 and 1000 s for MA1, whereas the plateau is only present between a t_{inter} of 100 and 300 s for MA2 and MA3.

On the one hand, the addition of Ti in HSLA steels microalloyed with Nb is important to minimize the grain coarsening at elevated temperatures, whereby the annealing experiments revealed that in the present case it made no difference whether the Ti content was 90 or 180 ppm. On the other hand, less Nb is available for the formation of strain-induced Nb(C,N) precipitates with an increasing Ti content in the steel due to the formation of (Ti,Nb)(C,N) precipitates. Therefore, with regard to the Ti content, neither too low nor too high a concentration should be chosen. This enables certain stability against grain coarsening at elevated temperatures and at the same time allows the positive effects of TMCP to be used in HSLA steels with C contents above 0.2 wt%.

5. Conclusion

In this study three microalloyed steels (MA1, MA2, and MA3) and one microalloy-free reference steel (Ref) were investigated. The three microalloyed steels have a C content of 0.23 wt%, a Nb content of around 200 ppm, and varying Ti contents between 20 and 180 ppm. The aim of this work was to investigate the influence of the Ti content in steels microalloyed with Nb on grain growth and recrystallization behavior and to compare it with a microalloy-free reference steel. Annealing experiments with various annealing temperatures were carried out to analyze the grain growth behavior of the alloys. The static recrystallization behavior was analyzed using double-hit deformation experiments. The results of this work allow to draw the following conclusions: 1) The grain growth behavior of Ref does not show an unsteady behavior due to the absence of a dissolution of precipitates; 2) The grain growth at elevated temperatures was inhibited in all microalloyed steels compared with Ref and shows a sudden increase at a temperature around 1050 °C, which is attributed to abnormal grain growth resulting from the dissolution of Nb(C,N) precipitates; 3) The grain growth behavior of MA2 and MA3 was inhibited compared with MA1 due to higher amounts of Ti. TiN and (Nb,Ti)(C,N) precipitates were responsible for the pinning of the grains at elevated temperatures. The results of the present work show that there is only little difference in the grain growth behavior, whether the Ti content is 90 or 180 ppm; 4) The static recrystallization behavior of Ref was investigated using double-hit deformation experiments and shows an Avrami-like curve, which is attributed to the absence of strain-induced carbide formation; 5) The static recrystallization behavior for MA1, MA2, and MA3 is inhibited compared with Ref. The recrystallization curves of all microalloyed steels show the formation of a plateau starting at a t_{inter} of 100 s, whereas MA1 shows the most pronounced plateau up to 1000 s. The occurrence of the plateau is attributed to the formation of strain-induced Nb(C,N) particles with a size of around 5–10 nm which also contains small amounts of Mo and Cr; 6) The degree of fractional softening above a t_{inter} of 1000 s increased with increasing Ti content of the steel. Due to the higher Ti content, less Nb was available for the formation of strain-induced Nb(C,N) precipitates due to the presence of (Ti,Nb)(C,N) precipitates. These fine Nb(C,N) precipitates are responsible for inhibiting recrystallization, which is why the

degree of recrystallization (fractional softening) is higher in alloys with more Ti; and 7) On the one hand, Ti is needed to prevent grain coarsening at elevated temperatures, but on the other hand, with increasing Ti content, less Nb is available in the matrix for the formation of strain-induced Nb(C,N) precipitates. As a consequence, a right balance must be found when choosing the Ti content in Nb and Ti microalloyed HSLA steels to simultaneously obtain the positive effects of Ti against grain coarsening and the positive effects of Nb on the static recrystallization behavior in HSLA steels with a C content of 0.23 wt%.

Acknowledgements

This research was funded by Austrian BMK (846933) in the framework of the programs "Production of the future" and the "BMK Professorship for Industry"; Österreichische Forschungsförderungs GmbH (FFG:885187); and Österreichische Forschungsförderungs GmbH (FFG:873200).

Conflict of Interest

The authors declare no conflict of interest.

Data Availability Statement

Research data are not shared.

Keywords

atom probe tomography, grain coarsening, high-strength low-alloy steels, Nb microalloyed steels, Ti microalloyed steels, static recrystallizations

Received: February 3, 2022

Revised: March 11, 2022

Published online:

- [1] A. J. DeArdo, M. J. Hua, K. G. Cho, C. I. Garcia, *Mater. Sci. Technol.* **2009**, 25, 1074.
- [2] S. Vervynck, K. Verbeken, B. Lopez, J. J. Jonas, *Int. Mater. Rev.* **2012**, 57, 187.
- [3] D. Chakrabarti, M. Strangwood, C. Davis, *Metall. Mater. Trans. A* **2009**, 40, 780.
- [4] T. N. Baker, *Ironmaking Steelmaking* **2019**, 46, 1.
- [5] A. J. DeArdo, *Int. Mater. Rev.* **2003**, 48, 371.
- [6] a) B. Dutta, C. M. Sellars, *Mater. Sci. Technol.* **1987**, 3, 197; b) C. Klinkenberg, K. Hulka, W. Bleck, *Steel Res. Int.* **2004**, 75, 744.
- [7] C. N. Homsher, *Determination of the Non-Recrystallization Temperature (TNR) in Multiple Microalloyed Steels*, Colorado School of Mines Golden / Colorado, USA **2013**.
- [8] S. G. Hong, K. B. Kang, C. G. Park, *Scr. Mater.* **2002**, 46, 163.
- [9] J. Webel, A. Herges, D. Britz, E. Detemple, V. Flaxa, H. Mohrbacher, F. Mücklich, *Metals* **2020**, 10, 243.
- [10] A. Hegetschweiler, O. Borovinskaya, T. Staudt, T. Kraus, *Anal. Chem.* **2019**, 91, 943.
- [11] G. Gottstein, *Physikalische Grundlagen der Materialkunde*, Springer-Verlag Berlin Heidelberg, Berlin, Heidelberg **2007**.

- [12] S. Monschein, M. Kapp, D. Zügner, J. Fasching, A. Landefeld, R. Schnitzer, *Steel Res. Int.* **2021**, 92, 2100065.
- [13] *Atom Probe Tomography: Put Theory into Practice* (Ed: W. Lefebvre-Ulrikson), Academic Press, London **2016**.
- [14] Q. Yu, Y. Sun, *Mater. Sci. Eng., A* **2006**, 420, 34.
- [15] L. J. Cuddy, J. C. Raley, *Metall. Trans. A* **1983**, 14A, 1989.
- [16] J. Moon, C. Lee, S. Uhm, J. Lee, *Acta Mater.* **2006**, 54, 1053.
- [17] A. Karmakar, S. Kundu, S. Roy, S. Neogy, D. Srivastava, D. Chakrabarti, *Mater. Sci. Technol.* **2014**, 30, 653.
- [18] S. F. Medina, V. Lopez, *ISIJ Int.* **1993**, 33, 605.
- [19] a) S. F. Medina, J. E. Mancilla, *ISIJ Int.* **1993**, 33, 1257;
b) S. F. Medina, J. E. Mancilla, *Acta Metall. Mater.* **1994**, 42, 3945; c) R. Esterl, M. Sonnleitner, R. Schnitzer, *Steel Res. Int.* **2019**, 90, 1800500.

Paper IV

Stefan Monschein, Katharina S. Ragger, Josef Fasching, Dominik Zügner and Ronald Schnitzer

Microstructural, Chemical and Crystallographic Investigations of Dynamic Strain-Induced Ferrite in a Microalloyed QT Steel

Metals 2022, 12, 313;

DOI: 10.3390/met12020313

Article

Microstructural, Chemical, and Crystallographic Investigations of Dynamic Strain-Induced Ferrite in a Microalloyed QT Steel

Stefan Monschein ^{1,*}, Katharina S. Ragger ², Josef Fasching ³, Dominik Zügner ⁴ and Ronald Schnitzer ¹

¹ Department of Materials Science, Montanuniversität Leoben, Franz Josef-Straße 18, 8700 Leoben, Austria; ronald.schnitzer@unileoben.ac.at

² Voestalpine Wire Rod Austria GmbH, Drahtstraße 1, 8792 St. Peter-Freienstein, Austria; katharina.ragger@voestalpine.com

³ Voestalpine Stahl Donawitz GmbH, Kerpelystraße 199, 8700 Leoben, Austria; josef.fasching@voestalpine.com

⁴ Voestalpine Forschungsservicegesellschaft Donawitz GmbH, Kerpelystraße 199, 8700 Leoben, Austria; dominik.zuegner@voestalpine.com

* Correspondence: stefan.monschein@unileoben.ac.at



Citation: Monschein, S.; Ragger, K.S.; Fasching, J.; Zügner, D.; Schnitzer, R. Microstructural, Chemical, and Crystallographic Investigations of Dynamic Strain-Induced Ferrite in a Microalloyed QT Steel. *Metals* **2022**, *12*, 313. <https://doi.org/10.3390/met12020313>

Academic Editor: Angelo Fernando Padilha

Received: 10 January 2022

Accepted: 8 February 2022

Published: 10 February 2022

Publisher's Note: MDPI stays neutral with regard to jurisdictional claims in published maps and institutional affiliations.



Copyright: © 2022 by the authors. Licensee MDPI, Basel, Switzerland. This article is an open access article distributed under the terms and conditions of the Creative Commons Attribution (CC BY) license (<https://creativecommons.org/licenses/by/4.0/>).

Abstract: Dynamic strain-induced transformation (DSIT) enables the formation of fine-grained ferritic microstructures, which are well suited for cold forming processes in the as-rolled condition. In this work, the formation mechanism, chemical composition, and crystallographic orientation of DSIT ferrite were investigated in a micro-alloyed steel and compared to pre-eutectoid ferrite. High-resolution techniques, such as scanning transmission electron microscopy and atom probe tomography (APT), were used for the investigations. To generate DSIT ferrite and pre-eutectoid ferrite, different experimental routes were applied using a compression deformation dilatometer. The results show a large number of NbC precipitates within DSIT ferrite, and show that the formation of DSIT ferrite is accompanied with C diffusion and the formation of retained austenite. APT measurements revealed that the C- and Mn concentration in DSIT ferrite is higher compared to pre-eutectoid ferrite. The crystallographic orientation of DSIT ferrite was examined using electron backscatter diffraction. The crystallographic orientation of DSIT ferrite after the deformation route revealed that the $\langle 111 \rangle$ plane normals are parallel to the compression direction with the $\langle 110 \rangle$ directions pointing towards the radial direction of the compressed sample. The results suggest that the formation of DSIT ferrite is a displacive mechanism, accompanied by C diffusion.

Keywords: dynamic strain-induced ferrite; thermomechanical processing; micro-alloyed steel; atom probe tomography; electron backscatter diffraction

1. Introduction

Quenched and tempered (QT) steels are characterized by a good toughness with a high hardness and strength. The final properties are achieved after quenching from the austenitic phase field and a subsequent tempering process. In order to ensure good cold formability, the microstructure of the semi-finished parts must meet certain properties before quenching and tempering. In most cases, the optimal cold forming properties of semi-finished QT steels are achieved after a soft annealing process prior to the forming process. In order to avoid this cost-intensive annealing step, micro-alloyed and thermo-mechanical controlled (TMC) processed QT steels have emerged as an alternative. The underlying idea is based on the good formability of fine ferritic microstructures, which can be adjusted using TMC processes and the addition of microalloying elements such as Nb and Ti [1]. A specific form of TMC processing is the formation of ferrite by dynamic strain-induced transformation (DSIT) [2–4]. This ferrite formation takes place dynamically during the deformation between A_{e3} (equilibrium temperature of the austenite to ferrite transformation) and A_{r3} (transformation temperature from austenite to ferrite, depending on the cooling rate) and differs from the dynamic transformation (DT) above A_{e3} that

Priestner et al. [5] observed already in the early 1980s. Yada et al. [6] were among the first to provide direct evidence of the dynamic formation of ferrite from an austenitic microstructure using in-situ X-ray diffraction. For the onset of the DSIT ferrite formation, a critical strain ($\epsilon_{C,DSIT}$) is required, which can be determined either by metallographic methods after quenching the deformed microstructure or indirectly by using the double-differentiation method developed by Poliak and Jonas [7,8]. The latter method was originally developed to determine the critical strain for the onset of dynamic recrystallization (DRX). However, it has shown that the underlying principle is the same for DRX and DSIT, as in both cases the softening affects the work hardening behavior of the deformed materials [9,10]. Thanks to the formation process of DSIT ferrite, it is possible to produce fine equiaxed ferrite grains with a grain size in the range of a few μm . Beladi et al. [11] have shown that the formation of DSIT ferrite initially occurs along the prior austenite grain boundaries (PAGB), followed by intragranular nucleation. It has also been reported that the presence of deformation bands [12] and fine NbC precipitates [13] enhances the amount of DSIT ferrite. During the formation process of DSIT ferrite, dynamic recrystallization and thus further grain refinement takes place. A misorientation of the low-angle grain boundaries that leads to a gradual transformation to high-angle grain boundaries is responsible for this, and therefore to a decreasing ferrite grain size [4,14,15].

Although the formation of DSIT ferrite has been well studied in the past, there are still open points regarding its mechanism of formation. Studies suggest that the formation of DSIT ferrite is more of a diffusional transformation process than a displacive mechanism [2,11]. Previous simulations by Zheng et al. [16] and experimental results by Hao et al. [17] show that the formation of DSIT ferrite is accompanied by C diffusion. As reported by Hao et al. [17], dislocations and deformation bands can serve as rapid diffusion channels. Nevertheless, C can only insufficiently diffuse due to the short time, which can lead to C supersaturated ferrite, or the formation of ultrafine cementite particles within ferrite. Hurley et al. [18] were able to show a Kurdjumov–Sachs orientation between the prior austenite grain and DSIT ferrite. This, in turn, would indicate a displacive mechanism.

In this study, the formation mechanism, chemical composition, and crystallographic orientation of DSIT ferrite were investigated and compared to pre-eutectoid formed ferrite in a QT steel. Therefore, various compression tests were performed with a deformation dilatometer in order to produce DSIT ferrite on the one hand and pre-eutectoid ferrite on the other. High resolution techniques, such as scanning transmission electron microscopy (STEM) in a scanning electron microscope (SEM), atom probe tomography (APT), and electron backscatter diffraction (EBSD) are used to provide insight into the microstructure, the chemical composition, and the crystallographic orientation of the ferritic areas.

2. Materials and Methods

2.1. Investigated Material

The chemical composition of the investigated steel is given in Table 1.

Table 1. Chemical composition of the investigated steel.

	Fe	C	N	Mn	Si	Cr	B	Nb	Ti
wt.%	bal.	0.32	0.004	0.98	0.10	0.43	0.0020	0.0110	0.0220
at.%	bal.	1.45	0.016	0.98	0.19	0.46	0.0100	0.0060	0.0250

The C content was selected in such a way that a sufficiently high strength for the finished components can be guaranteed after quenching and tempering. Ti was added to inhibit the grain growth during annealing. On the one hand, Nb was added to inhibit recrystallization through the formation of strain-induced NbC precipitates during TMC processing and, on the other hand, to support the formation of DSIT ferrite through NbC precipitates. The addition of small amounts of B improves the hardenability of the steel.

The steel was produced by vacuum induction melting. After reheating to 1100 °C, the ingot was rolled to a sheet thickness of 15 mm with a finish rolling temperature of 900 °C.

2.2. Dilatometric Experiments

The size of the dilatometer samples was 5 mm in diameter and 10 mm in length, with the longitudinal direction of the dilatometer sample oriented in the rolling direction of the sheet. To control the temperature during the processing a type S thermocouple was spot welded onto the surface of the sample.

2.2.1. Determination of A_{e1} , A_{e3} , and A_{r3}

The measurements of the transformation temperatures A_{e1} , A_{e3} , and A_{r3} were done by using a quenching dilatometer (DIL 805, TA Instruments, Hüllhorst, Germany). To determine A_{e1} and A_{e3} , measurements according to the ASTM A 1033-04 standard were carried out. To measure A_{r3} , the samples were heated to an annealing temperature (T_a) 50 °C above A_{e3} with a heating rate of 10 °Cs⁻¹. After a holding step (t_a) of 300 s the samples were cooled down to room temperature with cooling rates (λ) of -0.1, -0.3, -1.0, and -3.0 °Cs⁻¹.

2.2.2. Compression Experiments

In order to create DSIT ferrite and pre-eutectoid ferrite, three different compression routes were carried out with a deformation dilatometer (DIL 805 A/D/T, TA Instruments, Hüllhorst, Germany). A schematic drawing of the time–temperature–deformation schedule is shown in Figure 1.

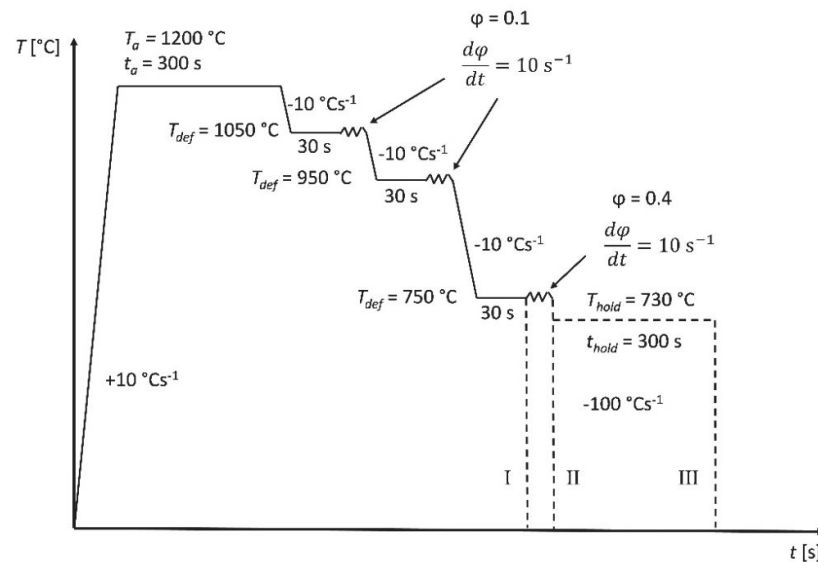


Figure 1. Schematic drawing of the time-temperature-deformation schedule. To investigate the dynamic strain-induced transformation (DSIT) and pre-eutectoid ferrite, three different deformation routes were carried out.

In all routes, the samples were initially heated with a heating rate of 10 °Cs⁻¹ to a T_a of 1200 °C and were held for 300 s. An equilibrium solubility temperature of 1165 °C was calculated for Nb(C,N) using the equation from Irvine et al. [19]. Therefore, the T_a was chosen in a way that Nb precipitates inside the matrix dissolved within the 300 s annealing time. After that, two compression steps were carried out with $\phi = 0.1$ and a strain rate of 10 s⁻¹ at deformation temperatures (T_{def}) of 1050 °C and 950 °C, respectively. The samples were cooled to T_{def} with a cooling rate of -10 °Cs⁻¹ and held at a constant temperature for 30 s before compression. In route I, the sample was cooled to $T_{def} = 750$ °C with a cooling

rate of $-10\text{ }^{\circ}\text{Cs}^{-1}$ and held for 30 s. To clarify whether the ferrite formation was due to DSIT or whether the formation was pre-eutectoid, the sample was directly gas quenched. In route II, after the holding time of 30 s the sample was compressed with $\varphi = 0.4$ at a strain rate of 10 s^{-1} . The sample was then also gas quenched to room temperature with a cooling rate of $-100\text{ }^{\circ}\text{Cs}^{-1}$. In order to investigate the properties of pre-eutectoid ferrite in the equilibrium state, route III was chosen. After the final compression step in route III, the sample was cooled to $T_{hold} = 730\text{ }^{\circ}\text{C}$ with a cooling rate of $-10\text{ }^{\circ}\text{Cs}^{-1}$ and was held constant for $t_{hold} = 300\text{ s}$. T_{hold} was chosen in a way that the temperature was still in the austenite/ferrite two-phase region. This sample was then also directly gas quenched to room temperature with a cooling rate of $-100\text{ }^{\circ}\text{Cs}^{-1}$. Silicon nitride tools were used for the uniaxial compression of the material.

2.3. Microstructural and Crystallographic Characterization

The microstructure in the deformed and quenched condition was examined with light optical microscopy (LOM) (Axio Imager M1m, Zeiss, Oberkochen, Germany) and SEM. Therefore, the samples were ground with SiC paper, polished with a $1\text{ }\mu\text{m}$ diamond suspension, and etched with a 3% nital etchant. In addition, high resolution images of DSIT ferrite were made using STEM. The thin-foil STEM specimens were prepared by polishing with SiC paper, subsequently followed by a thinning step in a double-jet electropolishing device (Tenupol 5, Struers, Willich, Germany).

The crystallographic orientation of DSIT ferrite after route II was determined using EBSD. Therefore, the polished samples were only lightly etched with a 3% nital etchant and then polished for about 1 min using an OP-U suspension. The data evaluation was carried out with the OIM Analysis 8 software from EDAX.

In order to investigate the chemical composition of ferrite, atom probe tomography (APT) measurements were performed. For this reason, APT tips were site-specific produced from the ferritic areas with a focused ion beam (FIB) microscope [20,21]. The APT measurements were carried out with a LEAP 3000X HR (Cameca, Gennevilliers Cedex, France) in the laser mode, with a pulse frequency of 250 kHz, a base temperature of 40 K, and a laser energy of 60 pJ. The data reconstruction was done with IVAS 3.6.14 software from Cameca. The SEM, STEM, EBSD, and FIB methods were performed using a Versa 3D Dual Beam device (FEI, Hillsboro, OR, USA).

3. Results

3.1. Determination of A_{e1} , A_{e3} and A_{r3}

For A_{e1} and A_{e3} , temperatures of $722\text{ }^{\circ}\text{C}$ and $809\text{ }^{\circ}\text{C}$ were determined, respectively. The results of the measurements for A_{r3} are shown in Table 2. With an increasing λ from $-0.1\text{ }^{\circ}\text{Cs}^{-1}$ to $-3.0\text{ }^{\circ}\text{Cs}^{-1}$, the A_{r3} decreased from $751\text{ }^{\circ}\text{C}$ to $690\text{ }^{\circ}\text{C}$.

Table 2. A_{r3} temperature depending on the cooling rate (λ).

$\lambda\text{ [}^{\circ}\text{Cs}^{-1}\text{]}$	$A_{r3}\text{ [}^{\circ}\text{C}\text{]}$
0.1	751
0.3	728
1.0	717
3.0	690

3.2. Microstructural and Chemical Characterization after the Deformation Experiments

Figure 2 shows LOM and SEM images of the quenched samples after the dilatometer routes I–III in the longitudinal section. Figure 2a,b depicts the microstructure after route I and shows a purely martensitic microstructure. The microstructure after route II is presented in Figure 2c,d. A martensitic matrix and approximately $5\text{ }\mu\text{m}$ small and uniform ferrite grains can be seen in both images. As a purely martensitic microstructure was

observed after route I, this was used as indirect evidence that ferrite formed during the final deformation step of route II, and therefore is DSIT ferrite. A detailed LOM image after route II is presented in Figure 3. Triple points are highlighted with arrows to show the formation of DSIT ferrite along PAGB. In route III, the sample was annealed at a T_{hold} of 730 °C for 300 s. This temperature was just above A_{e1} . Therefore, it can be said that the ferrite shown in Figure 2e,f is pre-eutectoid ferrite, which formed primarily along the PAGB. Furthermore, a comparison of Figure 2c,e shows that the ferrite content in the microstructure has increased between route II and route III.

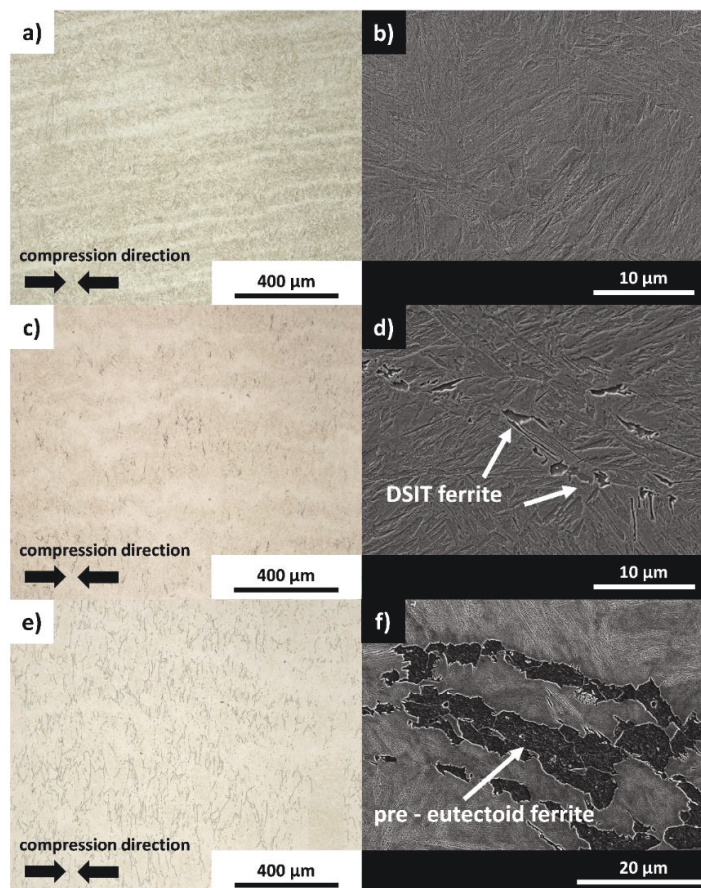


Figure 2. (a,b) Light optical microscopy (LOM) and scanning electron microscopy (SEM) image after route I. (c,d) LOM and SEM image after route II. (e,f) LOM and SEM image after route III.

Figure 4a,b shows STEM images with different magnifications of DSIT ferrite after route II. Both images show few dislocations within the ferrite, but a large amount of small precipitates. For further characterization of the precipitates and the chemical composition of DSIT ferrite after route II, APT measurements were carried out.

Figure 5 shows 3D reconstructions of an APT measurement after route II. The APT tips were produced by a site-specific tip preparation of the DSIT ferrite along the PAGB. In the upper part of the tip in Figure 5a, DSIT ferrite can be seen through the low C concentration, whereas in the lower half, a region with a higher C concentration was measured. Figure 5a,b shows the clustering of Nb and C both in DSIT ferrite and at the interface with the region with the higher C concentration. Figure 5b shows the distribution of B atoms and shows that B segregates in particular at the interface between the two regions.

To investigate the chemical composition of DSIT ferrite and its neighboring area, a chemical depth profile was created along the arrow in the blue cylinder in Figure 6a. The results are shown in Figure 6b, and show that there is an increase of the C content from

0.1 at% inside the DSIT ferrite up to 3.5 at% outside of it. The high C concentration of 3.5 at% compared to the nominal concentration of 1.45 at% indicates that the phase in the lower region of the tip is retained austenite [22].

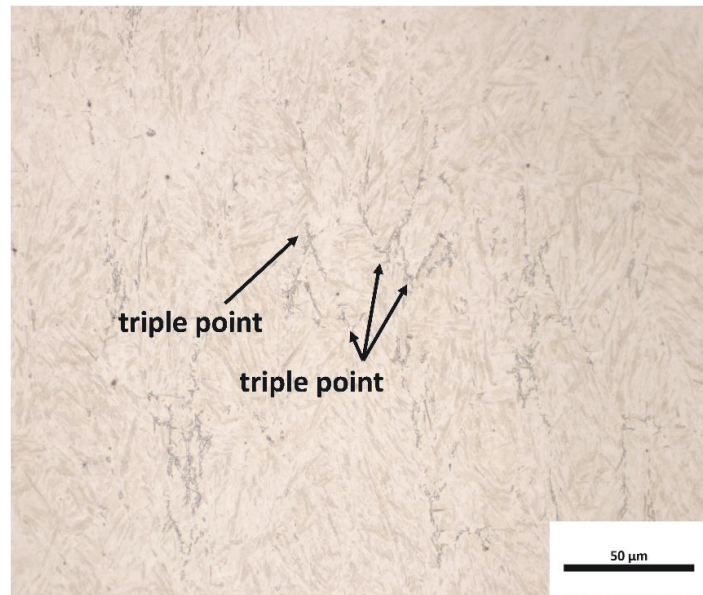


Figure 3. LOM image after route II. Triple points are highlighted with arrows to show the DSIT ferrite along prior austenite grain boundaries (PAGB).

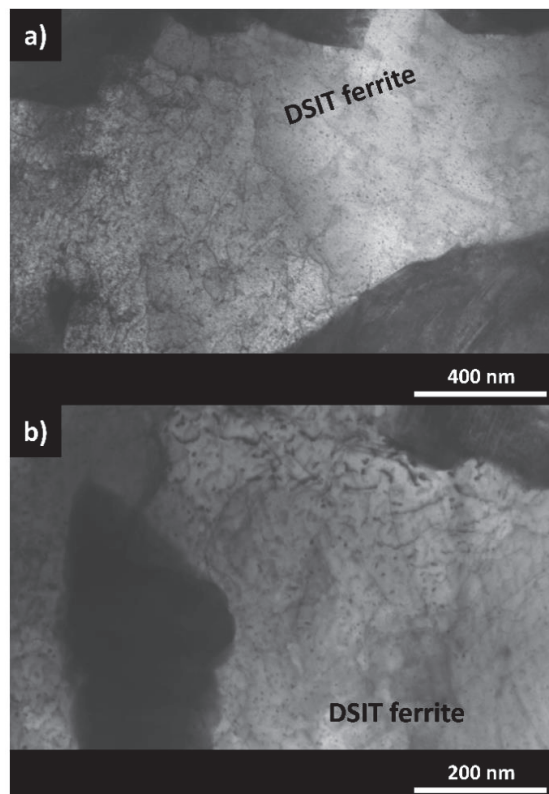


Figure 4. (a,b) Scanning transmission electron microscopy (STEM) images with different magnifications of DSIT ferrite after route II.

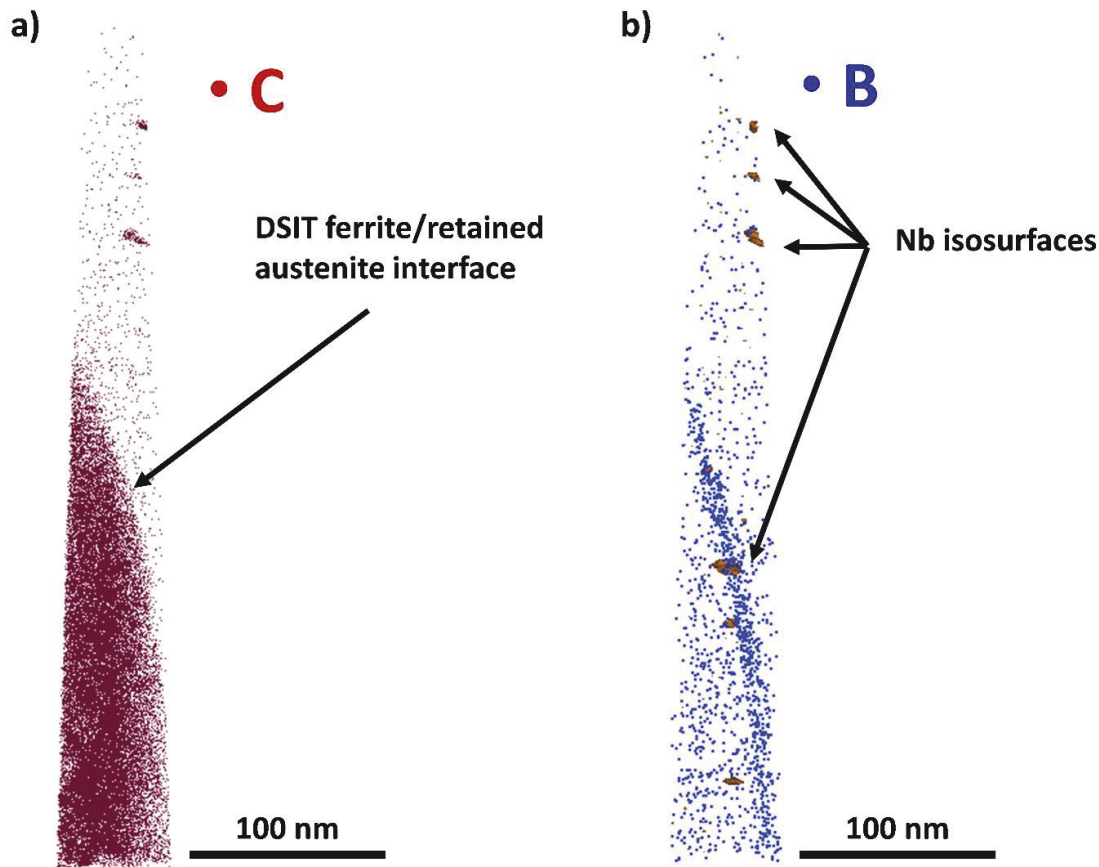


Figure 5. 3D reconstructions of an atom probe tomography (APT) measurement after route II. (a) C atoms are visualized by brown dots. The upper part with the lower number of C atoms represents DSIT ferrite and the lower retained austenite (b) B atoms are visualized by blue dots. The orange Nb isosurface represents the Nb clusters in the DSIT ferrite region and at the interface.

The Cr and Mn concentrations remain constant across the interface around 0.5 at% and 1.0 at%, respectively. Figure 6c shows the chemical depth profile of the red cylinder in Figure 6a. This indicates that this cluster mainly consists next to C and Fe of around 10 at% Nb and 5 at% Cr and Ti.

In order to investigate how the chemical composition of pre-eutectoid ferrite in the equilibrium state differs from the initial composition immediately after the formation of DSIT ferrite, further APT measurements were carried out after route III. Therefore, after route II as well as after route III, three APT tips including DSIT ferrite and pre-eutectoid ferrite, separately, were prepared by using a site-specific FIB-based preparation method. The results of the chemical composition of ferrite after route II and route III are depicted in Figure 7. Figure 7a,b shows that both the C and Mn concentration in ferrite are lower after route III than after route II. For route II, the mean C and Mn concentration is 0.068 at% and 0.980 at%, respectively, whereas the mean C and Mn concentration after route III is decreased to 0.028 at% and 0.864 at%, respectively. No significant differences could be measured for the Cr concentration in the ferrite between route II and route III. In this case, the large scatter of the measured values has to be taken into account.

3.3. Crystallographic Characterization

An EBSD measurement was performed to determine the crystallographic orientation of DSIT ferrite after route II. Therefore, the longitudinal section of a compressed sample after route II was examined. Figure 8a shows the image quality (IQ) map after the EBSD

measurement and the associated inverse pole figure (IPF) map in Figure 8b. From Figure 8a, it can be seen that DSIT ferrite can be distinguished from the martensitic matrix by a lower IQ. This is due to the different etching attacks of the phases during sample preparation. In order to separate the data corresponding to DSIT ferrite from the martensitic matrix, all data points above an IQ threshold were filtered out. The result can be seen for the IQ map in Figure 8c. In order to investigate the crystallographic orientation of DSIT ferrite after route II in the direction of the compression, the data were rotated in the direction of the compression force. The results are shown in Figure 9 and show that a (111)[-110] and (111)[1-10] texture are present. This means that most of the $\langle 111 \rangle$ plane normals are parallel to the compression direction, with the $\langle 110 \rangle$ directions pointing towards the radial direction of the compressed sample.

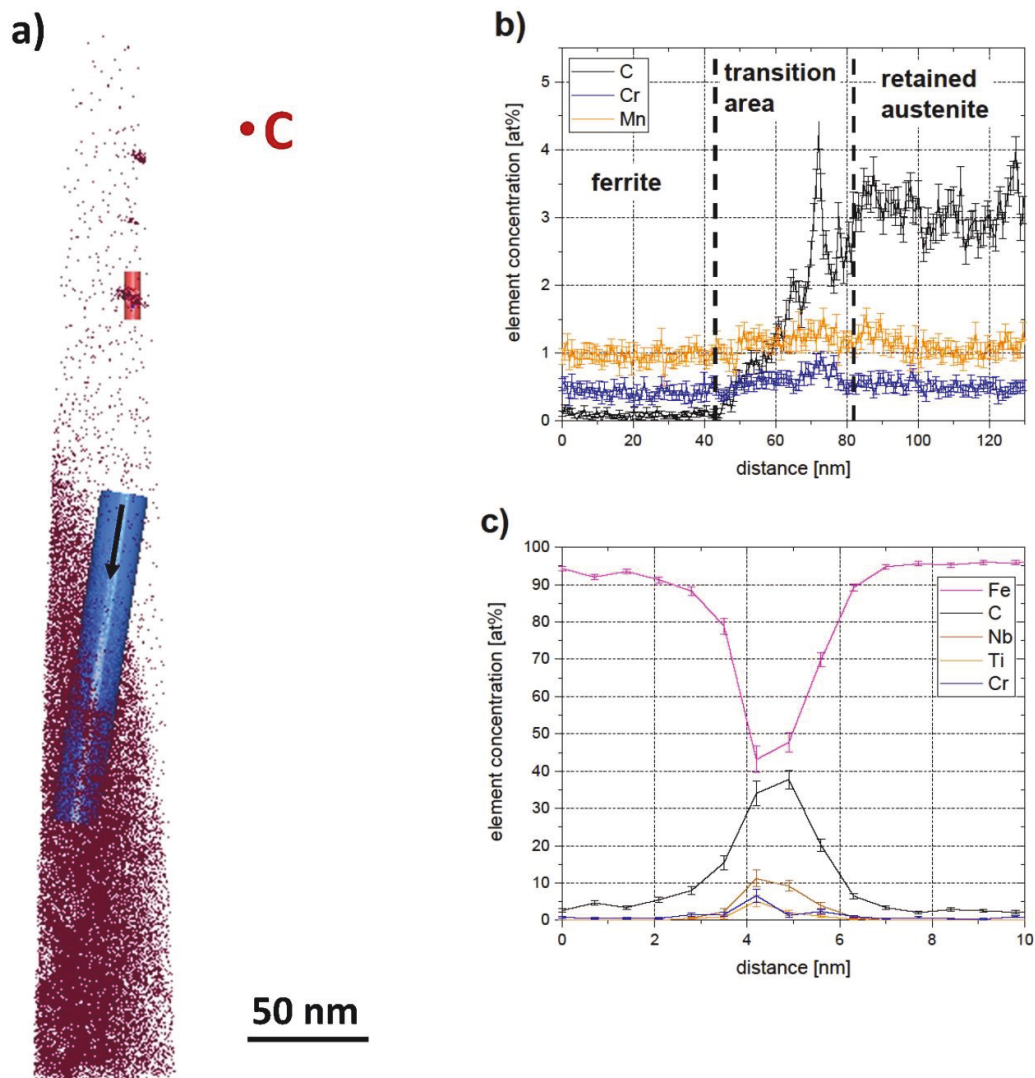


Figure 6. (a) 3D reconstruction of an APT measurement after route II. C atoms are visualized by brown dots. (b) The chemical depth profile across the interface along the arrow in the blue cylinder in (a). (c) The chemical depth profile of a carbide along the red cylinder in (a).

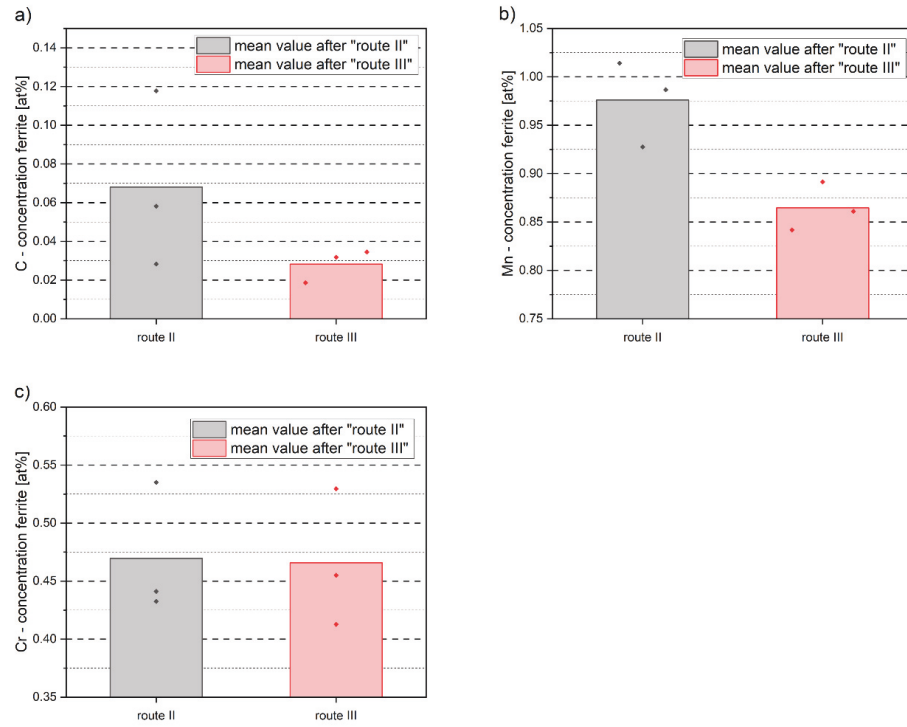


Figure 7. Chemical composition of DSIT ferrite after route II and pre-eutectoid ferrite after route III. (a) C content, (b) Mn content, and (c) Cr content.

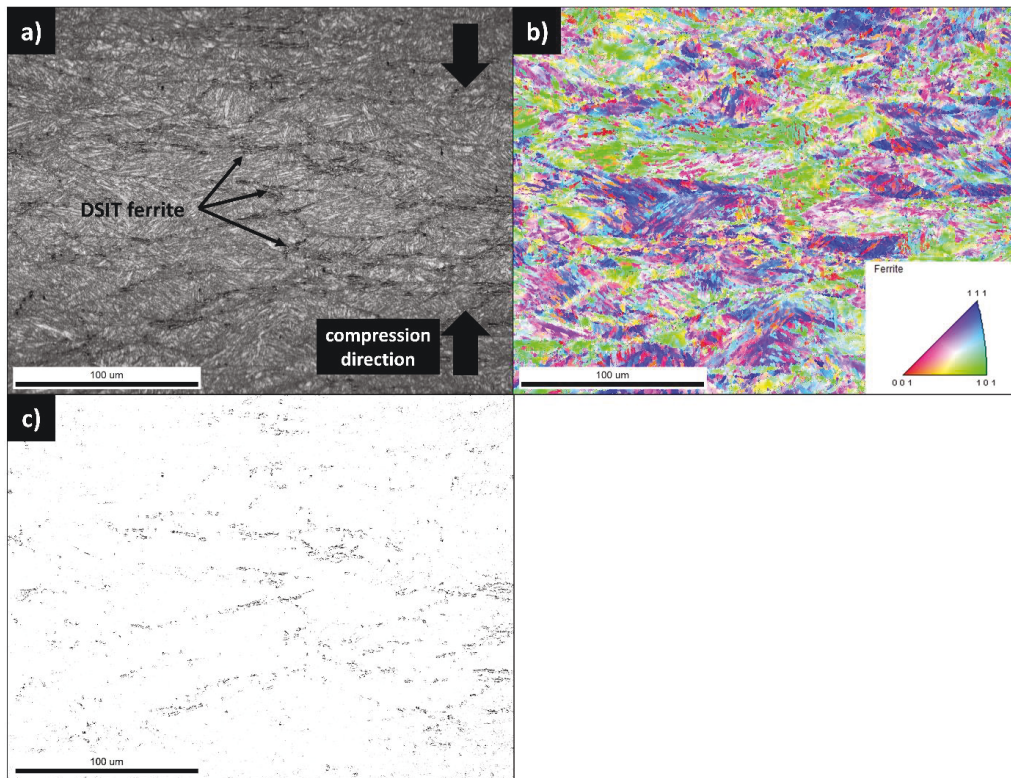


Figure 8. (a) Image quality (IQ) map after an electron backscatter diffraction (EBSD) measurement of a sample after route II in the longitudinal direction. (b) Inverse pole figure (IPF) map after an EBSD measurement of a sample after route II in the longitudinal direction. (c) Reduced IQ map of (a).

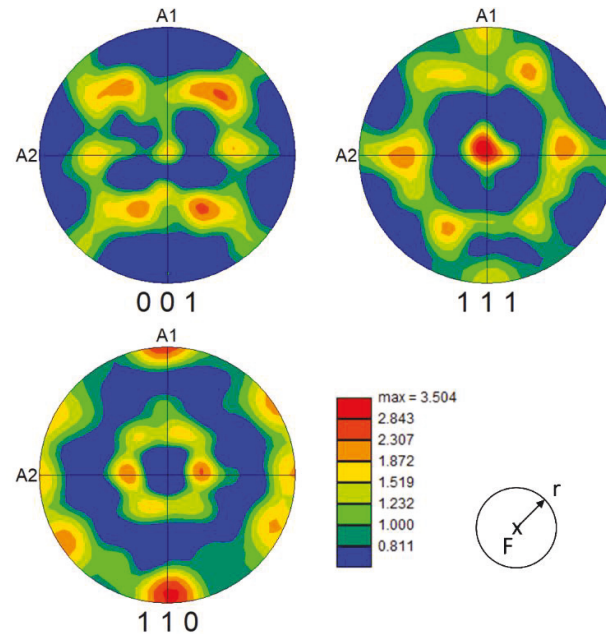


Figure 9. Texture plot of DSIT ferrite in compression direction after route II.

4. Discussion

The aim of this study was to investigate the formation mechanism, the chemical composition, and the crystallographic orientation of DSIT ferrite and to compare it with the properties of pre-eutectoid ferrite. For this reason, compression tests were performed with a deformation dilatometer to produce DSIT ferrite on the one hand, and pre-eutectoid ferrite on the other. Three different compression routes were chosen for this (Figure 1). All three routes had in common that the T_a and the first two compression steps at temperatures of 1050 °C and 950 °C were identical. The aim of the first two compression steps was to introduce deformation into the sample to promote the precipitation of NbC precipitates. In order to create the basic requirement for the formation of DSIT ferrite, the final experiment temperature was chosen in a way that it was between A_{e3} (809 °C) and A_{r3} (690 °C for $\lambda = -3.0 \text{ }^\circ\text{C s}^{-1}$). Therefore, both in route I and route II the samples were cooled to a final temperature of 750 °C, with the difference being that in route I the sample was quenched to room temperature immediately after keeping the temperature constant for 30 s. The LOM and SEM images in Figure 2a,b show that no ferrite formed after route I and that the matrix consists exclusively of martensite. Figure 2c,d shows ferritic areas inside a martensitic matrix after route II. In the present work, this serves as indirect evidence that DSIT ferrite has formed during the last compression step of route II. Sun et al. [23] followed a similar approach when they were able to preserve DSIT ferrite by quenching it directly after the final deformation step. From Figures 3 and 8a,c, it can be seen in more detail that DSIT ferrite, which formed during the last compression step of route II, has grown along PAGB. Similar results were reported in the past by Beladi et al. [11] and Bae et al. [12]. To further characterize pre-eutectoid ferrite, route III was performed. For this reason, the temperature was cooled down to $T_{hold} = 730 \text{ }^\circ\text{C}$ and was kept constant for 300 s directly after the last compression. T_{hold} was chosen in a way that it was in the austenite/ferrite two phase region between A_{e1} and A_{e3} . In Figure 2e, pre-eutectoid ferrite is depicted along the PAGB. Therefore, our results indicate that DSIT ferrite, shown in Figure 2c,d and Figure 3, served as a nucleation site for the further formation of pre-eutectoid ferrite, shown in Figure 2e,f.

The STEM images in Figure 4 reveal that DSIT ferrite after route II has a large number of fine precipitates around 5 nm. However, the results of this work do not allow any statement to be made regarding whether the precipitates were already present in the steel before the

formation of DSIT ferrite, or whether they were precipitated during the formation of DSIT ferrite. Further investigations would have to be carried out in this regard. According to Hong et al. [13], NbC could act as a DSIT ferrite nucleation site. The APT measurements in this study also indicate this mechanism, as fine NbC precipitates (around 5 nm) were often detected in the area of the retained austenite/DSIT ferrite interface and DSIT ferrite itself, which can be seen in Figure 5b. A detailed analysis of the NbC precipitates revealed that they also contain small amounts of Ti and Cr. Figure 5b shows B segregation at the interface between DSIT ferrite and retained austenite in the 3D reconstruction. As B is known to segregate at PAGB, therefore delaying the austenite to ferrite phase transformation during cooling [24], our results suggest that the interface between DSIT ferrite and retained austenite in Figure 5b is a PAGB.

Previous research from Zheng et al. [16] and Hao et al. [17] indicated that the formation of DSIT ferrite is associated with C diffusion, whereas due to the short diffusion time, a ferrite oversaturated with C can remain. Our results confirm this, as the C concentration in DSIT ferrite after route II was on average 0.068 at% and decreased to 0.028 at% after route III. The further decrease in the C concentration between route II and route III indicates that the C diffusion during the formation of DSIT ferrite was insufficient. As a result, this led to the formation of DSIT ferrite oversaturated with C. The Mn concentration in the ferritic areas also decreased after route III (0.864 at%) compared to route II (0.980 at%). Both C and Mn are known to stabilize austenite, which is why it was assumed that they diffused into the neighboring retained austenite areas. In order to verify this, further APT measurements of retained austenite after route III would have to be carried out to determine the chemical composition in the equilibrium state. No decrease could be observed for the Cr concentration in ferrite between route II and route III. The scatter of the measured values does not allow for drawing any conclusions in this case.

The presence of retained austenite right next to DSIT ferrite suggests that C diffuses into the neighboring areas during the formation of DSIT ferrite, and leads to an enrichment with C. As a result, retained austenite was stabilized down to room temperature. According to Ghosh et al. [4], the fact that only C diffuses into neighboring areas during the formation of DSIT ferrite but not heavier elements, such as Mn, Si, or Cr, indicates that the formation is a displacive mechanism, although accompanied by C diffusion. The present APT investigations of DSIT ferrite (Figure 6) and its neighboring areas show that during the formation, there was only a diffusion of C and no other elements into the neighboring areas. This, in turn, supports the before mentioned assumption of a displacive mechanism. Furthermore, it is supported by the results of the EBSD measurement (Figures 8 and 9). The texture analysis of DSIT ferrite has shown that the $\langle 111 \rangle$ plane normals are parallel to the compression direction with the $\langle 110 \rangle$ directions pointing towards the radial direction of the compressed sample. The fact that there is a certain orientation relationship between the prior austenite grain and DSIT ferrite is, according to Ghosh et al. [4], also an indication for a displacive mechanism, as polygonal ferrite usually does not have any particular orientation relation with respect to its parent austenite grain. Although in the present case further experiments and EBSD measurements would be required to confirm and describe the displacive mechanism in more detail, our results indicate that the formation of DSIT ferrite is a displacive mechanism accompanied by C diffusion and the formation of retained austenite.

5. Conclusions

In this work, the microstructural, chemical, and crystallographic properties of DSIT ferrite were examined and compared with pre-eutectoid ferrite. In order to obtain the desired ferrite structure, various compression experiments were performed with a deformation dilatometer. Route I was chosen to check whether ferrite had already formed before the final deformation step of route II. Route II was chosen to produce DSIT ferrite through a final deformation step at a temperature of 750 °C and a strain of 0.4. The final experiment

temperature of route III (730 °C) was chosen in a way that pre-eutectoid ferrite formed during a final holding time of 300 s.

The results can be summarized as follows:

- The LOM and SEM analysis of the quenched dilatometer samples did show that DSIT ferrite formed predominantly along the PAGB during the final compression step of route II. Investigations of the quenched dilatometer samples after route III indicate that DSIT ferrite serves as a nucleation site for the formation of pre-eutectoid ferrite.
- APT measurements showed that the formation of DSIT ferrite was accompanied by the formation of retained austenite. This could be explained by the fact that C diffuses into neighboring areas during the formation of DSIT ferrite and stabilizes the austenite down to room temperature.
- STEM and APT measurements revealed the presence of fine NbC precipitates (around 5–10 nm) within DSIT ferrite, as well as at the interface between DSIT ferrite and retained austenite.
- During the formation of DSIT ferrite, only a diffusion of C into neighboring areas was observed. Both the Mn and Cr concentration were equal within DSIT ferrite and the neighboring retained austenite right after the formation of DSIT ferrite. The reason for this is assumed to be that the heavier elements, such as Mn and Cr, did not have enough time to diffuse during the formation of DSIT ferrite.
- The C and Mn concentrations within DSIT ferrite after route II were higher than the concentrations in the pre-eutectoid ferrite after route III. This leads to the assumption that C and Mn did not have enough time to diffuse during the formation of DSIT ferrite and that DSIT ferrite is therefore oversaturated with C and Mn right after the formation. To verify this, further APT measurements of retained austenite after route III would have to be carried out to determine the chemical composition in the equilibrium state.
- An EBSD measurement of the crystallographic orientation of DSIT ferrite after route II showed that the <111> plane normals were parallel to the compression direction, with the <110> directions pointing towards the radial direction of the compressed sample.
- It was found that during the formation of DSIT ferrite, only diffusion from C into neighboring areas occurred. At the same time a preferred orientation of DSIT ferrite in relation to the compression direction exists. This suggests that the formation of DSIT ferrite is a displacive mechanism, accompanied with C diffusion and the formation of retained austenite.

Author Contributions: Conceptualization, S.M., K.S.R., J.F., D.Z. and R.S.; methodology, S.M.; software, R.S.; validation, K.S.R., J.F., D.Z. and R.S.; investigation, S.M.; resources, K.S.R., J.F., D.Z. and R.S.; data curation, S.M.; writing—original draft preparation, S.M.; writing—review and editing, K.S.R., J.F. and R.S.; visualization, S.M.; supervision, R.S. and K.S.R.; project administration, S.M.; funding acquisition, R.S. All authors have read and agreed to the published version of the manuscript.

Funding: This research was funded by: Austrian BMK (846933) in the framework of the program 387 “Production of the future” and the “BMK Professorship for Industry”; Österreichische Forschungsförderungs GmbH (FFG:885187); Österreichische Forschungsförderungs GmbH (FFG:873200).

Data Availability Statement: Not applicable.

Conflicts of Interest: The authors declare no conflict of interest.

References

1. Buchmayr, B.; Hatzenbichler, T.; Kienreich, R.; Beyer, S. Werkstoff- und verfahrenstechnische Optimierung bei der Herstellung hochfester Schrauben. *Berg Huettenmaennische Mon.* **2008**, *153*, 423–429. [[CrossRef](#)]
2. Beladi, H.; Kelly, G.L.; Hodgson, P.D. Ultrafine grained structure formation in steels using dynamic strain induced transformation processing. *Int. Mater. Rev.* **2007**, *52*, 14–28. [[CrossRef](#)]
3. Zhao, L.; Park, N.; Tian, Y.; Shibata, A.; Tsuji, N. Dynamic Transformation Mechanism for Producing Ultrafine Grained Steels. *Adv. Eng. Mater.* **2018**, *20*, 1701016. [[CrossRef](#)]

4. Ghosh, C.; Aranas, C.; Jonas, J.J. Dynamic transformation of deformed austenite at temperatures above the Ae3. *Prog. Mater. Sci.* **2016**, *82*, 151–233. [[CrossRef](#)]
5. Priestner, R.; de los Rios, E. Ferrite grain refinement by controlled rolling of low-carbon and microalloyed steel. *Met. Technol.* **1980**, *7*, 309–316. [[CrossRef](#)]
6. Yada, H.; Li, C.-M.; Yamagata, H. Dynamic $\gamma \rightarrow \alpha$ Transformation during Hot Deformation in Iron-Nickel-Carbon Alloys. *ISIJ Int.* **2000**, *40*, 200–206. [[CrossRef](#)]
7. Poliak, E.I.; Jonas, J.J. A one-parameter approach to determining the critical conditions for the initiation of dynamic recrystallization. *Acta Mater.* **1996**, *44*, 127–136. [[CrossRef](#)]
8. Poliak, E.I.; Jonas, J.J. Initiation of Dynamic Recrystallization in Constant Strain Rate Hot Deformation. *ISIJ Int.* **2003**, *43*, 684–691. [[CrossRef](#)]
9. Sun, L.; Muszka, K.; Wynne, B.P.; Palmiere, E.J. Effect of strain path on dynamic strain-induced transformation in a microalloyed steel. *Acta Mater.* **2014**, *66*, 132–149. [[CrossRef](#)]
10. Choi, J.-K.; Seo, D.-H.; Lee, J.-S.; Um, K.-K.; Choo, W.-Y. Formation of Ultrafine Ferrite by Strain-induced Dynamic Transformation in Plain Low Carbon Steel. *ISIJ Int.* **2003**, *43*, 746–754. [[CrossRef](#)]
11. Beladi, H.; Kelly, G.L.; Shokouhi, A.; Hodgson, P.D. The evolution of ultrafine ferrite formation through dynamic strain-induced transformation. *Mater. Sci. Eng. A* **2004**, *371*, 343–352. [[CrossRef](#)]
12. Bae, Y.H.; Lee, J.S.; Choi, J.-K.; Choo, W.-Y.; Hong, S.H. Effects of Austenite Conditioning on Austenite/Ferrite Phase Transformation of HSLA Steel. *Mater. Trans.* **2004**, *45*, 137–142. [[CrossRef](#)]
13. Hong, S.C.; Lim, S.H.; Hong, H.S.; Lee, K.J.; Shin, D.H.; Lee, K.S. Effect of Nb on grain growth of ferrite in C-Mn steel during isothermal holding after severe deformation. *Mater. Sci. Technol.* **2004**, *20*, 207–212. [[CrossRef](#)]
14. Gourdet, S.; Montheillet, F. A model of continuous dynamic recrystallization. *Acta Mater.* **2003**, *51*, 2685–2699. [[CrossRef](#)]
15. Pandi, R.; Yue, S. Dynamic Transformation of Austenite to Ferrite in Low Carbon Steel. *ISIJ Int.* **1994**, *34*, 270–279. [[CrossRef](#)]
16. Zheng, C.; Xiao, N.; Hao, L.; Li, D.; Li, Y. Numerical simulation of dynamic strain-induced austenite–ferrite transformation in a low carbon steel. *Acta Mater.* **2009**, *57*, 2956–2968. [[CrossRef](#)]
17. Hao, L.; Sun, M.; Xiao, N.; Li, D. Characterizations of Dynamic Strain-induced Transformation in Low Carbon Steel. *J. Mater. Sci. Technol.* **2012**, *28*, 1095–1101. [[CrossRef](#)]
18. Hurley, P.J.; Hodgson, P.D.; Muddle, B.C. Analysis and characterisation of ultra-fine ferrite produced during a new steel strip rolling process. *Scr. Mater.* **1999**, *40*, 433–438. [[CrossRef](#)]
19. Irvine, K.J.; Pickering, F.B.; Gladman, T. Grain-refined C-Mn steels. *J. Iron Steel Res. Int.* **1967**, *205*, 161–182.
20. Miller, M.K.; Russell, K.F.; Thompson, G.B. Strategies for fabricating atom probe specimens with a dual beam FIB. *Ultramicroscopy* **2005**, *102*, 287–298. [[CrossRef](#)] [[PubMed](#)]
21. Lefebvre-Ulrikson, W.; Vurpillot, F.; Sauvage, X. (Eds.) *Atom Probe Tomography: Put Theory into Practice*; Academic Press: London, UK, 2016; ISBN 0128046473.
22. Lerchbacher, C.; Zinner, S.; Leitner, H. Atom probe study of the carbon distribution in a hardened martensitic hot-work tool steel X38CrMoV5-1. *Micron* **2012**, *43*, 818–826. [[CrossRef](#)] [[PubMed](#)]
23. Sun, X.; Dong, H.; Liu, Q.; Weng, Y. Dynamically transformed ferrite fraction inferred from dilatometry measurements after deformation. *Mater. Sci. Eng. A* **2008**, *487*, 93–98. [[CrossRef](#)]
24. He, X.L.; Chu, Y.Y.; Jonas, J.J. Grain boundary segregation of boron during continuous cooling. *Acta Metall.* **1989**, *37*, 147–161. [[CrossRef](#)]

5.2 Conference Contributions

Conference talk I: Stefan Monschein, Katharina S. Ragger, Dominik Zügner, Josef Fasching and Ronald Schnitzer

Influence of Nb and Ti on the recrystallization and precipitation behavior of HSLA steels
EUROMAT 2021, (virtual, 13-17 September, 2021)

5.3 Co - supervised theses

(I) Nikolaus Kostwein: *Metallographische Analyse des Rekrystallisationsverhaltens eines mikrolegierten Stahls*, Bachelor thesis, Montanuniversität Leoben, 2021

(II) Katharina Käsznar: *Einfluss der Prozessparameter auf die Gefügeentwicklung von Kaltfließpressstählen bei thermomechanischer Umformung*, Master thesis, Montanuniversität Leoben, 2022

(III) Jakob Eschelbeck: *Einfluss von Temperatur auf das Kornwachstum und Rekrystallisationsverhalten von HSLA-Stählen*, Master thesis, Montanuniversität Leoben, 2022

6 Summary and discussion of the published content

6.1 Aim and scope of the investigations

Although HSLA steel concepts containing MAE, such as Nb and Ti, have already emerged in the 1960s, they were mainly limited to steels with C contents below 0.1 wt%. Due to increased requirements in terms of strength and toughness, the development of high performance wire products is also moving towards a combination of microalloyed HSLA steels with higher C contents and TMCP. Thus, there is still great research potential, especially with regard to the interaction of the MAE and deformation parameters of the TMCP on the product properties during and after deformation.

For this reason, seven HSLA steels with different contents of MAE were examined in this thesis. The chemical composition of the steels and a list of the peer - reviewed publications (chapter 5.1) in which they were examined is given in Table 2.

Table 2: Chemical composition of the investigated steels.

	C	Mn	Ni	Cr	Mo	Si	N	Nb	Ti	B	
	wt%	wt%	wt%	wt%	wt%	wt%	wt%	wt%	wt%	wt%	Paper
steel A	0.23	1.25	0.48	0.48	0.23	0.21	0.006	-	-	-	II
steel B	0.22	1.27	0.48	0.49	0.24	0.22	0.012	0.026	0.015	-	I + II
steel C	0.21	1.33	1.06	0.57	0.56	0.21	0.005	-	-	-	III
steel D	0.24	1.34	1.05	0.56	0.55	0.39	0.012	0.022	0.002	-	III
steel E	0.24	1.32	1.04	0.55	0.54	0.20	0.012	0.020	0.009	-	III
steel F	0.24	1.32	1.04	0.55	0.54	0.20	0.014	0.021	0.018	-	III
steel G	0.32	0.98	-	0.43	-	0.10	0.004	0.011	0.022	0.002	IV

Both steel A and steel B were manufactured and rolled on an industrial scale and delivered as wires in the as - rolled condition. For both steels, the annealing temperature prior to the rolling process was 1100 °C, with a finishing rolling temperature between 800 °C and 900 °C. Steel C, D, E, F and G were produced on a small scale facility by vacuum induction melting to ingots. After solidifying, steel C, D, E and F were reannealed to a temperature of 1150 °C and forged to a diameter of 30 mm. Steel G was reheated to a temperature of 1100 °C and rolled to a sheet thickness of 15 mm with a finishing rolling temperature of 900 °C. By using a combination of dilatometer experiments and standard - to high - resolution characterization methods, the following questions were intended to be answered:

- Which methods are suitable for determining the degree of recrystallization and are there alternatives to prevent costly dilatometer experiments?

- How do different contents of Nb and Ti influence the recrystallization - and grain growth behavior?
- What influence do the precipitates possess and how can they be characterized by modern high - resolution methods?
- How do different TMCP parameters, such as annealing temperature, deformation temperature and different deformation rates influence recrystallization, the precipitation behavior and the microstructure?

Numerous investigations were carried out on the steels listed in Table 2 in order to be able to answer the above questions. For better visualization Figure 6.1 illustrates a workflow diagram showing the connection between the questions, the examined steels, the used methods and peer - reviewed publications.

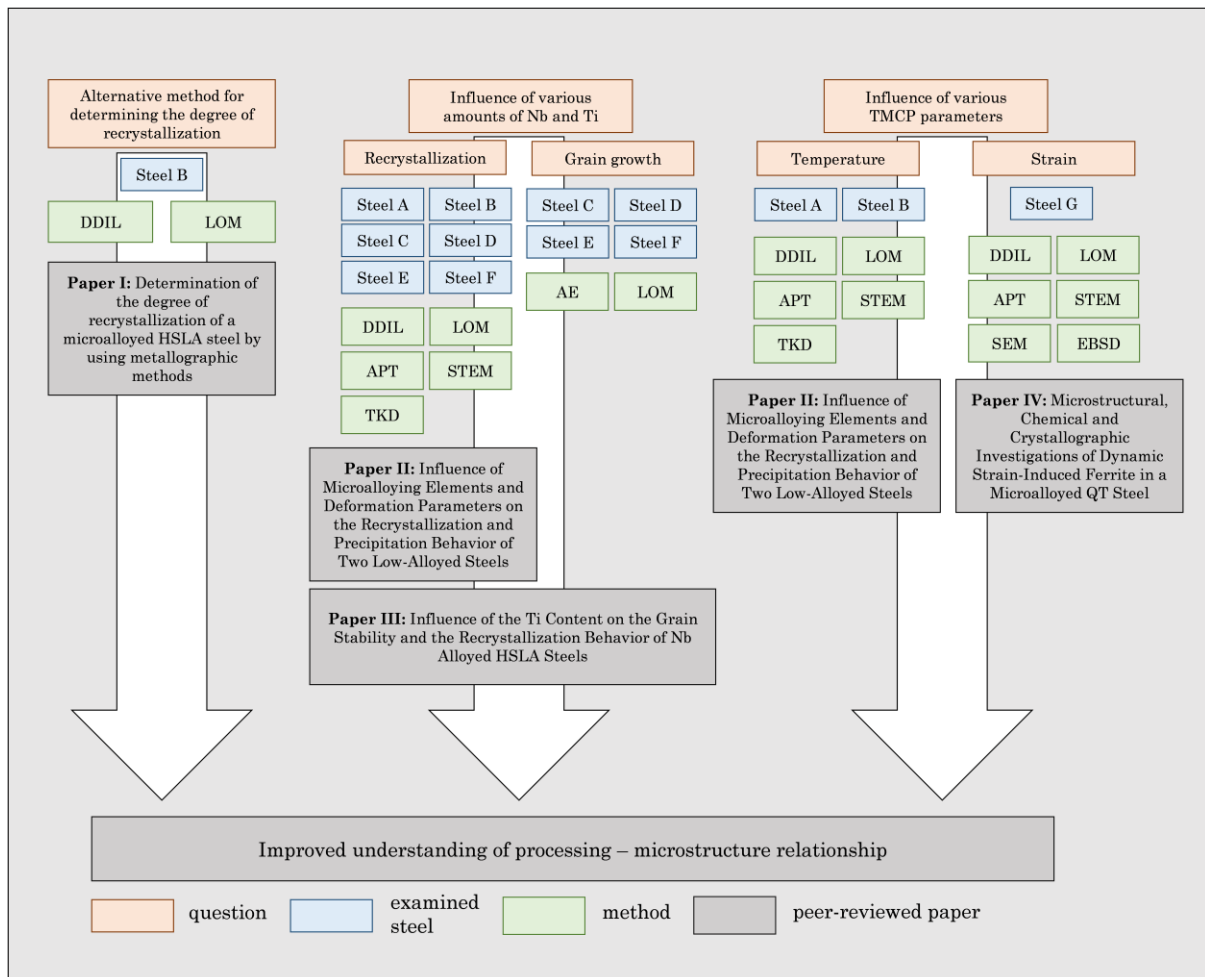


Figure 6.1: Workflow diagram showing the connection between the questions, the examined steels, the used methods and peer - reviewed publications (deformation dilatometer (DDIL), light optical microscopy (LOM), atom probe tomography (APT), scanning transmission electron microscopy (STEM), transmission Kikuchi diffraction (TKD), scanning electron microscopy (SEM), annealing experiments (AE))

6.2 Development of a method for determining the degree of recrystallization

In the past, numerous direct and indirect methods were used to determine the degree of recrystallization of a microstructure. Metallographic methods [130], micro hardness measurements [131] or measurements using EBSD [131,132] can be mentioned here as an example. What these methods have in common, however, is that they are either difficult to automate or require complex sample preparation. Therefore, *Paper I* dealt with the question of developing an alternative method having the future potential to determine the degree of recrystallization of microalloyed steels directly, easily and cost - effectively using a combination of light optical microscopy and advanced software solutions. For this reason, samples of steel B were deformed using single - hit compression tests on a deformation dilatometer in order to produce defined degrees of recrystallization. To be able to generate a specific degree of recrystallization using single - hit compression tests, the recrystallization kinetics had to be determined in advance using double - hit compression tests (the experimental procedure of double - hit experiments is described in detail in chapter 3.1). The results of the determination of the recrystallization kinetics via double - hit deformation tests are published in *Paper II*, with Figure 6.2 showing an example of the degree of recrystallization over time after a T_a of 1250 °C and a T_{def} of 850 °C.

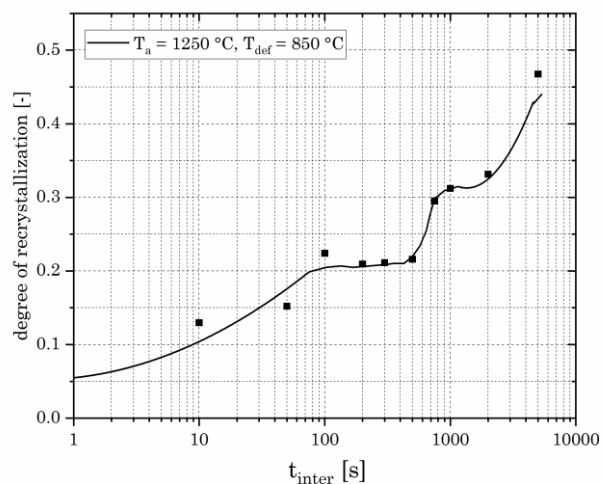


Figure 6.2: Course of the degree of recrystallization over time determined using double - hit deformation experiments on steel B after a T_a of 1250 °C and a T_{def} of 850 °C. Image adapted and reprinted with permission from Paper II.

The LOM determination of the degree of recrystallization from *Paper I* can be summarized using Figure 6.3.

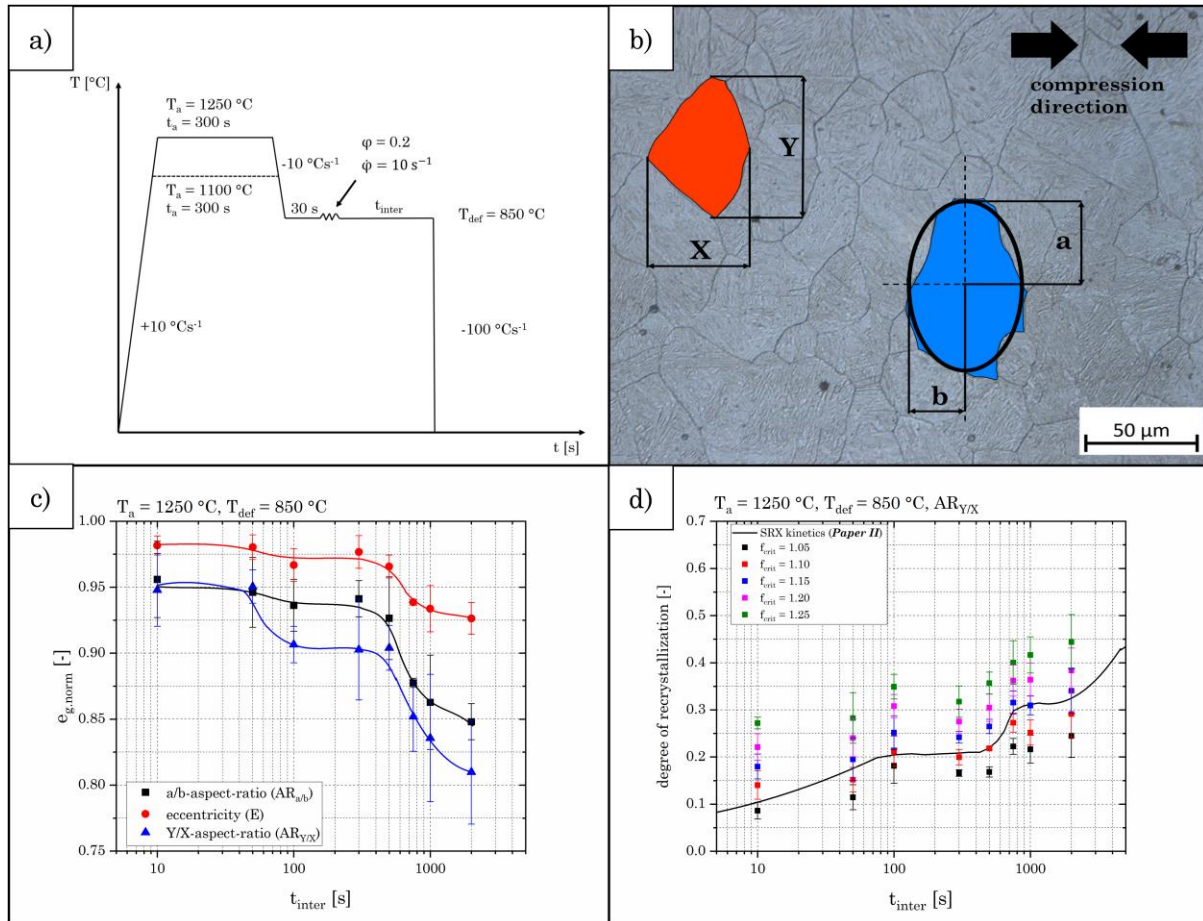


Figure 6.3: a) Schematic illustration of the time - temperature - deformation schedule of the single - hit deformation experiment. b) LOM image of a deformed sample after the single - hit compression test. The red and blue grains are used for better visualization of the parameters used to determine the grain elongation. c) Course of the three grain elongation parameters over time after the single - hit deformation experiments. d) Course of the degree of recrystallization over time determined using double - hit deformation tests and single - hit deformation tests. All images adapted and reprinted with permission from Paper I.

Figure 6.3 a) shows a schematic illustration of the time - temperature - deformation schedule of the single - hit compression experiments, which were used in order to produce samples with a specific degree of recrystallization. Comparing the time - temperature - deformation schedule of the single - hit deformation experiment with that of the double - hit deformation experiment, it is noticeable that they only differ from each other in the absence of the second deformation step. Therefore, the recrystallization kinetics determined in *Paper II* could be used for the experiments in *Paper I*. Furthermore, the grain elongation of the deformed samples was used to determine the degree of recrystallization. For this reason, three parameters were defined with which the grain elongation can be described and compared with each other. On the one hand, the grain elongation was determined via the length - to - width ratio of the stretched grains

(Y/X - aspect - ratio ($AR_{Y/X}$)), but also determined by two other parameters (the a/b - aspect - ratio ($AR_{a/b}$) and the eccentricity (E)) that require an ellipse to be fitted into the respective grains (for better visualization see Figure 6.3 b)). By comparing the three parameters, it was shown that the $AR_{Y/X}$ is best suited to describe grain elongation, since this parameter provides the highest sensitivity with regard to changes in grain elongation. This can be shown by comparing Figure 6.2 and Figure 6.3 c), since both, the course of the degree of recrystallization over time and the course of grain elongation over time show the formation of a plateau after the same t_{inter} (the formation of strain - induced precipitates in both cases is responsible for the formation of the plateau). In order to be able to quantify the degree of recrystallization based on grain elongation, a critical value of grain elongation (f_{crit}) was defined, below which a grain can be assumed to be recrystallized. This allows to calculate the degree of recrystallization from the ratio of the recrystallized grains of a LOM image and the total number of all grains in the image. The curves in Figure 6.3 d) show that with the optimal choice of f_{crit} , the recrystallization determined by single - hit deformation tests matches well with the recrystallization kinetics determined in *Paper II*.

Since modern software solutions in combination with suitable etching methods make it possible to identify individual grains in a microstructure and calculate their grain elongation, the method described in *Paper I* offers a simple and automatable way of determining the degree of recrystallization of microalloyed steels using light microscopy in combination with image processing.

6.3 Characterization of microalloy precipitates

As already explained in detail in chapter 2.3, MAE influence both the behavior during deformation (e.g. recrystallization and recovery) and the mechanical properties in the final condition. Responsible for this are on the one hand fine precipitates, as well as small contents dissolved in the matrix. In order to be able to examine such fine precipitates and to gain knowledge about their influence on the properties of the steel, it is necessary to use high - resolution characterization methods. For this reason, the alloys from Table 2 were examined using APT, STEM, TKD and EDX and the findings about the precipitates of the steels alloyed with Nb and Ti is summarized here.

The largest precipitates found with the four before mentioned high - resolution characterization methods ranged in a size around 50 to 100 nm. Figure 6.4 a) depicts a STEM image of a 90 nm small rectangular precipitate, which was extracted from steel B in the as - rolled condition using the carbon replica method (more information in

chapter 3.3). Using EDX (Figure 6.4 b)) it could be shown that the precipitate in Figure 6.4 a) is a carbonitride containing Ti and Nb. A slightly smaller precipitate with a size around 40 nm is shown in Figure 6.4 c) and was found by using APT on a deformed sample of steel E after a double - hit deformation test. The chemical composition of this precipitate is shown in Figure 6.4 d) and also shows that this precipitate is a carbonitride containing mainly Ti and Nb, but also small amounts of Cr and Ni.

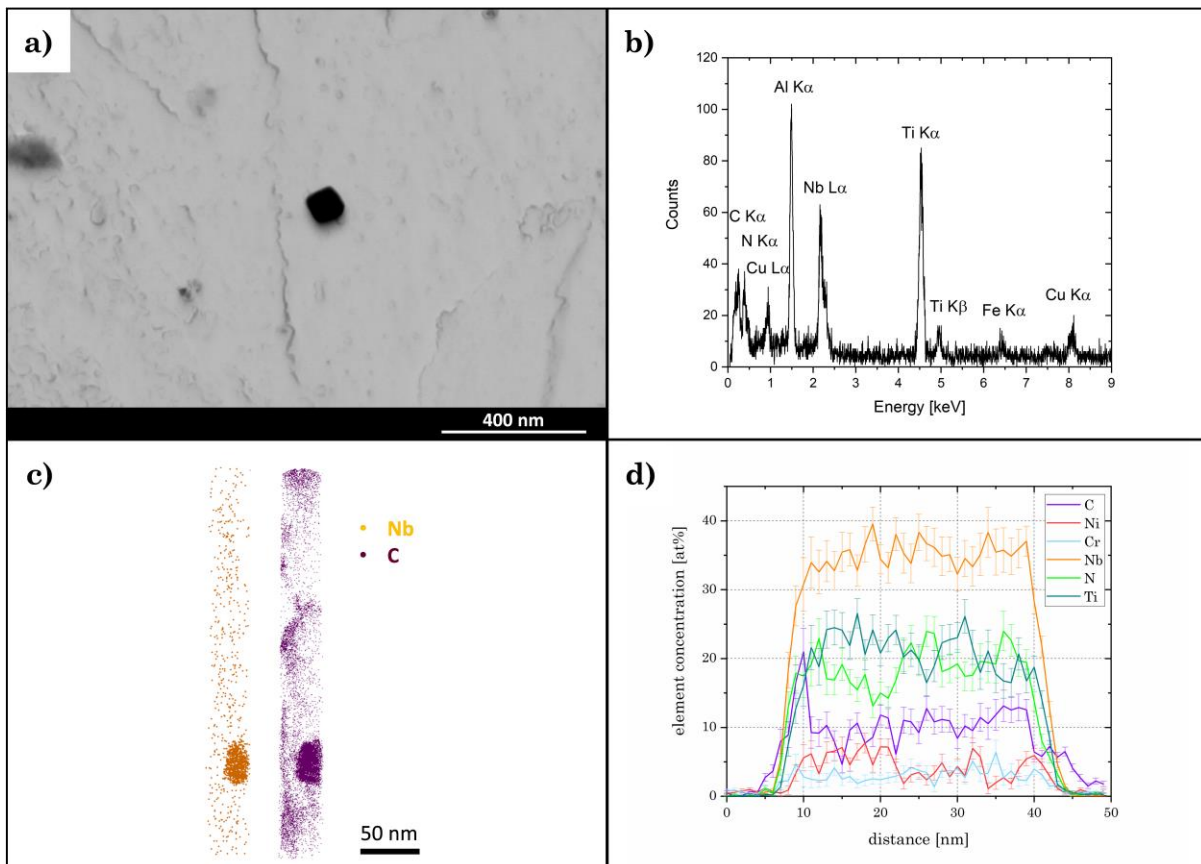


Figure 6.4: a) STEM image of a 90 nm rectangular precipitate which was extracted from steel B in the as - rolled condition using the carbon replica method. b) corresponding EDX spectra of the precipitate in a). c) 3D reconstruction of a 40 nm small precipitate found in steel E after a double - hit deformation test. d) corresponding chemical profile of the precipitate in c). Image a) and b) adapted and reprinted with permission from Paper II. Image c) and d) adapted and reprinted with permission from Paper III.

In the as - rolled condition of steel B, precipitates with a size around 20 nm were found, which can be seen in Figure 6.5 a) and Figure 6.5 c). By using EDX (Figure 6.5 b)) and TKD (Figure 6.5 d)) it could be shown that these are TiN precipitates.

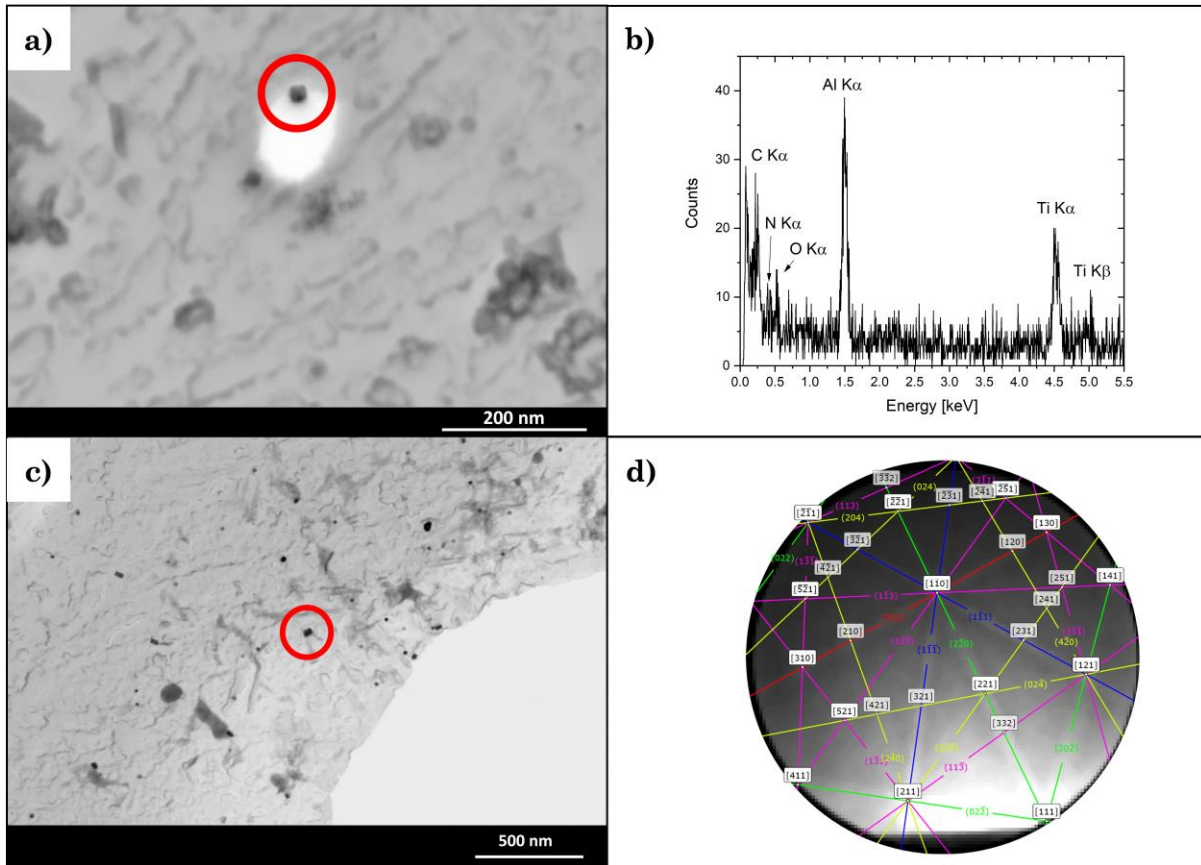


Figure 6.5: a) and c) STEM images of 20 nm rectangular precipitates which were extracted from steel B in the as - rolled condition using the carbon replica method. b) corresponding EDX spectra of the precipitate in a). d) corresponding Kikuchi pattern after TKD on the precipitate in c) with the best matching solution according to the analysis software TEAM v.4.3. All images adapted and reprinted with permission from Paper II.

The smallest precipitates found with the high - resolution characterization methods were about 5 nm small NbC - and Nb(C,N) precipitates. In **Paper II** and **Paper III** these were strain - induced precipitates found along dislocations in specimens after double - hit deformation tests, whereas in **Paper IV** these fine precipitates were found in large number inside DSIT ferrite and at the grain boundary between DSIT ferrite and retained austenite. Figure 6.6 a) shows a STEM image of strain - induced Nb(C,N) precipitates in steel B along dislocations after a double - hit deformation test. Strain - induced precipitates were also found in steel D, steel E and steel F after such tests, with Figure 6.6 b) showing the chemical profile of such a precipitate in steel D, analyzed using APT. Besides Nb, C and N also small amounts of Mo and Cr were found inside the precipitates. Figure 6.6 c) depicts a STEM image of NbC precipitates inside DSIT ferrite in steel G, with the corresponding chemical profile of one precipitate in Figure 6.6 d), analyzed using APT. In addition to the main elements Nb and C, also small amounts of Cr and Ti were found inside the precipitates.

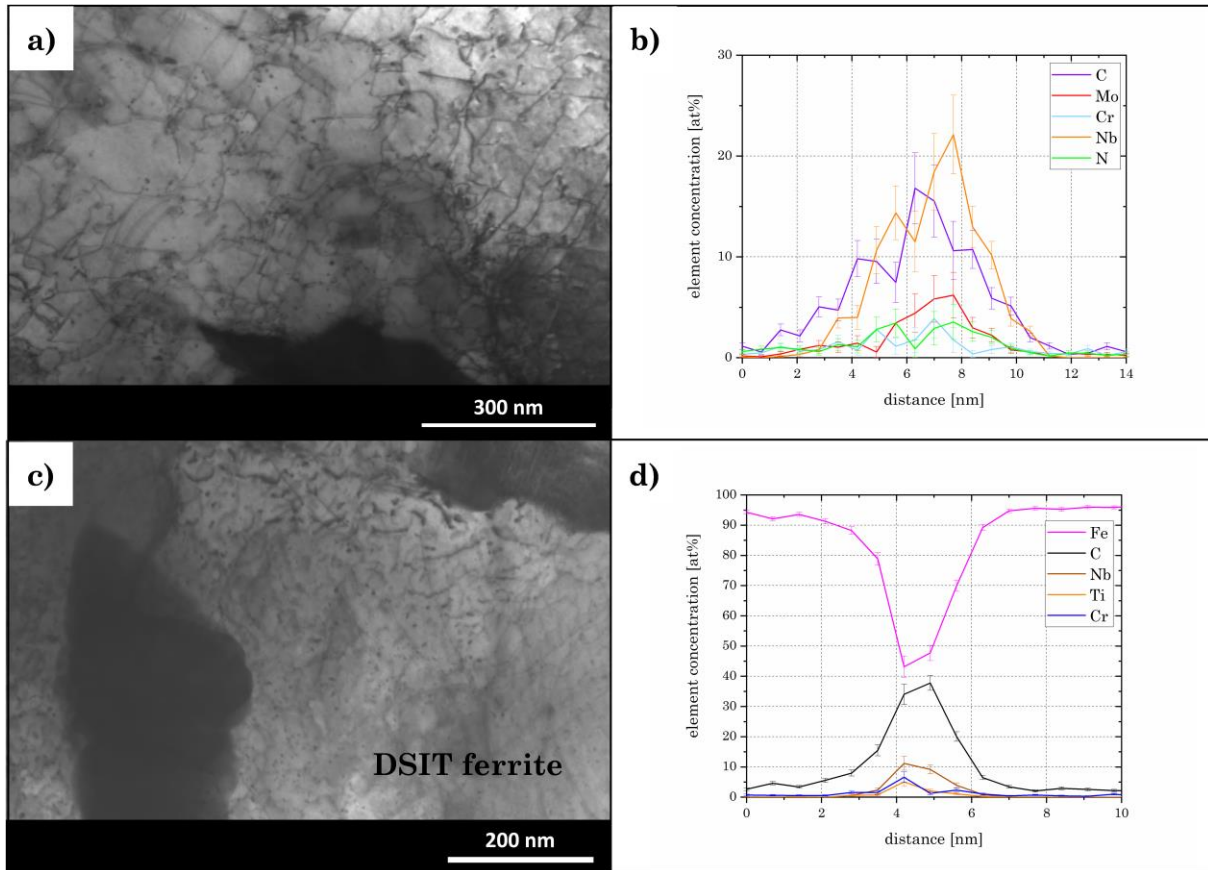


Figure 6.6: a) STEM image of strain - induced Nb(C,N) precipitates in steel B along dislocations after a double - hit deformation test. b) Chemical profile of a strain - induced Nb(C,N) precipitate in steel D, analyzed using APT. c) STEM image of NbC precipitates inside DSIT ferrite in steel G. d) Corresponding chemical profile of a NbC precipitate in c), analyzed using APT. Image a) adapted and reprinted with permission from Paper II. Image b) adapted and reprinted with permission from Paper III. Image c) and d) adapted and reprinted with permission from Paper IV.

6.4 Influence of deformation parameters on recrystallization and microstructure

One question from *Paper II* dealt with the influence of different annealing - and deformation temperatures on the recrystallization behavior. For this reason, on samples of steel A and steel B double - hit deformation experiments with different T_a and T_{def} were carried out. The knowledge gained from these experiments can be explained using the curves in Figure 6.7. Figure 6.7 a) shows the results of the tests on samples of steel B, which were deformed at the same T_{def} , but had a different T_a . It can be seen that the recrystallization kinetic slows down with an increasing T_a . Two reasons can explain this phenomenon:

1) It is well known that the austenite grain size during annealing depends on the annealing time, but to a much greater extend on the temperature [133,134]. An increase

in T_a therefore leads to a larger grain size and thus to a reduction in the total area of grain boundaries. Since these serve as nucleation sites during recrystallization, this leads to slower recrystallization kinetics [2,61].

2) Since steel B is a microalloyed steel, an increase in T_a leads to a larger proportion of dissolved Nb in the matrix. On the one hand, this delays recrystallization due to the solute drag effect [27,28], but also due to the formation of strain - induced precipitates. The latter point is shown by the formation of a plateau in the recrystallization curve and in the past was reported over a wide range of microalloyed steels [30,76,78]. It can also be observed in Figure 6.7 a) at a t_{inter} between 100 and 500 s. More details on these strain - induced precipitates can be found in Figure 6.6 a) and b).

From Figure 6.7 b) it can be seen that the recrystallization of steel A occurs faster with an increasing T_{def} . Since steel A is not a microalloyed steel, this recrystallization behavior was to be expected and can also be described by fitting the JMAK equation (equation 7 in chapter 2.4) to the data points.

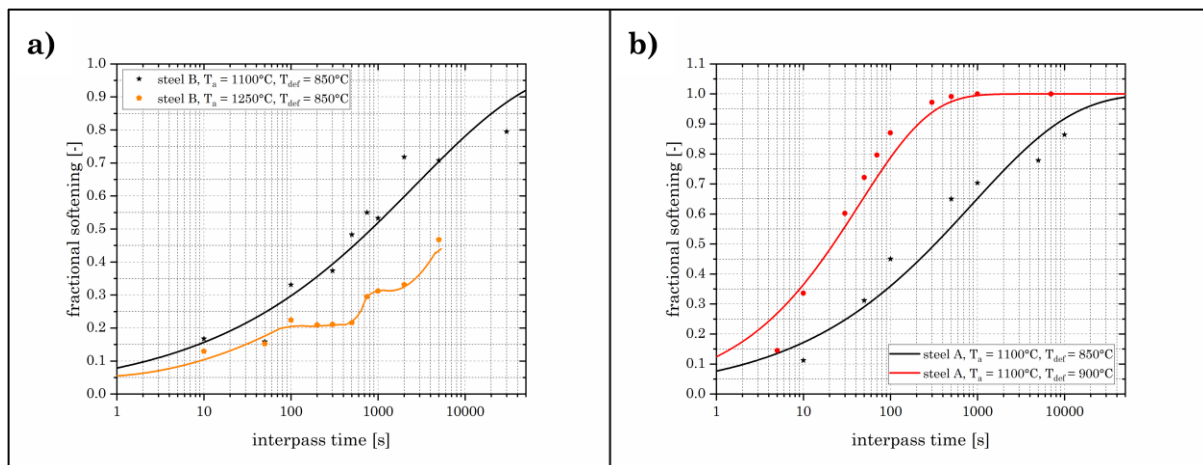


Figure 6.7: Fractional softening determined by using double - hit deformation experiments on samples of steel A and B with varying parameters. a) T_a and b) T_{def} . Both images adapted and reprinted with permission from Paper II.

A reduction of T_{def} not only reduces the recrystallization kinetics, but makes it also possible to dynamically form strain - induced transformed (DSIT) ferrite when the temperature falls below a critical value, even in the austenite regime. In order for this to take place, T_{def} must be somewhere between A_{e3} (equilibrium temperature of the austenite to ferrite transformation) and A_{r3} (transformation temperature from austenite to ferrite, depending on the cooling rate) and a critical degree of deformation must be introduced. Although the formation of DSIT ferrite has been thoroughly investigated in the past [135–139], there are still open questions regarding the exact mechanism of formation. Studies by Zheng et al. [138] and Hao et al. [137] rather suggest that the formation of

DSIT ferrite is more of a diffusional transformation process since it is accompanied by the diffusion of C, whereas results of Hurley et al. [140] indicate a displacive mechanism.

For this reason, steel G was deformed using a deformation dilatometer in such a way that on the one hand DSIT ferrite has formed and on the other hand could be compared with pre - eutectoid ferrite under equilibrium conditions. APT was used to investigate the diffusional behavior of the alloy elements during the formation of DSIT ferrite and to analyze the chemical composition of DSIT ferrite and pre - eutectoid ferrite. By using EBSD the crystallographic orientation of DSIT ferrite was investigated. The results are published in *Paper IV* and are briefly summarized in this section.

Figure 6.8 a) depicts a 3D reconstruction of an APT measurement of steel G, showing DSIT ferrite (upper part) and retained austenite (lower part). The chemical profile was created along the blue cylinder in the reconstruction and the results are placed right next to it. The chemical depth profile shows that a diffusion of C into the neighboring areas takes place during the formation of DSIT ferrite. However, no diffusion of the heavier elements Cr and Mn could be observed. This indicates that the formation of DSIT ferrite is only accompanied by the diffusion of C. The chemical composition of DSIT ferrite and pre - eutectoid ferrite were measured using APT and the results are depicted in Figure 6.8 b) - Figure 6.8 d). The results show that although the formation of DSIT ferrite is accompanied by the diffusion of C, the concentration in pre - eutectoid ferrite is even lower. This indicates that DSIT ferrite is oversaturated with C, since there is apparently not enough time for all C atoms to diffuse during the formation of DSIT ferrite. A similar trend can be observed for Mn. Although there is no diffusion of Mn during the formation of DSIT ferrite, the concentration in pre - eutectoid ferrite decreases. This means that DSIT ferrite is not just oversaturated with C but also Mn. No clear trend could be observed with regard to the Cr content, as there was a large scatter of the measured values. By using EBSD the crystallographic orientation of DSIT ferrite was analyzed and the corresponding texture plot is given in Figure 6.9. The results show that the $\langle 111 \rangle$ plane normals of DSIT ferrite are oriented parallel to the deformation direction with the $\langle 110 \rangle$ directions of DSIT ferrite pointing towards the radial direction of the compressed samples. The fact that there is a preferred orientation of DSIT ferrite in relation to the direction of deformation suggests that the formation is a displacive mechanism, although accompanied by the diffusion of C.

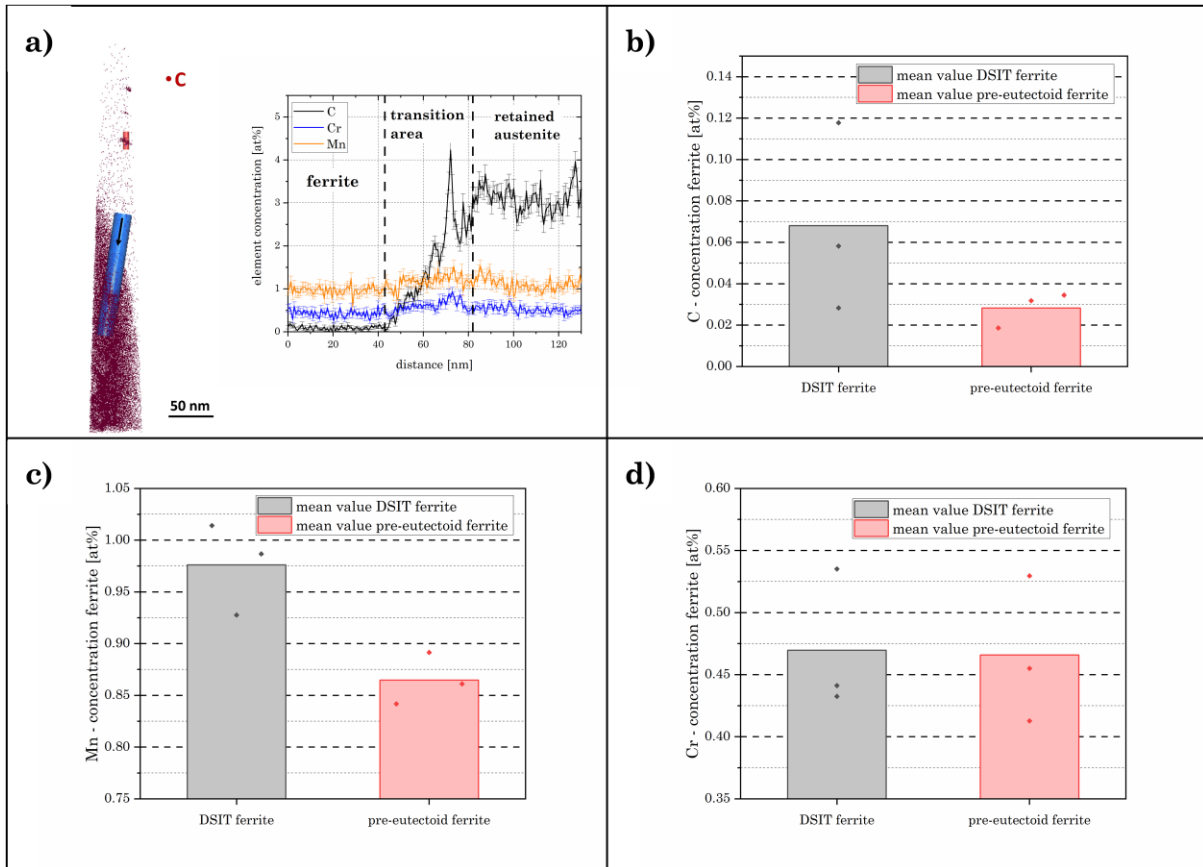


Figure 6.8: a) 3D reconstruction of an APT measurement of DSIT ferrite and the corresponding chemical depth profile along the blue cylinder. b) C concentration in DSIT ferrite and pre - eutectoid ferrite. c) Mn concentration in DSIT ferrite and pre - eutectoid ferrite. d) Cr concentration in DSIT ferrite and pre - eutectoid ferrite. All images adapted and reprinted with permission from Paper IV.

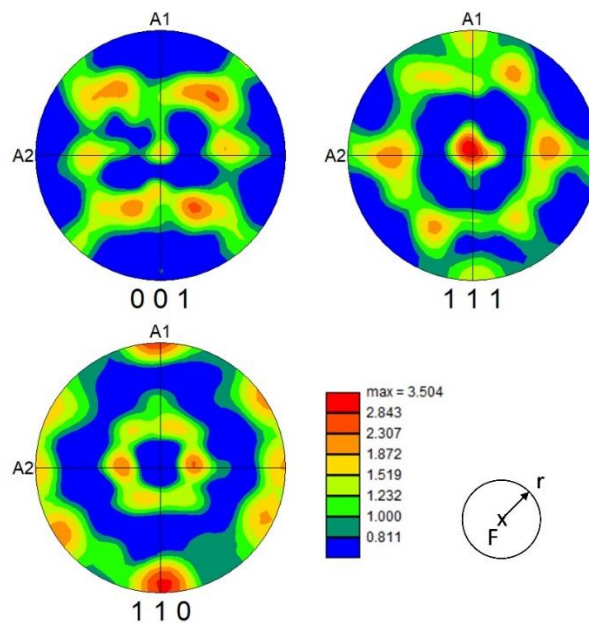


Figure 6.9: Texture plot of DSIT ferrite in compression direction. Image reprinted with permission from Paper IV.

6.5 Influence of the microalloying elements on recrystallization, grain growth and microstructure

In *Paper II*, a microalloy - free steel (steel A) and a microalloyed steel (steel B) were analyzed and compared with each other in the as - rolled condition and after several double - hit deformation experiments. In the as - rolled condition both steels were delivered as wire rod and went through an identical rolling process. Steel B had a finer microstructure in the as - rolled condition compared with steel A. High - resolution characterization methods such as STEM combined with EDX and TKD revealed that TiN precipitates with a size around 15 nm (Figure 6.5) and (Nb,Ti)(C,N) precipitates with a size around 40 - 100 nm (Figure 6.4) were responsible for this, due to a pinning effect of the grain boundaries during the annealing process prior to rolling. The results of this study coincide well with studies by George et al. [141] and Cuddy et al. [142], who were able to show that TiN precipitates of the same order of size were responsible for inhibiting grain coarsening, due to a pinning of the grain boundaries.

In both *Paper II* and *Paper III*, the recrystallization behavior of microalloyed steels was investigated by means of double - hit deformation tests and compared to microalloy - free steels. When comparing the microalloyed with the microalloy - free steels, in both cases a same trend was observed with regard to the recrystallization behavior. All microalloyed steels recrystallized more slowly than their microalloy - free reference alloys. Responsible for this were on the one hand the solute drag effect [27,28], as well as the microalloy precipitates present in the steel [2,76,78]. Figure 6.10 illustrates the course of recrystallization over time of the microalloyed steels B, D, E and F after the double - hit deformation tests. Comparing the four curves indicates that steel B shows the slowest recrystallization behavior. Steel B and steel F are similar in terms of the content of MAE, with the difference that the Ni content in steel B is 0.48 wt% and in steel F 1.04 wt%. In this case, the slower recrystallization of steel B can therefore be attributed to the higher T_a of 1250 °C, which apparently led to a higher proportion of dissolved MAE and therefore slowed down recrystallization due to the solute drag effect. Steel D, E and F only differ in different Ti contents, with the Ti content in steel D being 20 ppm, in steel E 90 ppm and in steel F 180 ppm. Comparing only the curves of these three steels. It can be seen that recrystallization slows down as the Ti content decreases. After determining the content of dissolved Nb in the matrix of quenched samples after double - hit deformation test after a t_{inter} of 300 s, it can be shown in Figure 6.11 that the content of dissolved Nb in the matrix decreases continuously from steel D to steel F. Therefore, it is assumed that the

delayed recrystallization of steel D is due to more Nb being available to form strain - induced NbC precipitates, which inhibit recrystallization. This is due to the fact that with increasing Ti content, certain amounts of Nb are already bound in (Nb,Ti)(C,N) precipitates, which were detected by STEM, EDX and APT (Figure 6.4). Furthermore, this theory is also supported by the fact that all 4 curves show a plateau beginning at a t_{inter} of 100 s, which indicates the formation of strain - induced NbC precipitates (for further information see Figure 6.6 a) and b)) and that this plateau is most pronounced in the curve of steel D. In addition to the recrystallization - retarding effect caused by these fine NbC precipitates, they apparently also serve as nucleation sites for the formation of DSIT ferrite. Figure 6.6 c) and d) show that large amounts of these precipitates were found within DSIT ferrite, suggesting these precipitates serve as nucleation sites, which is also consistent with results from Hong et al. [143].

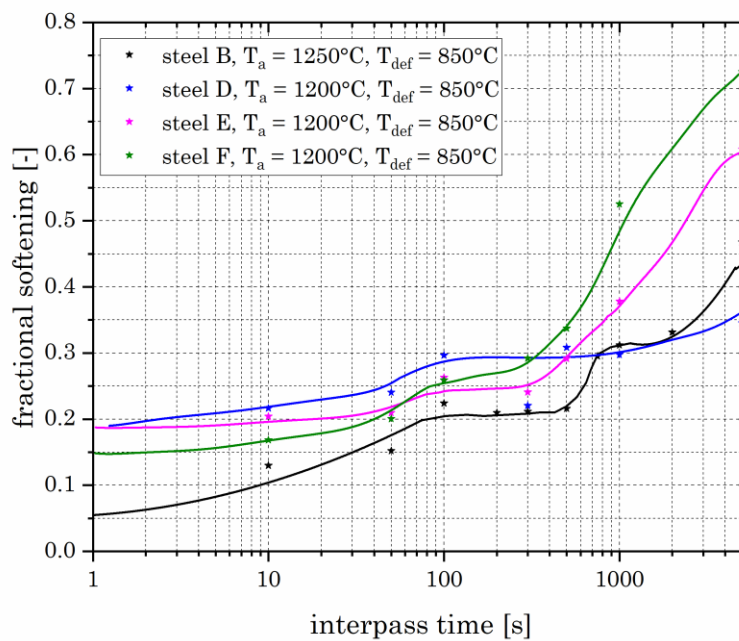


Figure 6.10: Fractional softening determined by using double - hit deformation experiments on samples of steel B, D, E and F. Image adapted and reprinted with permission from Paper II and Paper III.

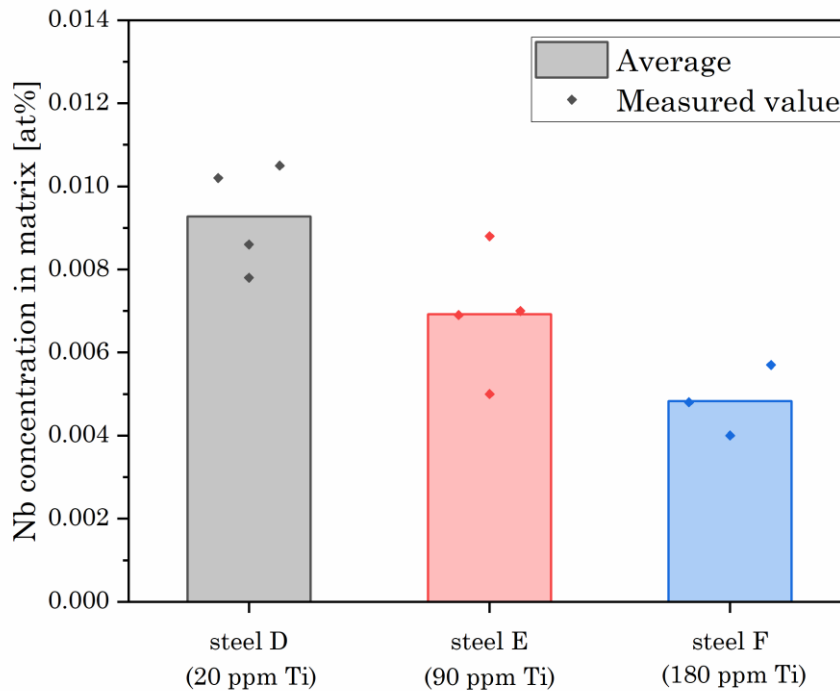


Figure 6.11: Nb concentration in solute solution in the matrix after double-hit deformation tests and a t_{inter} of 300 s. Concentration determined with APT. Image adapted and reprinted with permission from Paper III.

The effect of different levels of Nb and Ti on grain coarsening behavior was also examined in **Paper III** by annealing treatments followed by metallographic analysis and the results are depicted in Figure 6.12. The course of the mean grain size of the prior austenite grains (d_{mean}) over T_a shows that all microalloyed steels (steel D, E and F) show less grain coarsening compared to the microalloy-free reference alloy steel C. The TiN (Figure 6.5), (Ti,Nb)(C,N) (Figure 6.4) and NbC precipitates described in chapter 6.3 are responsible for this effect, due to a pinning of the grain boundaries during annealing. It is noticeable that the addition of Ti in steels E and F provides a clear advantage over steel D, but there is hardly any difference whether the Ti content is 90 ppm or 180 ppm. This in turn is in contradiction to the results from Figure 6.10, which did show that a lower content of Ti has a positive effect on recrystallization retardation. In summary, for microalloyed steels with a C content around 0.2 wt% it can be said that a right balance must be found when choosing the Ti content in Nb and Ti microalloyed steels to simultaneously obtain the positive effects of Ti against grain coarsening and the positive effects of Nb on retarding the static recrystallization behavior.

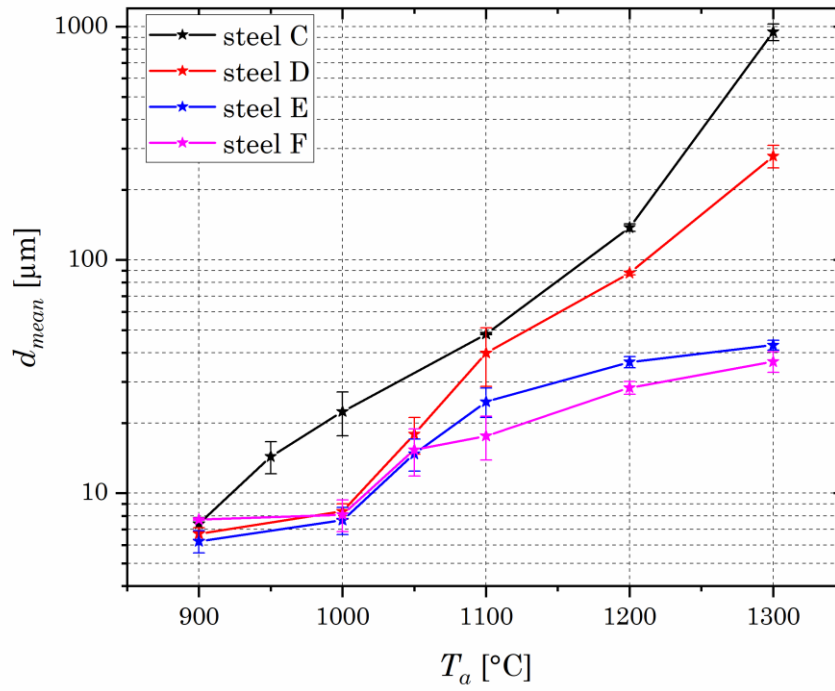


Figure 6.12: Mean size of the prior austenite grains (d_{mean}) after various T_a . Image adapted and reprinted with permission from Paper III.

7 Novel features

The following points summarize the novel findings of the investigations published in the appended publications:

- A new method was developed which has the future potential to determine the degree of recrystallization of microalloyed steels. By choosing a picric acid based etchant, grain elongation of prior austenite grain boundaries can be visualized. By choosing a critical value of grain elongation (f_{crit}) suitable for a certain deformation process, the proportion of recrystallized grains can be determined using light - optical microscopy.
- The influence of different levels of microalloying elements and deformation parameters on recrystallization and microstructure was investigated for microalloyed HSLA steels with a C content over 0.2 wt%. A sufficiently high annealing temperature prior deformation is important in order to use the full potential of the microalloying elements in the subsequent deformation process. Furthermore, a right balance must be found when choosing the Ti content in Nb and Ti microalloyed steels to simultaneously obtain the positive effects of Ti against grain coarsening and the positive effects of Nb on retarding the recrystallization behavior.
- By using scanning transmission electron microscopy, atom probe tomography and electron backscatter diffraction, new insights into the mechanism of formation of dynamic strain - induced transformed ferrite could be obtained. The results suggest that the formation is a displacive mechanism due to a certain orientation relationship between dynamic strain - induced transformed ferrite and the direction of deformation, although accompanied by the diffusion of C during the formation.

8 References

- [1] J.M. Rodriguez-Ibabe, P. Uranga, Thermomechanical Processing of Steels, MDPI, Basel, Switzerland, 2020.
- [2] S. Vervynckt, K. Verbeken, B. Lopez, J.J. Jonas, Modern HSLA steels and role of non-recrystallisation temperature, *International Materials Reviews* 57 (2012) 187–207. <https://doi.org/10.1179/1743280411Y.0000000013>.
- [3] G. Schulze, Die Metallurgie des Schweißens: Eisenwerkstoffe, Nichteisenmetallische Werkstoffe, 4th ed., Springer-Verlag, Heidelberg, Germany, 2009.
- [4] A.J. DeArdo, M.J. Hua, K.G. Cho, C.I. Garcia, On strength of microalloyed steels: an interpretive review, *Materials Science and Technology* 25 (2009) 1074–1082. <https://doi.org/10.1179/174328409X455233>.
- [5] T.N. Baker, Microalloyed steels, *Ironmaking & Steelmaking* 43 (2016) 264–307. <https://doi.org/10.1179/1743281215Y.0000000063>.
- [6] W.B. Morrison, Microalloy steels – the beginning, *Materials Science and Technology* 25 (2009) 1066–1073. <https://doi.org/10.1179/174328409X453299>.
- [7] A.J. DeArdo, Niobium in modern steels, *International Materials Reviews* 48 (2003) 371–402. <https://doi.org/10.1179/095066003225008833>.
- [8] T.N. Baker, Titanium microalloyed steels, *Ironmaking & Steelmaking* 46 (2019) 1–55. <https://doi.org/10.1080/03019233.2018.1446496>.
- [9] H. Hoffmann, G. Spur, R. Neugebauer, *Handbuch Umformen*, 2nd ed., Carl Hanser Fachbuchverlag, München, Germany, 2012.
- [10] World Steel in Figures 2021, <https://worldsteel.org/wp-content/uploads/2021-World-Steel-in-Figures.pdf>, accessed 18 February 2022.
- [11] Total Materia, <https://www.totalmateria.com>, accessed 18 February 2022.
- [12] T. Gladman, *The Physical Metallurgy of Microalloyed Steels*, Institute of Materials, London, UK, 1997.
- [13] D.K. Matlock, J.G. Speer, Microalloying concepts and application in long products, *Materials Science and Technology* 25 (2009) 1118–1125. <https://doi.org/10.1179/174328408X322222>.
- [14] K. Narita, Physical Chemistry of the Groups IVa (Ti, Zr), Va (V, Nb, Ta) and the Rare Earth Elements in Steel, *ISIJ International* 15 (1975) 145–152. <https://doi.org/10.2355/isijinternational1966.15.145>.
- [15] T.N. Baker, Processes, microstructure and properties of vanadium microalloyed steels, *Materials Science and Technology* 25 (2009) 1083–1107. <https://doi.org/10.1179/174328409X453253>.

- [16]Turkdogan E.T., Causes and effects of nitride and carbonitride precipitation during continuous casting, *Iron and Steelmaking* (1989) 61–75.
- [17]J.-M. Jang, S.-H. Seo, J.-S. Han, D.-S. Kim, Y.-B. Kang, J.-J. Pak, Reassessment of $TiN(s)=Ti+N$ Equilibration in Liquid Iron, *ISIJ International* 55 (2015) 2318–2324. <https://doi.org/10.2355/isijinternational.ISIJINT-2015-265>.
- [18]K.J. Irvine, F.B. Pickering, T. Gladman, Grain-refined C-Mn steels, *Journal of Iron and Steel Research International* 205 (1967) 161–182.
- [19]Nordberg H., Aronsson B., Solubility of niobium carbide in austenite, *Journal of the Iron and Steel Institute* (1968) 1263–1266.
- [20]H. Sekine, T. Inoue, M. Ogasawara, Solubility of V_4C_3 in α -Iron, *ISIJ International* 8 (1968) 101–102. <https://doi.org/10.2355/isijinternational1966.8.101>.
- [21]E.O. Hall, The Deformation and Ageing of Mild Steel: III Discussion of Results, *Proc. Phys. Soc. B* 64 (1951) 747–753. <https://doi.org/10.1088/0370-1301/64/9/303>.
- [22]N.J. Petch, The cleavage strength of polycrystals, *Journal of the Iron and Steel Institute* (1953) 25–28.
- [23]T. Gladman, Holmes B., F.B. Pickering, Work Hardening of Low-Carbon Steels, *Journal of the Iron and Steel Institute* (1970) 172.
- [24]C. Wang, M. Wang, J. Shi, W. Hui, H. Dong, Effect of microstructural refinement on the toughness of low carbon martensitic steel, *Scripta Materialia* 58 (2008) 492–495. <https://doi.org/10.1016/j.scriptamat.2007.10.053>.
- [25]M. Gómez, L. Rancel, S.F. Medina, Effects of Nb, V, Ti and Al on Recrystallisation/Precipitation Interaction in Microalloyed Steels, *Materials Science Forum* 638-642 (2010) 3388–3393. <https://doi.org/10.4028/www.scientific.net/MSF.638-642.3388>.
- [26]G.S. Rohrer, “Introduction to Grains, Phases, and Interfaces—an Interpretation of Microstructure,” *Trans. AIME*, 1948, vol. 175, pp. 15–51, by C.S. Smith, *Metallurgical and Materials Transactions A* 41 (2010) 1063–1100. <https://doi.org/10.1007/s11661-010-0215-5>.
- [27]K. Lücke, K. Detert, A quantitative theory of grain-boundary motion and recrystallization in metals in the presence of impurities, *Acta Metallurgica* 5 (1957) 628–637. [https://doi.org/10.1016/0001-6160\(57\)90109-8](https://doi.org/10.1016/0001-6160(57)90109-8).
- [28]J.W. Cahn, The impurity-drag effect in grain boundary motion, *Acta Metallurgica* 10 (1962) 789–798. [https://doi.org/10.1016/0001-6160\(62\)90092-5](https://doi.org/10.1016/0001-6160(62)90092-5).
- [29]C.M. Sellars, J.A. Whiteman, Recrystallization and grain growth in hot rolling, *Metal Science* 13 (1979) 187–194. <https://doi.org/10.1179/msc.1979.13.3-4.187>.

- [30] R. Esterl, M. Sonnleitner, R. Schnitzer, Microstructural Analysis of the Recrystallization Behavior of Low Alloyed Steels, *Steel Research International* 90 (2019) 1800500.
- [31] B. Dutta, E. Valdes, C.M. Sellars, Mechanism and kinetics of strain induced precipitation of Nb(C,N) in austenite, *Acta Metallurgica et Materialia* 40 (1992) 653–662. [https://doi.org/10.1016/0956-7151\(92\)90006-Z](https://doi.org/10.1016/0956-7151(92)90006-Z).
- [32] B. Dutta, C.M. Sellars, Effect of composition and process variables on Nb(C, N) precipitation in niobium microalloyed austenite, *Materials Science and Technology* 3 (1987) 197–206. <https://doi.org/10.1179/mst.1987.3.3.197>.
- [33] B. Dutta, C.M. Sellars, Strengthening of austenite by niobium during hot rolling of Microalloyed steel, *Materials Science and Technology* 2 (1986) 146–153. <https://doi.org/10.1179/mst.1986.2.2.146>.
- [34] B. Dutta, E.J. Palmiere, C.M. Sellars, Modelling the kinetics of strain induced precipitation in Nb microalloyed steels, *Acta Materialia* 49 (2001) 785–794. [https://doi.org/10.1016/S1359-6454\(00\)00389-X](https://doi.org/10.1016/S1359-6454(00)00389-X).
- [35] C. Klinkenberg, K. Hulka, W. Bleck, Niobium Carbide Precipitation in Microalloyed Steel, *Steel Research International* 75 (2004) 744–752. <https://doi.org/10.1002/srin.200405837>.
- [36] J.G. Speer, S.S. Hansen, Austenite recrystallization and carbonitride precipitation in niobium microalloyed steels, *Metallurgical and Materials Transactions A* 20 (1989) 25–38. <https://doi.org/10.1007/bf02647491>.
- [37] Y. Cao, F. Xiao, G. Qiao, C. Huang, X. Zhang, Z. Wu, B. Liao, Strain-induced precipitation and softening behaviors of high Nb microalloyed steels, *Materials Science and Engineering: A* 552 (2012) 502–513. <https://doi.org/10.1016/j.msea.2012.05.078>.
- [38] Coladas R., Masounave J., Bailon J. P. (Eds.), *The hot deformation of austenite*, AIME, New York, USA, 1977.
- [39] M.G. Burke, L.J. Cuddy, J. Piller, M.K. Miller, Combined APFIM–TEM study of Nb(CN) precipitation in HSLA steel, *Materials Science and Technology* 4 (1988) 113–116. <https://doi.org/10.1179/mst.1988.4.2.113>.
- [40] M. Charleux, W.J. Poole, M. Militzer, A. Deschamps, Precipitation behavior and its effect on strengthening of an HSLA-Nb/Ti steel, *Metallurgical and Materials Transactions A* 32 (2001) 1635–1647. <https://doi.org/10.1007/s11661-001-0142-6>.

- [41] J. Strid, K.E. Easterling, On the chemistry and stability of complex carbides and nitrides in microalloyed steels, *Acta Metallurgica* 33 (1985) 2057–2074. [https://doi.org/10.1016/0001-6160\(85\)90129-4](https://doi.org/10.1016/0001-6160(85)90129-4).
- [42] M.J. White, W.S. Owen, Effects of vanadium and nitrogen on recovery and recrystallization during and after hot-working some HSLA steels, *Metallurgical and Materials Transactions A* 11 (1980) 597–604. <https://doi.org/10.1007/BF02670696>.
- [43] M.J. Crooks, A.J. Garratt-Reed, J.B.V. Sande, W.S. Owen, Precipitation and Recrystallization in Some Vanadium and Vanadium-Niobium Microalloyed Steels, *Metallurgical and Materials Transactions A* 12 (1981) 1999–2013. <https://doi.org/10.1007/BF02644169>.
- [44] W.J. Lui, J.J. Jonas (Eds.), *Proceedings of an International Symposium on Processing, microstructure and properties of HSLA steels, 1988, Warrendale, PA, USA*.
- [45] N.K. Balliger, R.W.K. Honeycombe, The effect of nitrogen on precipitation and transformation kinetics in vanadium steels, *Metallurgical and Materials Transactions A* 11 (1980) 421–429. <https://doi.org/10.1007/BF02654566>.
- [46] F.A. Khalid, D.V. Edmonds, Interphase precipitation in microalloyed engineering steels and model alloy, *Materials Science and Technology* 9 (1993) 384–396. <https://doi.org/10.1179/mst.1993.9.5.384>.
- [47] R. Lagneborg, B. Hutchinson, T. Siwecki, S. Zajac, The role of Vanadium in microalloyed steels, *Scandinavian Journal of Metallurgy* 28 (1999) 186–241.
- [48] D. Hernandez, B. López, J.M. Rodríguez-Ibabe, Ferrite Grain Size Refinement in Vanadium Microalloyed Structural Steels, *MSF 500-501* (2005) 411–418. <https://doi.org/10.4028/www.scientific.net/MSF.500-501.411>.
- [49] S.F. Medina, M. Gómez, L. Rancel, Grain refinement by intragranular nucleation of ferrite in a high nitrogen content vanadium microalloyed steel, *Scripta Materialia* 58 (2008) 1110–1113. <https://doi.org/10.1016/j.scriptamat.2008.02.004>.
- [50] S. Zajac, S.F. Medina, V. Schwinn, Grain refinement by intragranular ferrite nucleation on precipitates in microalloyed steels, *ECSC Final Report* (2007).
- [51] A.J. Ardell, Precipitation hardening, *Metallurgical and Materials Transactions A* 16 (1985) 2131–2165. <https://doi.org/10.1007/BF02670416>.
- [52] Orowan E. (Ed.), *Symposium on Internal Stresses in Metals and Alloys, London, UK, 1948*.

- [53] S. Zajac, T. Siwecki, W.B. Hutchinson, R. Lagneborg, Strengthening Mechanisms in Vanadium Microalloyed Steels Intended for Long Products, *ISIJ Int.* 38 (1998) 1130–1139. <https://doi.org/10.2355/isijinternational.38.1130>.
- [54] H. Kejian, T.N. Baker, The effects of small titanium additions on the mechanical properties and the microstructures of controlled rolled niobium-bearing HSLA plate steels, *Materials Science and Engineering: A* 169 (1993) 53–65. [https://doi.org/10.1016/0921-5093\(93\)90598-9](https://doi.org/10.1016/0921-5093(93)90598-9).
- [55] S.G. Hong, K.B. Kang, C.G. Park, Strain-induced precipitation of NbC in Nb and Nb-Ti microalloyed HSLA steels, *Scripta Materialia* 46 (2002) 163–168.
- [56] G. Gottstein, *Physikalische Grundlagen der Materialkunde*, 3rd ed., Springer-Verlag, Berlin, Heidelberg, Germany, 2007.
- [57] K.K. Alaneme, E.A. Okotete, Recrystallization mechanisms and microstructure development in emerging metallic materials: A review, *Journal of Science: Advanced Materials and Devices* 4 (2019) 19–33. <https://doi.org/10.1016/j.jsamd.2018.12.007>.
- [58] N. Hansen, R.F. Mehl, A. Medalist, New discoveries in deformed metals, *Metallurgical and Materials Transactions A* 32 (2001) 2917–2935. <https://doi.org/10.1007/s11661-001-0167-x>.
- [59] T. Yu, N. Hansen, X. Huang, Recovery by triple junction motion in heavily deformed metals, *IOP Conference Series: Materials Science and Engineering* 89 (2015) 12014. <https://doi.org/10.1088/1757-899X/89/1/012014>.
- [60] E. Nes, Recovery revisited, *Acta Metallurgica et Materialia* 43 (1995) 2189–2207. [https://doi.org/10.1016/0956-7151\(94\)00409-9](https://doi.org/10.1016/0956-7151(94)00409-9).
- [61] P.R. Rios, F. Siciliano Jr, H.R.Z. Sandim, R.L. Plaut, A.F. Padilha, Nucleation and growth during recrystallization, *Materials Research* 8 (2005) 225–238. <https://doi.org/10.1590/S1516-14392005000300002>.
- [62] D. Raabe, Recovery and Recrystallization: Phenomena, Physics, Models, Simulation, in: *Physical Metallurgy*, Elsevier, Amsterdam, Netherlands, 2014, pp. 2291–2397.
- [63] K. Huang, R.E. Logé, A review of dynamic recrystallization phenomena in metallic materials, *Materials & Design* 111 (2016) 548–574. <https://doi.org/10.1016/j.matdes.2016.09.012>.
- [64] T. Sakai, A. Belyakov, R. Kaibyshev, H. Miura, J.J. Jonas, Dynamic and post-dynamic recrystallization under hot, cold and severe plastic deformation conditions, *Progress in Materials Science* 60 (2014) 130–207. <https://doi.org/10.1016/j.pmatsci.2013.09.002>.

- [65] K. Barmak, A Commentary on: “Reaction Kinetics in Processes of Nucleation and Growth”*, *Metallurgical and Materials Transactions B* 49 (2018) 3616–3680.
<https://doi.org/10.1007/s11663-010-9421-1>.
- [66] M. Avrami, Kinetics of Phase Change. I General Theory, *The Journal of Chemical Physics* 7 (1939) 1103–1112. <https://doi.org/10.1063/1.1750380>.
- [67] M. Avrami, Kinetics of Phase Change. II Transformation-Time Relations for Random Distribution of Nuclei, *The Journal of Chemical Physics* 8 (1940) 212–224.
<https://doi.org/10.1063/1.1750631>.
- [68] M. Avrami, Granulation, Phase Change, and Microstructure Kinetics of Phase Change. III, *The Journal of Chemical Physics* 9 (1941) 177–184.
<https://doi.org/10.1063/1.1750872>.
- [69] A.N. Kolmogorov, On the Statistical Theory of Crystallization of Metals [in Russian], *Izv. Akad. Nauk SSSR* 3 (1937) 355–359.
- [70] D. Raabe, Cellular Automata in Materials Science with Particular Reference to Recrystallization Simulation, *Annual Review of Materials Research* 32 (2002) 53–76. <https://doi.org/10.1146/annurev.matsci.32.090601.152855>.
- [71] M. El Wahabi, L. Gavard, F. Montheillet, J.M. Cabrera, J.M. Prado, Effect of initial grain size on dynamic recrystallization in high purity austenitic stainless steels, *Acta Materialia* 53 (2005) 4605–4612.
<https://doi.org/10.1016/j.actamat.2005.06.020>.
- [72] E. Nes, Modelling of work hardening and stress saturation in FCC metals, *Progress in Materials Science* 41 (1997) 129–193. [https://doi.org/10.1016/S0079-6425\(97\)00032-7](https://doi.org/10.1016/S0079-6425(97)00032-7).
- [73] E.I. Poliakov, J.J. Jonas, A one-parameter approach to determining the critical conditions for the initiation of dynamic recrystallization, *Acta Materialia* Vol. 44 (1996) 127–136.
- [74] A. Najafizadeh, J.J. Jonas, Predicting the Critical Stress for Initiation of Dynamic Recrystallization, *ISIJ International* 46 (2006) 1679–1684.
<https://doi.org/10.2355/isijinternational.46.1679>.
- [75] L. Ma, Z. Liu, S. Jiao, X. Yuan, Di Wu, Dynamic recrystallization behaviour of Nb-Ti microalloyed steels, *Journal of Wuhan University of Technology-Materials Science* 23 (2008) 551–557. <https://doi.org/10.1007/s11595-006-4551-7>.
- [76] S.F. Medina, J.E. Mancilla, Determination of Static Recrystallization Critical Temperature of Austenite in Microalloyed Steels, *ISIJ International* 33 (1993) 1257–1264. <https://doi.org/10.2355/isijinternational.33.1257>.

- [77] S.F. Medina, J.E. Mancilla, Influence of Alloying Elements in Solution on Static Recrystallization Kinetics of Hot Deformed Steels, *ISIJ International* 36 (1996) 1063–1069. <https://doi.org/10.2355/isijinternational.36.1063>.
- [78] S.F. Medina, A. Quispe, P. Valles, J.L. Banos, Recrystallization-precipitation interaction study of two medium carbon niobium microalloyed steels, *ISIJ International* 39 (1999) 913–922. <https://doi.org/10.2355/isijinternational.39.913>.
- [79] S.F. Medina, A. Quispe, Improved Model for Static Recrystallization Kinetics of Hot Deformed Austenite in Low Alloy and Nb/V Microalloyed Steels, *ISIJ International* 41 (2001) 774–781. <https://doi.org/10.2355/isijinternational.41.774>.
- [80] M. Gómez, S.F. Medina, A. Quispe, P. Valles, Static Recrystallization and Induced Precipitation in a Low Nb Microalloyed Steel, *ISIJ International* 42 (2002) 423–431. <https://doi.org/10.2355/isijinternational.42.423>.
- [81] M. Gómez, S.F. Medina, P. Valles, Determination of Driving and Pinning Forces for Static Recrystallization during Hot Rolling of a Niobium Microalloyed Steel, *ISIJ International* 45 (2005) 1711–1720. <https://doi.org/10.2355/isijinternational.45.1711>.
- [82] S.F. Medina, J.E. Mancilla, Static Recrystallization Modelling of Hot Deformed Microalloyed Steels at Temperatures below the Critical Temperature, *ISIJ International* 36 (1996) 1077–1083. <https://doi.org/10.2355/isijinternational.36.1077>.
- [83] S.F. Medina, J.E. Mancilla, Static recrystallization of austenite and strain induced precipitation kinetics in titanium microalloyed steels, *Acta Metallurgica et Materialia* 42 (1994) 3945–3951. [https://doi.org/10.1016/0956-7151\(94\)90172-4](https://doi.org/10.1016/0956-7151(94)90172-4).
- [84] S.F. Medina, V. Lopez, Static Recrystallization in Austenite and Its Influence on Microstructural Changes in C-Mn Steel and Vanadium Microalloyed Steel at the Hot Strip Mill, *ISIJ International* 33 (1993) 605–614. <https://doi.org/10.2355/isijinternational.33.605>.
- [85] S.F. Medina, J.E. Mancilla, C.A. Hernández, Static Recrystallization of Hot Deformed Austenite and Induced Precipitation Kinetics in Vanadium Microalloyed Steels, *ISIJ International* 34 (1994) 689–696. <https://doi.org/10.2355/isijinternational.34.689>.
- [86] Quispe A., S.F. Medina, P. Valles, Recrystallization-induced Precipitation Interaction in a Medium Carbon Vanadium Microalloyed Steel, *ISIJ International* 37 (1997) 783–788. <https://doi.org/10.2355/isijinternational.37.783>.

- [87] A.J. DeArdo (Ed.), Thermomechanical processing of microalloyed austenite: Proceedings of the International Conference on the Thermomechanical Processing of Microalloyed Austenite, The Metallurgical Society of AIME, Warrendale, PA, USA, 1982.
- [88] F. Boratto, R. Barbosa, S. Yue, J.J. Jonas, Physical metallurgy of thermomechanical processing of steels and other metals, in: Thermomechanical processing of steels and other materials, THERMEC-88, Tokyo, Japan, 1988, pp. 383–390.
- [89] T. Maki (Ed.), Morphology and substructure of martensite in steels, Elsevier, Amsterdam, Netherlands, 2012.
- [90] T. Maki, I. Tamura, On the thin plate martensite in ferrous alloys and its various properties, *Bull. Japan Inst. Metals* 23 (1984) 229–237.
- [91] S. Morito, H. Tanaka, R. Konishi, T. Furuhashi, T. Maki, The morphology and crystallography of lath martensite in Fe-C alloys, *Acta Materialia* 51 (2003) 1789–1799. [https://doi.org/10.1016/S1359-6454\(02\)00577-3](https://doi.org/10.1016/S1359-6454(02)00577-3).
- [92] T. Inoue, S. Matsuda, ichi, Y. Okamura, K. Aoki, The Fracture of a Low Carbon Tempered Martensite, *Transactions of the Japan Institute of Metals* 11 (1970) 36–43. <https://doi.org/10.2320/matertrans1960.11.36>.
- [93] S. Matsuda, T. Inoue, H. Mimura, Y. Okamura, Toughness and Effective Grain Size in Heat-Treated Low-Alloy High Strength Steels, *ISIJ International* 12 (1972) 325–333. <https://doi.org/10.2355/isijinternational1966.12.325>.
- [94] T. Furuhashi, K. Kikumoto, H. Saito, T. Sekine, T. Ogawa, S. Morito, T. Maki, Phase Transformation from Fine-grained Austenite, *ISIJ International* 48 (2008) 1038–1045. <https://doi.org/10.2355/isijinternational.48.1038>.
- [95] S. Morito, H. Saito, T. Ogawa, T. Furuhashi, T. Maki, Effect of Austenite Grain Size on the Morphology and Crystallography of Lath Martensite in Low Carbon Steels, *Metallurgical Transactions A* 45 (2005) 91–94. <https://doi.org/10.2355/isijinternational.45.91>.
- [96] E.I. Galindo-Nava, P. Rivera-Díaz-del-Castillo, A model for the microstructure behaviour and strength evolution in lath martensite, *Acta Materialia* 98 (2015) 81–93. <https://doi.org/10.1016/j.actamat.2015.07.018>.
- [97] S. Morito, H. Yoshida, T. Maki, X. Huang, Effect of block size on the strength of lath martensite in low carbon steels, *Materials Science and Engineering: A* 438-440 (2006) 237–240. <https://doi.org/10.1016/j.msea.2005.12.048>.
- [98] J. Daigne, M. Guttman, J.P. Naylor, The influence of lath boundaries and carbide distribution on the yield strength of 0.4% C tempered martensitic steels, *Materials*

- Science and Engineering 56 (1982) 1–10. [https://doi.org/10.1016/0025-5416\(82\)90176-8](https://doi.org/10.1016/0025-5416(82)90176-8).
- [99] A. Shibata, T. Nagoshi, M. Sone, S. Morito, Y. Higo, Evaluation of the block boundary and sub-block boundary strengths of ferrous lath martensite using a micro-bending test, *Materials Science and Engineering: A* 527 (2010) 7538–7544. <https://doi.org/10.1016/j.msea.2010.08.026>.
- [100] A.J. Kaijalainen, P.P. Suikkanen, T.J. Linnell, L.P. Karjalainen, J.I. Kömi, D.A. Porter, Effect of austenite grain structure on the strength and toughness of direct-quenched martensite, *Journal of Alloys and Compounds* 577 (2013) S642–S648. <https://doi.org/10.1016/j.jallcom.2012.03.030>.
- [101] E. Macherauch, H.-W. Zoch, *Praktikum in Werkstoffkunde*, Springer Fachmedien Wiesbaden, Wiesbaden, Germany, 2014.
- [102] TA Instruments, *Leitfaden zur Inbetriebnahme eines TA Instruments-Dilatometers: DIL805 V10.2*, Hüllhorst, Germany, 2017.
- [103] S. Vervynckt, K. Verbeken, P. Thibaux, Y. Houbaert, Characterization of the Austenite Recrystallization by Comparing Double Deformation and Stress Relaxation Tests, *Steel Research International* 81 (2010) 234–244. <https://doi.org/10.1002/srin.200900126>.
- [104] L.P. Karjalainen, Stress relaxation method for investigation of softening kinetics in hot deformed steels, *Materials Science and Technology* 11 (1995) 557–565. <https://doi.org/10.1179/mst.1995.11.6.557>.
- [105] C.N. Homsher, Determination of the Non-Recrystallization Temperature in Multiple Microalloyed Steels. Master thesis, Colorado School of Mines, Golden, CO, USA, 2013.
- [106] Y.B. Xu, Y.M. Yu, B.L. Xiao, Z.Y. Liu, G.D. Wang, Modelling of microstructure evolution during hot rolling of a high-Nb HSLA steel, *Journal of Materials Science* 45 (2010) 2580–2590. <https://doi.org/10.1007/s10853-010-4229-6>.
- [107] C. Devadas, I.V. Samarasekera, E.B. Hawbolt, The thermal and metallurgical state of steel strip during hot rolling: Part III. Microstructural evolution, *Metallurgical Transactions A Volume* 22 (1991) 335–349.
- [108] E.J. Palmiere, C.I. Garcia, A.J. DeArdo, The Influence of Niobium Supersaturation on the Static Recrystallization Behavior of Microalloyed Steels, *Metallurgical and Materials Transactions A Volume* 27A (1996) 951–960.

- [109] O. Kwon, A.J. DeArdo, Interactions between recrystallization and precipitation in hot-deformed microalloyed steels, *Acta Metallurgica et Materialia* 39 (1991) 529–538. [https://doi.org/10.1016/0956-7151\(91\)90121-G](https://doi.org/10.1016/0956-7151(91)90121-G).
- [110] G. Li, T.M. Maccagno, D.Q. Bai, J.J. Jonas, Effect of Initial Grain Size on the Static Recrystallization Kinetics of Nb Microalloyed Steels, *ISIJ International* 36 (1996) 1479–1485. <https://doi.org/10.2355/isijinternational.36.1479>.
- [111] Fernandez A. I., B. Lopez, J.M. Rodriguez-Ibabe, Relationship between the austenite recrystallized fraction and the softening measured from the interrupted torsion test technique, *Scripta Materialia* Vol. 40 (1999) 543–549.
- [112] S. Vervynckt, Control of the Non-Recrystallization Temperature in High Strength Low Alloy (HSLA) Steels. PhD Thesis, Gent, Belgium, 2010.
- [113] W. Lefebvre-Ulrikson (Ed.), Atom probe tomography: Put theory into practice, Academic Press, London, UK, 2016.
- [114] M.K. Miller, R.G. Forbes, Atom probe tomography, *Materials Characterization* 60 (2009) 461–469. <https://doi.org/10.1016/j.matchar.2009.02.007>.
- [115] P. Felfer, L. Stevenson, T. Li, Atom Probe Tomography, *Practical Metallography* 55 (2018) 515–526. <https://doi.org/10.3139/147.110543>.
- [116] A. Cerezo, P.H. Clifton, M.J. Galtrey, C.J. Humphreys, T.F. Kelly, D.J. Larson, S. Lozano-Perez, E.A. Marquis, R.A. Oliver, G. Sha, K. Thompson, M. Zandbergen, R.L. Alvis, Atom probe tomography today, *Materials Today* 10 (2007) 36–42. [https://doi.org/10.1016/S1369-7021\(07\)70306-1](https://doi.org/10.1016/S1369-7021(07)70306-1).
- [117] M. Nöhrer, W. Mayer, S. Primig, S. Zamberger, E. Kozeschnik, H. Leitner, Influence of Deformation on the Precipitation Behavior of Nb(CN) in Austenite and Ferrite, *Metallurgical and Materials Transactions A* 45 (2014) 4210–4219. <https://doi.org/10.1007/s11661-014-2373-3>.
- [118] M. Nöhrer, S. Zamberger, S. Primig, H. Leitner, Atom probe study of vanadium interphase precipitates and randomly distributed vanadium precipitates in ferrite, *Micron* (Oxford, England 1993) 54-55 (2013) 57–64. <https://doi.org/10.1016/j.micron.2013.08.008>.
- [119] M. Nöhrer, W. Mayer, S. Zamberger, E. Kozeschnik, H. Leitner, Precipitation Behavior of Strain-Induced V Precipitates in Ferrite at Different Temperatures in a 0.2 wt% Carbon Steel, *Steel Research International* 85 (2014) 679–688. <https://doi.org/10.1002/srin.201300185>.

- [120] J. Weibel, A. Herges, D. Britz, E. Detemple, V. Flaxa, H. Mohrbacher, F. Mücklich, Tracing Microalloy Precipitation in Nb-Ti HSLA Steel during Austenite Conditioning, *Metals* 10 (2020) 243. <https://doi.org/10.3390/met10020243>.
- [121] E.V. Pereloma, A.G. Kostryzhev, A. AlShahrani, C. Zhu, J.M. Cairney, C.R. Killmore, S.P. Ringer, Effect of austenite deformation temperature on Nb clustering and precipitation in microalloyed steel, *Scripta Materialia* 75 (2014) 74–77. <https://doi.org/10.1016/j.scriptamat.2013.11.026>.
- [122] A.G. Kostryzhev, A. Al Shahrani, C. Zhu, S.P. Ringer, E.V. Pereloma, Effect of deformation temperature on niobium clustering, precipitation and austenite recrystallisation in a Nb–Ti microalloyed steel, *Materials Science and Engineering: A* 581 (2013) 16–25. <https://doi.org/10.1016/j.msea.2013.05.068>.
- [123] K. Thompson, D. Lawrence, D.J. Larson, J.D. Olson, T.F. Kelly, B. Gorman, In situ site-specific specimen preparation for atom probe tomography, *Ultramicroscopy* 107 (2007) 131–139. <https://doi.org/10.1016/j.ultramicro.2006.06.008>.
- [124] R.R. Keller, R.H. Geiss, Transmission EBSD from 10 nm domains in a scanning electron microscope, *Journal of microscopy* 245 (2012) 245–251. <https://doi.org/10.1111/j.1365-2818.2011.03566.x>.
- [125] G.C. Sneddon, P.W. Trimby, J.M. Cairney, Transmission Kikuchi diffraction in a scanning electron microscope: A review, *Materials Science and Engineering: R: Reports* 110 (2016) 1–12. <https://doi.org/10.1016/j.mser.2016.10.001>.
- [126] P.W. Trimby, Orientation mapping of nanostructured materials using transmission Kikuchi diffraction in the scanning electron microscope, *Ultramicroscopy* 120 (2012) 16–24. <https://doi.org/10.1016/j.ultramicro.2012.06.004>.
- [127] S. Suzuki, Features of Transmission EBSD and its Application, *JOM* 65 (2013) 1254–1263. <https://doi.org/10.1007/s11837-013-0700-6>.
- [128] A. Bhattacharya, C.M. Parish, Y. Katoh, J. Henry, Data for: High throughput crystal structure and composition mapping of crystalline nanoprecipitates in alloys by transmission Kikuchi diffraction and analytical electron microscopy.: Supplementary data, <https://data.mendeley.com/datasets/wsyx4sm548/1>.
- [129] A. Bhattacharya, C.M. Parish, J. Henry, Y. Katoh, High throughput crystal structure and composition mapping of crystalline nanoprecipitates in alloys by transmission Kikuchi diffraction and analytical electron microscopy, *Ultramicroscopy* 202 (2019) 33–43. <https://doi.org/10.1016/j.ultramicro.2019.03.015>.
- [130] M. Gómez, L. Rancel, B.J. Fernández, S.F. Medina, Evolution of austenite static recrystallization and grain size during hot rolling of a V-microalloyed steel,

- Materials Science and Engineering: A 501 (2009) 188–196.
<https://doi.org/10.1016/j.msea.2008.09.074>.
- [131] P.O. Malta, D.S. Alves, A.O.V. Ferreira, I.D. Moutinho, C.A.P. Dias, D.B. Santos, Static Recrystallization Kinetics and Crystallographic Texture of Nb-Stabilized Ferritic Stainless Steel Based on Orientation Imaging Microscopy, *Metallurgical and Materials Transactions A* 48 (2017) 1288–1309. <https://doi.org/10.1007/s11661-016-3935-3>.
- [132] M. Black, R. Higginson, An investigation into the use of electron back scattered diffraction to measure recrystallised fraction, *Scripta Materialia* 41 (1999) 125–129. [https://doi.org/10.1016/s1359-6462\(99\)00051-2](https://doi.org/10.1016/s1359-6462(99)00051-2).
- [133] S. Illescas, J. Fernández, J.M. Guilemany, Kinetic analysis of the austenitic grain growth in HSLA steel with a low carbon content, *Materials Letters* 62 (2008) 3478–3480. <https://doi.org/10.1016/j.matlet.2008.03.001>.
- [134] D. Dong, F. Chen, Z. Cui, Modeling of Austenite Grain Growth During Austenitization in a Low Alloy Steel, *Journal of Materials Engineering and Performance* 25 (2016) 152–164. <https://doi.org/10.1007/s11665-015-1810-9>.
- [135] H. Beladi, G.L. Kelly, P.D. Hodgson, Ultrafine grained structure formation in steels using dynamic strain induced transformation processing, *International Materials Reviews* 52 (2007) 14–28. <https://doi.org/10.1179/174328006X102538>.
- [136] C. Ghosh, C. Aranas, J.J. Jonas, Dynamic transformation of deformed austenite at temperatures above the Ae₃, *Progress in Materials Science* 82 (2016) 151–233. <https://doi.org/10.1016/j.pmatsci.2016.04.004>.
- [137] L. Hao, M. Sun, N. Xiao, D. Li, Characterizations of Dynamic Strain-induced Transformation in Low Carbon Steel, *Journal of Materials Science & Technology* 28 (2012) 1095–1101. [https://doi.org/10.1016/S1005-0302\(12\)60178-9](https://doi.org/10.1016/S1005-0302(12)60178-9).
- [138] C. Zheng, N. Xiao, L. Hao, D. Li, Y. Li, Numerical simulation of dynamic strain-induced austenite–ferrite transformation in a low carbon steel, *Acta Materialia* 57 (2009) 2956–2968. <https://doi.org/10.1016/j.actamat.2009.03.005>.
- [139] L. Sun, K. Muszka, B.P. Wynne, E.J. Palmiere, Effect of strain path on dynamic strain-induced transformation in a microalloyed steel, *Acta Materialia* 66 (2014) 132–149. <https://doi.org/10.1016/j.actamat.2013.11.062>.
- [140] P.J. Hurley, P.D. Hodgson, B.C. Muddle, Analysis and characterisation of ultra-fine ferrite produced during a new steel strip rolling process, *Scripta Materialia* 40 (1999) 433–438. [https://doi.org/10.1016/S1359-6462\(98\)00442-4](https://doi.org/10.1016/S1359-6462(98)00442-4).

- [141] T. George, J.J. Irani, Control of austenitic grain size by addition of titanium, *Acta Metallurgica* 13 (1968) 94.
- [142] L.J. Cuddy, J.C. Raley, Austenite Grain Coarsening in Microalloyed Steels, *Metallurgical Transactions A Volume 14A* (1983) 1989–1995.
- [143] S.C. Hong, S.H. Lim, H.S. Hong, K.J. Lee, D.H. Shin, K.S. Lee, Effect of Nb on grain growth of ferrite in C-Mn steel during isothermal holding after severe deformation, *Materials Science and Technology* 20 (2004) 207–212.
<https://doi.org/10.1179/026708304225011261>.